Electrolyte-gated organic field effect transistor with functionalized lipid monolayer for novel sensors

ナギュ, ファン, ティン

https://doi.org/10.15017/4060115

出版情報：九州大学, 2019, 博士（工学）, 課程博士
バージョン：
権利関係：

Electrolyte-gated organic field effect transistor with functionalized lipid monolayer for novel sensors

Nguy Phan Tin

Kyushu University

2019

Table of Contents

Chapter 1 Introduction

1.1. Backgrounds

Nowadays, the rapid growth in urban and industrial causes critical pollution for the aqueous environment.[1,2] The contamination of heavy metal ions and organic compounds (pharmaceutical and personal care products, pesticides, persistent organic pollutants, endocrine-disrupting chemicals, heavy metals or toxins) into water are the main reason for almost pollution issues.[1,2] Notably, most of the heavy metals and organic compounds are considered to be toxic to humans, animals, fishes, and the environment, even at low concentrations.[1,3] As the pollution is prolonged and absorbed into the human body through the water and food sources, these toxins can cause critical diseases such as kidney damage, liver damage Wilson, visceral cancers and vascular disease, depression, lethargy, and neurological signs.[1] If the pollution can be detected at an early stage, the solving of contamination accidents will be more favorable, resulting in the reduction of negative impacts on the environment and humans. The detection and monitoring of pollution, therefore, are critical meanings for protecting the environment and human health.

GC-MS **Atomic Absorption Spectrometer**

Figure 1.1. Ions and molecules analysis systems.[4,5]

The conventional methods for the identification and quantification of ions and molecules such as high-performance liquid chromatography (HPLC), liquid chromatography coupled with mass spectroscopy (LC-MS and LC-MS/MS) or electrochemical detection (LC-ED), gas chromatography coupled with mass spectroscopy or not (GC and GC-MS), are popularly based on chromatographic techniques. Although these techniques represent accurate and sensitive tools to identify and quantify ions and molecules, there are still some disadvantages. They require expensive and complex instrumentations, and intricate sample preparations, as seen in **Figure 1.1**. Furthermore, these methods are also time-consuming and difficult to achieve in real-time for high-frequency monitoring of pollutants in large areas. Therefore, the development of innovative analytical techniques that encompass selectivity, sensitivity, easiness-to-handle, accuracy, swiftness, high-throughput, integration, and wearable associated with real-time monitoring capabilities are necessary.

For this purpose, sensor technology is widely known as an effective alternative tool for the detection of ions and molecules with a low-cost, an easy handle of measurement. Furthermore, the sensor technology allows us for on-situ detection, a large area of monitoring by a sensor network, and being free from limiting by geographical locations.[6,7] Concerning the detection and monitoring of soluble analytes, there are some typical types of sensors, such as electrochemical, optical, piezoelectric, gravimetric, pyroelectric, and electrical sensors. Among these platforms, electrical sensors based on the organic field-effect transistor (OFET) are widely known in the past twenty years due to their intrinsic advantages.[8–10] OFET structure allows the sensor to be manufactured by a high-throughput fabrication process with a low cost by printing technique on a large area of a flexible substrate, and be favorably integrated into an electronic circuit.[10–16] Additionally, OFETs based sensors offer versatility and feasibility in the optimization to gain high selectivity and sensitivity.[17,18] Transistor-based sensors integrate three typically main parts of the sensor, namely a probe, a transducer, and an amplifier in one device that remarkably enhances the sensitivity even with negligible input signals.[19–22]

For the detection of elements in the aqueous environment, an electrolyte solution has widely been used as electrical gates in OFETs by immersing a gate electrode into an electrolyte solution.[23–28] With this configuration, the high gating capacitance (1-20 μFcm^{-2})[29,30] is obtained through the formation of an electrical double layer (EDL) at the

electrolyte and organic semiconductor interface. Of importance is that the high capacitance allows the electrolyte-gated OFETs (EG-OFETs) effectively to work at the millivolt range. This feature is suitable for portable devices, which require low power consumption. Another merit of EG-OFET is an ultra-low threshold voltage (V_{th}), which is used as an output of the sensor. This parameter is affected by a variety of surface charge caused by ions or biomolecules.[20,25] The ultra-low threshold voltage, therefore, allows the sensor to be sensitive even with a small signal. With these features, the EG-OFETs are excellently suitable for the detection of ions and biomolecules in the aqueous environment. However, there are still serious challenges for the EG-OFET-based sensors. The first challenge is the stable operation of EG-OFETs in the electrolyte solution. [30–33] In fact, the detection of ions or biomolecules is typically carried out in the presence of many interfering ions, e.g., potassium and sodium. These ions are well known to act as electrical dopants to organic semiconductors, causing degradation of the transistor performance.[29,30,34] Second, the protocol for the synthesis and attaching the probes on organic semiconductor channels are necessary to detect analytes such as ions and proteins.

Here, we propose an EG-OFET with a lipid monolayer to address the above challenges for sensor applications. In these devices, the P3HT - poly(3-hexylthiophene-2,5-diyl) is employed as an organic semiconductor channel due to its intrinsic advantage. The P3HT film consists of the thiophene-core layer with the two alkyl chains on both sides. This structure allows the P3HT film to be stable in the aqueous environment, as reported in the literature.[23,28] To protect P3HT film from the doping effect and to attach sensing probes, we introduce the ultrathin lipid monolayer (2.2 nm)[35] at the interface between the electrolyte solution and the organic semiconductor for the first time. A striking point is the lipid monolayer can protect the organic semiconductor layer from directly contacting with the electrolyte solution. The EG-OFET with a lipid monolayer, therefore, achieves the stable transistor operation even in aqueous conditions because of the reduction of electrochemical doping into the organic semiconductor. Moreover, head groups of lipid monolayers can be easily functionalized to graft many kinds of probes for different sensor applications. Here, the transistors with OH-terminated lipid monolayers show potential for pH sensor. The devices demonstrate a linear sensitivity with pH level in the range of 4 to 12, which satisfies the physiological pH range of 4-8 required for biosensor applications.[36] However, the pH sensitivity of devices is a disadvantage for

ion sensor applications. The signal from pH sensitivity will interfere with the output signal of the ion sensor. Therefore, it is necessary to eliminate this disadvantage. The OH- groups are passivated by using inert groups, methyltrichlorosilane (MTS), through the silanization process.[20,35] The devices with MTS groups show independence on the pH variation. As a result, EG-OFETs with functionalized lipid monolayers demonstrate a stable operation in electrolyte solution even with pH variation. This property of EG-OFET is necessary for ion sensor applications.

As proof of concept, the new sensor for the detection of cesium ions in natural waters was developed. In the past half-century, radioactive pollution from metal ions in the aqueous has become a critical concern for both environmental and human health issues. The main reasons for the dramatic health condition of humans, aquatic plants, and animals are high-level radiation ions, as well as low-level radiation ions accumulating over long periods.[37] Among radioactive ions, cesium isotopes are common sources of radioactive pollution. Cesium isotopes behave as soluble elements and show high mobility in aqueous environments with pollutants found in very far away from the source. Notably, the concerns on cesium pollution have become more serious after the Fukushima Daiichi Nuclear Power Plant accident. The Japanese government announces that a safety level of radioactive cesium ion concentration in water is 10 $Bq.kg^{-1}$. Monitoring the level of cesium ions in soft and sea waters in large areas is an essential requirement for marine life and human safety.[38]

For the achievement of the highly sensitive detection of cesium ions, the probes have to be high selectivity to cesium ions and well attach to EG-OFET. Herein, a novel probe for cesium ions based on crown ether, which is well known for metal ion complexes, was synthesized.[39–41] The crown ether is developed on the calixarene scaffold. Because the calixarene scaffold can reduce the flexibility of crown ether, as well as provide positions to graft a whole probe onto the lipid monolayer. The new structure of the probe allows the complexation to be grafted easily on lipid monolayer by using the same protocol for the passivation of OH groups. The new cesium ion sensor demonstrates ultra-sensitivity for the detection of cesium ions. The low limit of detection can be achieved at 10^{-17} M. The range of detection was up to 10 orders of concentration. Notably, the high sensitivity of the sensor is obtained even with the presence of interfering ions, e.g., potassium and sodium ions. For practical application, the sensor is utilized to detect

cesium ions in synthetic seawater. The preliminary result indicates that the sensor can detect the cesium ion at a low concentration in pseudo practical conditions. With these features, our sensor satisfies the requirement of the Japanese government for the cesium ion concentration in tap water.[42] The sensor is also superior to the conventional technique, inductively coupled plasma-mass spectroscopy (ICP-MS). ICP-MS only can detect cesium ions in the range 10^{-11} to 10^{-8} in DI-water. Meanwhile, other sensors are limited by the high concentration and the small range of cesium ion detection.[41,43–45] From these results, the EG-OFETs with engineered lipid monolayer provide an innovative concept for biosensors and chemical sensors.

The detail of sensor development and characterization was described in the following sections.

1.1.1. Advantages of OFET for sensor applications

In this study, a field-effect transistor (FET) is used as a platform to develop the sensor due to the advantages of FET. FET structure provides the versatility of being able to achieve high selectivity and sensitivity. Furthermore, sensors based on FET can be favorable integration to electronic circuits that is suitable for the sensor network as well as data collecting and processing for IoT.[6,7] Another interest of these sensors is the easiness of the measurements, including no requirement of skilled manipulators and their integration into transportable systems. At the early stages, FET sensors are well known for the pH level detection, where they measure the concentrations of H^+ ion a solution through the ion-selective electrode (ISFET). FET-based sensors are sensitive to the charged surface of the dielectric layer caused by the change of H^+ ion concentrations.[9,46] In recent years, FET-based sensors have undergone many developments and have been improved for the highly sensitive detection of ions and biomolecules like enzymes, proteins, DNA, and so on.[20,47–51]

On the other hand, depending on the chosen materials and fabrication techniques, bulk fabrication of FETs can be produced at a low cost. Organic materials, therefore, have been attracted much attention in recent decades because of their advantages in fulfilling these requirements.[17,22,52–54] Organic field-effect transistors (OFETs) exhibit intrinsic processing characteristics since they can be favorably produced at or near room

temperature.[11,13,55] OFETs, therefore, can be manufactured in bulk on flexible polymeric substrates and even on paper through nano/microelectronic technology or ink-jet printing technologies.[13,14,55,56] Furthermore, the impressive improvement of the OFET performance during the last decade is comparable with conventional inorganic materials.[11,57] These features allow the OFETs to become potential competitive candidates for the replacement of existing or novel thin-film transistors in applications requiring large-area coverage, structural flexibility, low-temperature processing, and especially low cost. Notably, OFETs can be fabricated entirely from inexpensive and natural, biodegradable materials.

1.1.2. Operation of OFET and OFET-based sensors

For the OFET-based sensor, the parameters of OFET are commonly used as output signals, namely threshold voltage, drain-source current, and carrier mobility. The understanding of the operation of OFET, therefore, is necessary. **Figure 1.2** shows a typical back-gate bottom-contact configuration of the p-type OFET. The simple OFET consists of three-terminal electrodes, including source (S), drain (D), and gate (G), a thin insulating layer with a high dielectric constant, and an organic semiconductor layer.[11] The operation of OFET is similar to the conventional MOSFET (metal-oxide-semiconductor field-effect transistor). The gate electrode is biased to establish the electric field across the dielectric layer. The gate voltage can control the charge carrier density in the organic semiconductor. Hence, the current flowing between the source and drain electrodes through the organic semiconductor can be modulated, resulting in the relationship between the gate voltage (V_{GS}) and the drain current (I_{DS}).[10,11]

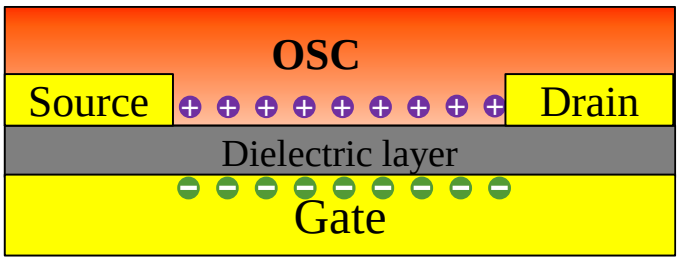

Figure 1.2. A typical back-gate bottom-contact configuration of OFET.

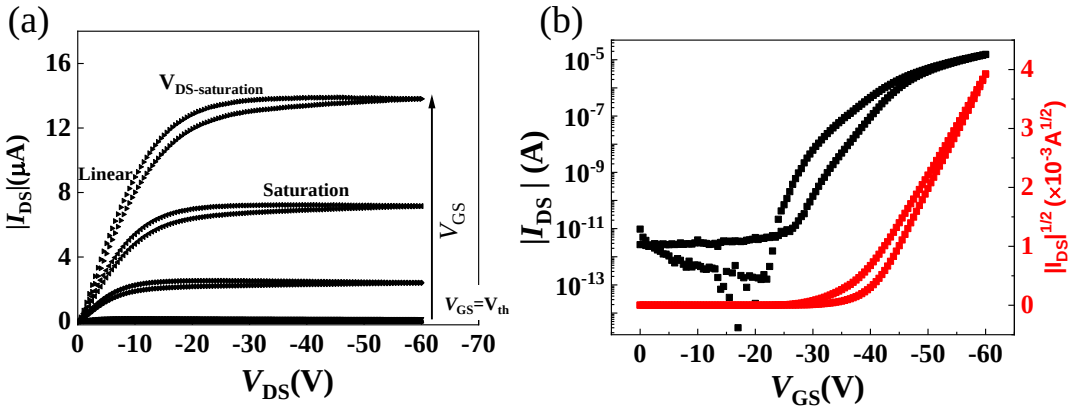

Figure 1.3. (a) Current–voltage (I_{DS} – V_{DS}) characteristic curve of a p-channel OFET device at different V_{GS} gate voltages. The linear region at $V_{DS} < (V_{GS} - V_{th})$ and saturation region $V_{DS} > (V_{GS} - V_{th})$. (b) Square root of the current–voltage (I_{DS}–V_{GS}) transfer characteristic measured at $V_{DS} = -60$ V.

Figure 1.3 shows the typical curves for the p-channel OFET. As for all FET-based devices, the output curves are the set of I_{DS} currents measured as a function of drain-source voltage (V_{DS}) at different gate bias voltages. The curves include two regions, namely a linear region at $V_{DS} \ll (V_{GS} - V_{th})$ and a saturation region at $V_{DS} > (V_{GS} - V_{th})$. At low drain-source voltages (linear regime), the I_{DS} current is proportional to V_{DS} at a fixed V_{GS} following Ohm's law. As the drain-source voltage becomes more negative, the charge carrier density near the drain electrode reduces until generating pinch-off of the channel. The $I_{DS,}$ therefore, is limited to a constant value (saturation region) even if the V_{DS} continues to rise. These features of OFET I–V curves are well described by analytical equations below.[10,11]

$$I_{DS} = \frac{W}{2L}\mu C_i(V_{GS} - V_{th})^2 \qquad V_{DS} \ll (V_{GS} - V_{th})\text{: linear region} \qquad (1.1)$$

$$I_{DS} = \frac{W}{2L}\mu C_i(V_{GS} - V_{th})^2 \qquad V_{DS} > (V_{GS} - V_{th})\text{: saturation region} \qquad (1.2)$$

where W and L are width and length of semiconductor channel, respectively, μ and C_i are the carrier mobility and the capacitance of the gate insulator, respectively, V_{th} is the threshold voltage of the device.

The driving force towards the use of OFETs as sensors is the combination of the accuracy electronic output signal and the high sensing performance with low-cost

fabrication for the development of single-use or disposable devices. For instance, an array of sensors can be fabricated in one device by the nano-imprinting technique to develop lab-on-chip for the detection of analytes concentration. In the late 80s, a sensor based on OFET was first introduced as a chemical sensor to detect chemical substances with one report.[10,33] Since then, the OFET sensors have been developed rapidly and adapted for the detection of many substances in chemistry and biology.[8,10,15] At this time, OFET sensors were proposed to work as multi-parametric sensors based on the typical parameters of OFETs, namely the field-effect mobility and the on current, as well as the threshold voltage and the bulk conductivity of the organic film.[10] In general, the variation of these four electrical parameters of OFETs can be simultaneously observed at room temperature.[11] In this approach, pioneered in 2000, these four electrical parameters were considered as the output parameters used to characterize an OFET sensor's response to given analytes.[10] However, the bulk conductivity of the semiconducting channel is typical and could be measured in an equivalent resistor sensor.[10] Meanwhile, other parameters can be easily extracted from the transfer curves of OFET by use using **Equation 1.2**.[10,33] The response of a resistor, therefore, is less used as the specific output signal in OFET sensors than three other parameters.[33] The basic mechanism operation of OFET sensors based on the chemical interaction between the analytes and the recognition molecules layer whose charged products can act as extra gating to the OFET, leading to a measurable shift of threshold voltage (V_{th}) or mobility.[8,10,15,33] As an expectation based on **Equation 1.2**, these changes result in a variation of the drain-source current and the two-dimension conductivity. Moreover, the calculation of the mobility values is quite complicated in some kinds of OFET sensors. The threshold voltage, therefore, has been widely utilized as a primary sensor output.[20,26,58] The more detail of the sensing mechanism will be discussed in the below section.

To date, four types of OFET have been proposed for chemical and biological sensors, as seen in **Figure 1.4**.[10,33,59] The first one is called organic electrochemical transistors (OECTs), in which the organic semiconductor layer was used as a sensing layer. The popularly sensing mechanism involves the oxidation or reduction of analytes at the interface of the organic semiconductor layer.[10,33] Dependence on the organic semiconductor layer properties and morphology, the analytes can cause changes in the V_{th} or mobility due to charge trapping and variation of the potential barrier.[10,29] Another

mechanism of this sensor has been proposed involving electrochemical reactions, which take place at the interface of the organic semiconductor leading to modulate the I_{DS}.[29,60,61] These OCETs are widely utilized for gas sensors.[61] For the chemical and biological analytes, the accuracy and stable operation of these sensors are affected by the doping effect from the electrolyte solution to the organic semiconductor.[8]

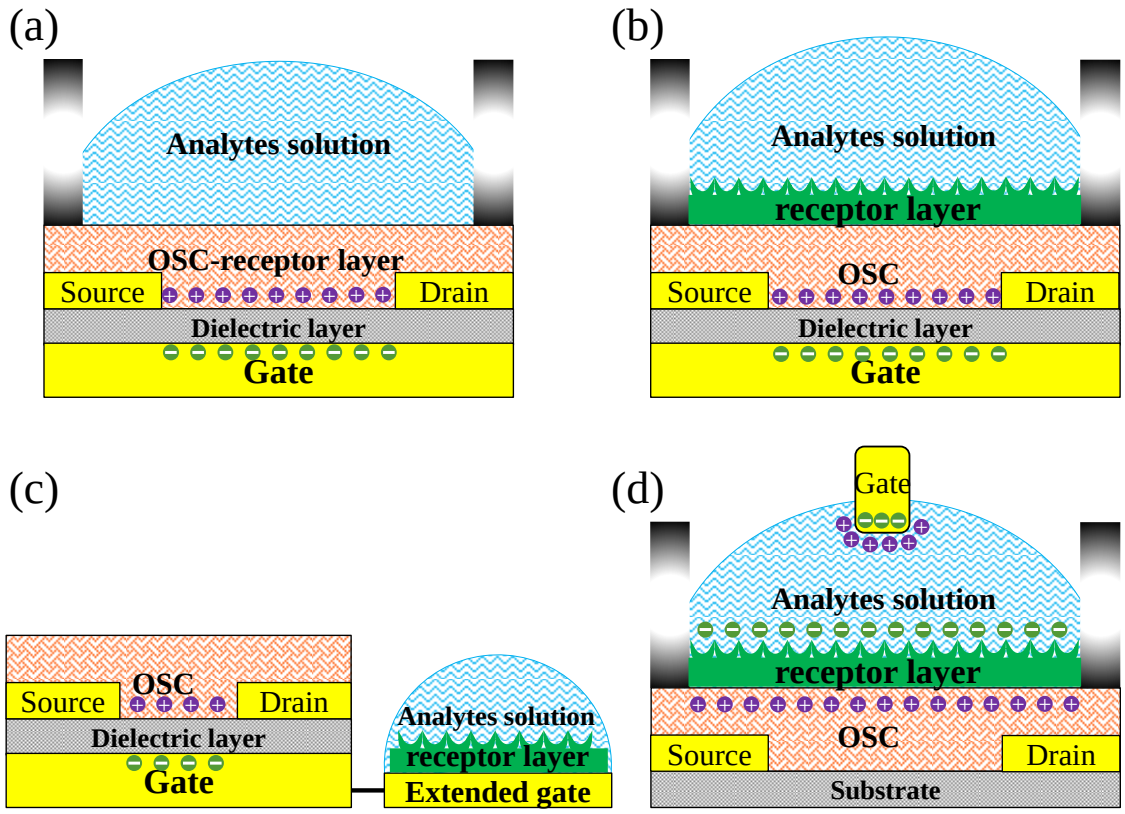

Figure 1.4. Structure of four kinds of sensors based on OFET.

In the second structure, a receptor layer is introduced at the interface of the organic semiconductor layer. For the sensor with high selectivity capabilities, it is necessary to implement molecules capable of strong interactions with target analytes. These systems are widely addressed as receptors. This layer has a high selectivity to analytes even at low dissociation constant to achieve a low limit of detection due to the strong interactions.[10] The chemical interactions between receptors and analytes induce the variation charge at the surface leading to the shift of V_{th}. Because of using the conventional back gate, these devices are affected by strong bias stress resulting in a large clockwise hysteresis loop

during the transfer scan.[33] These sensors, therefore, require an ultra-thin gate dielectric to operate at a low voltage.[10,33]

In the third structure, a receptor layer is assembled on the extended gate instead of the organic semiconductor layer.[21,25,53] These sensors avoid the contact between the organic semiconductor layer and electrolyte solution allowing the sensors working as a conventional OFET. However, these devices require an ultra-thin gate dielectric to reduce the operating voltage as the second structure. Furthermore, this sensor structure becomes more complicated and larger than others.

The last device is electrolyte-gated organic field-effect transistors (EGOFETs). The conventional OFETs use an insulating layer to separate the organic semiconductor from the gate electrode. Here, EGOFETs used the electrolyte solution to separate the organic semiconductor layer from the gate electrode. An electrical double layer (EDL) forms at the interface between the solution and the semiconductor channel by coupling of pairs of opposite charges when the gate bias applies.[10,33,59] This EDL has an extremely high capacitance due to its sub-nano thickness.[10,33,59] The gating capacitance allows EG-OFETs to operate at a sub-voltage range.[10,23,30,34,62,63] This feature is necessary to reduce power consumption for portable devices in wireless sensor networks. Moreover, EG-OFETs are no longer affected by bias stress leading to reduce hysteresis in the loop of the transfer curve.[33] For sensor applications, the specific receptors can be integrated into EGOFETs by functionalizing the organic semiconductor or the gate electrode.[12,19,26,64] With the advantages mentioned above, I aim to develop a new versatile sensor based on the EG-OFET structure.

1.2. Challenges for development of EG-OFET based sensor

In recent years, EG-OFETs have been attached much attention to the development of the sensor for the detection of ions and biomolecules. These sensors face some challenges, although sensor based on EG-OFET has many advantages as mentioned above. The first issue is a stable operation of EG-OFET in the electrolyte solution for practical use. The second issue is the immobilization of specific receptors onto the organic

semiconductor layer for sensor applications. The details will be discussed in the two following sections.

1.2.1. The doping effect of electrostatic and electrochemical processes

The electrolyte solution is aggressive to the organic semiconductor and results in the degradation of OFET. The main reasons are electrostatic and electrochemical doping processes.[59,65] When the voltage is applied, these processes will occur simultaneously.[33] For instance, water is always used as an electrolyte gated solution at the early stage of the development of sensors based on EG-OFET.[23] Because the ultrapure water has a minimum ion concentration of solvated protons (H^+) and hydroxyl ions (OH^-) of 10^{-7} M. The low ion concentration will reduce the possibility of electrochemical processes. However, in water, the autoprotolysis always occurs in the self-ionization of water reaction **(Equation 1.3)**.[33,66] The water normally shows an ionic conductivity of 10^{-5} Sm^{-1} due to proton transfer.[33] Moreover, when the applied voltage is reached to oxidation potential or reduction potential, the electrochemical process in water will strongly occur, as seen at **Equation 1.4** and **1.5**.[33]

$$2H_2O \leftrightharpoons OH^- + H_3O^+ \quad (1.3)$$

$$H_2O \leftrightharpoons 2H^+ + \frac{1}{2}O_2 + 2e^- \quad (1.4)$$

$$2H_2O + 2e^- \leftrightharpoons H_2 + 2OH^- \quad (1.5)$$

In the operation mode of OFET, the electrochemical process will occur on the surface of the organic semiconductor, as seen in **Equation 1.6** and **1.7**.[33] These processes are considered as a charge carrier trapping/detrapping at the interface of the organic semiconductor, causing the minor hysteresis during the transfer curve scan.[33]

$$2OSC^+ + H_2O \leftrightharpoons 2OSC^0 + 2H^+ + \frac{1}{2}O_2 \quad (1.6)$$

$$2OSC^0 + 2H^+ \leftrightharpoons 2OSC^+ + H_2 \quad (1.7)$$

If the potential difference between the source and drain electrodes exceeds 1 V, the strong electrolysis process will occur at the interface between the organic semiconductor and water molecules. The remarkable Faradaic current can be measured and degrade the performance of EG-OFET.[33] Furthermore, in the electrolyte solution, the electrochemical will occur easier and stronger than that in the water due to the high concentration of ions even under 1 V.[67,68] These reactions limit the voltage applied to the gate and drain electrodes of EG-OFET. The development sensors based on EG-OFET, therefore, need to concern about the applied voltage as well as the doping effect of the electrolyte solution.

1.2.2. The immobilization of specific receptor

For the unique detection of analytes, the specific recognition sites of the sensor should be stably secured either through integration into the device structure or chemically grafting them on the organic semiconductor surface. Several approaches have been proposed to attach the probes into the EG-OFET.[33] Horowitz's group introduced a method using a polythiophene derivative with carboxyl side chains - poly[3-(5-carboxypentyl)thiophene-2,5-diyl] (P3PT - COOH) as the organic semiconductor layer.[24,69] A part of the carboxyl-groups exposed to the electrolyte solution and paired with the DNA strands through the chemical bonding. However, due to the existence of COOH-groups, the thiophene film became hydrophilic, leading to being a favorite for the ion penetration into the polymer.[24,69] The large hysteresis, therefore, was observed at the loop of the transfer curve.

Another popular method is the functionalization of the organic semiconductor layer with some groups like carboxyl (COOH), hydroxyl (OH) or amino (NH_2) groups to make a covalent bonding with proteins (DNA, enzymes, antibody-antigen) to the interface between the organic semiconductor and analyte solutions. Buth et al. modified the sexithiophene (6T) surface by using the UV/oxidation method to create hydroxyl groups (OH).[27] Then, the surface was further functionalized by (3-aminopropyl)triethoxysilane (APTES) to exchange hydroxyl groups by amino groups, followed by the activation of the carboxylic acid process by the N-ethyl-N'-(3-dimethylaminopropyl)-carbodiimide hydrochloride (EDC) and N-hydroxysuccinimide

(NHS). Finally, the penicillin enzymes were attached to the surface through the chemical bonding with carboxyl groups. The devices showed the sensitivity changes in the concentration of the penicillin target molecules. However, the performance of the WG-OFET slightly degraded due to UV treatment. Torsi's group and Bao's group introduced another way to form a rich layer of carboxyl groups on polymeric organic semiconductor by plasma-enhanced chemical vapor deposition (PE-CVD).[26,70] Although PE-CVD is quite complicated, this method negligible affected the performance of EG-OFET. Bao's group directly attached the N-terminus of the peptide nucleic acid (PNA) to these carboxyls using EDC/NHS chemistry.[70] Meanwhile, Torsi's group further had modified the COOH layer by NH_2-functionalized phospholipids bilayer before attaching recognition elements (streptavidin).

Although there are many interesting attempts to attach the recognition elements on the organic semiconductor surface, these methods still suffer many disadvantages, namely the degradation of EG-OFET performance and the requirement of a complicated system. Moreover, most of these methods mainly focus on the detection of biomolecules. There are lacking in EG-OFET based sensors for the detection of ions. The development of alternative methods, therefore, is necessary to overcome these limitations. Additionally, the alternative method has to remain the ultra-low operation voltage of EG-OFET.

1.3. Purposes and strategies

In this dissertation, I would like developing a new ultra-highly sensitive sensor based on EG-OFET for the detection of ions or molecules in a solution. The selectivity of the sensor will be easily adaptable on-demand of the aimed target. In this case, the cesium ion is selected as a target to demonstrate the applicability of the new sensor structure for the detection of analytes in the aqueous. Two challenges mentioned above must be addressed to achieve the final sensor. The surface of organic semiconductor, therefore, is proposed to be modified by a lipid monolayer. This layer will protect the organic semiconductor from the electrolyte solution. Additionally, the head groups of this layer can be used to graft cesium probes on it. With lipid monolayer, the new sensor can surpass the challenges of EG-OFET.

The new sensor, therefore, consists of three key components, namely the organic semiconductor, lipid monolayer, and cesium ion probe. The organic semiconductor plays a role as a basic component to assemble other parts on it. For this role, the organic semiconductor must be a flat surface and stable in the water environment. Then, the surface of the organic semiconductor will be modified by lipid monolayer through the vesicle protocol. The lipid monolayer is expected to protect the organic semiconductor from the doping effect of the electrolyte solution.[33] The operation of EG-OFET with lipid monolayer, therefore, is improved to achieve stable performance. Besides, the head groups of the lipid monolayer will be functionalized to graft specific probes into EG-OFET. Finally, for the cesium ions sensor, the probes must be highly selective to cesium ions. The probes will be synthesized and designed by my collaborators in France. The detail of the materials and strategies for sensor development is described below.

1.3.1. Material of organic semiconductor

In this dissertation, poly(3-hexylthiophene-2-5-dily) (P3HT) molecules were employed as the organic semiconductor of EG-OFET. **Figure 1.5(a)** shows the chemical structure of P3HT molecules. P3HT molecules provide intrinsic advantages which are worth for EG-OFET. P3HT molecules are soluble in the organic solvent, like chloroform, chlorobenzene, dichlorobenzene, and toluene, allowing large-scale low-cost applications via solution processing.[13] Due to the existence of thiophene and alkyl chain in the same molecule scaffold, the P3HT film can form a sandwich structure with a core layer of thiophene and two hydrophobic alkyl chains (C_6H_{13}) at both sides, as seen in **Figure 1.5(b).**

The core layer of thiophene is the polymer backbones formed by the π-conjugation of thiophene rings. Besides, the strong π-π interactions between the thiophene rings of neighboring polymer chains allow these chains forming in two-dimensional sheets (lamellae) with order along the π- π stacking direction. Meanwhile, the van der Waals interaction between alkyl chains of polymer sheets provides a stacking order in three-dimension.[71] The P3HT film, therefore, can be crystallized to improve the charge transport capability.[72] The charges can be transported along the polymer backbone and the delocalization of the carriers in the π-stacking direction of two-dimensional sheets.

Furthermore, the strong π-π interaction between polymer chains makes P3HT films to be stable in the aqueous environment. On the other hand, the super-hydrophobic surface of the P3HT film is necessary for the lipid monolayer deposition process. There are hydrophobic interactions between lipid molecules and the surface of P3HT film. Another merit of P3HT film is a flat surface allowing lipid molecules well form on that. From the above advantages, P3HT film is suitable for our EG-OFET based sensors.

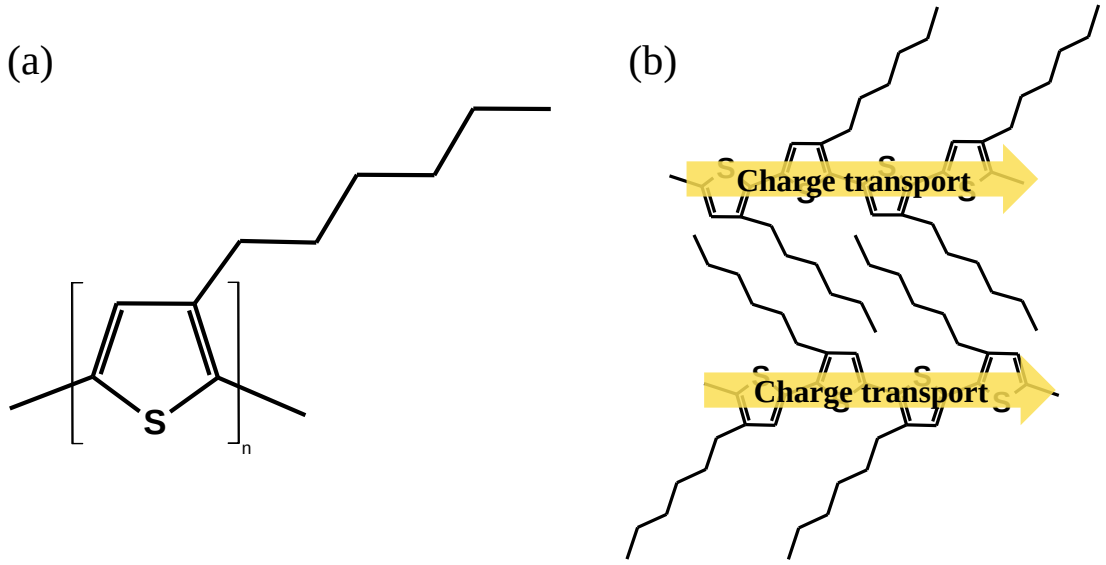

Figure 1.5. (a) Chemical structure of P3HT. (b) Charges transport in P3HT film

1.3.2. Modification of organic semiconductor channel

For sensors based on EG-OFET, surface modification is necessary. The main purpose is the immobilization of receptor molecules on the organic semiconductor surface.[24,73] Additionally, the surface modification also reduces the doping effect due to avoiding the direct contact of the organic semiconductor with electrolyte solution[54,74]. However, the modification protocol should not impact the organic semiconductor to avoid the degradation of EG-OFET. Furthermore, OFETs must remain a low voltage operation. For this purpose, the ultra-thin phospholipid monolayer (~2.2 nm) is proposed to modify the surface of the P3HT film.

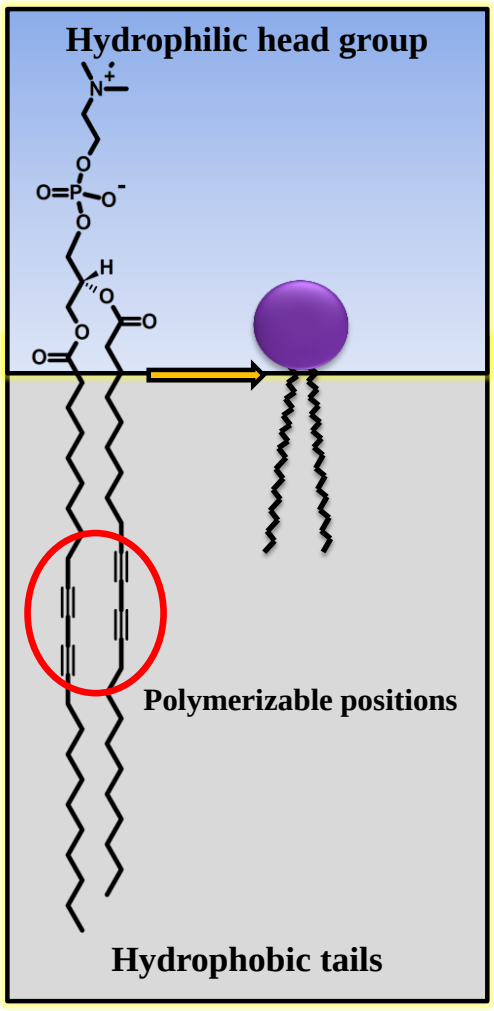

Figure 1.6. Chemical structure of polar phospholipid molecule

To develop the modification protocol, I used a commercial lipid, DCPC (1,2-bis(10,12-tricosadiynoyl)-sn-glycero-3-phosphocholine) lipid due to its intrinsic properties. DCPC lipids are amphiphilic molecules that allow DCPC molecules in water spontaneously self-assembling to form bilayers, monolayer, or form spherical lipid shells, known as vesicles under suitable conditions (**Figure 1.6**).[75–77] It is worthy of note that the lipid membrane is a natural insulator, which is an efficient barrier to both ionic and electronic transport.[78,79] The electrical resistance of the lipid membrane can reach giga-ohm in magnitude, although its' thickness is ultra-thin (2 nm).[75,80] Moreover, it is reported that the lipid membrane is stable enough against the oxidation and electrolysis process in a few months.[77] The lipid monolayer, therefore, can minimize the doping effect from the electrolyte solution into the organic semiconductor. On the other hand, we

can functionalize the head groups of lipids to attach specific probes into EG-OFET. The vesicles of desired compositions can be prepared to form lipid membranes with different functional groups. Furthermore, we can do a two-dimension polymerization of lipid molecules in the plane of the membrane at the positions of acetylene groups. This feature can improve the mechanical stability of the lipid membrane. The lipid monolayer, therefore, is stable on P3HT film during subsequent modification. With these features, the lipid membrane is suitable to employ in applications requiring high resistance, biocompatibility, and flexibility.

1.3.3. Cesium ion probes

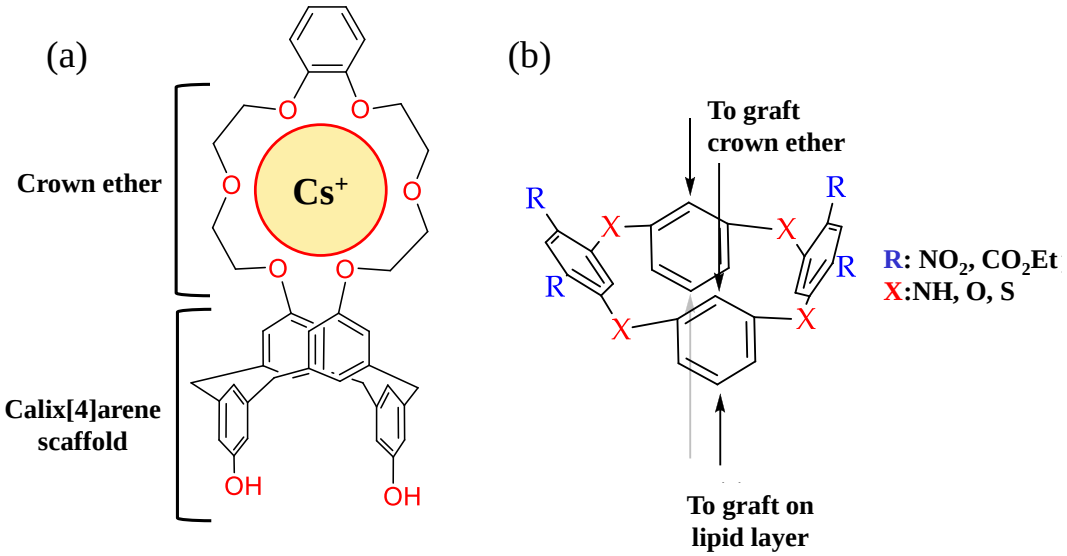

Figure 1.7. a) 1,3-alternated calix[4]arenes bearing crown ether which is specific for Cesium ion and two hydroxyl groups to graft onto lipid part. b) a) Calix[4]arene scaffold with available positions, namely **R** and **X** for adjusting the size of crown ether as well as affinity to cesium ions.

As discussed in section 1.1, in recent years, radioactive contamination from cesium ions has been gained much attention since the Fukushima accident. Cesium ions have high mobility in marine environments with pollutants found at a very far away from a source. Monitoring a level of cesium ions in soft and sea waters in large areas is, therefore, an essential requirement for marine life and human safety.[38] However, the conventional techniques are limited by expensive cost, sophisticated instrumentation,

intricate sample preparations, and time-consuming. Additionally, there are a few sensors that have been developed to detect on-situ cesium ions in water. The method used the ion-selective membrane based on polyvinyl chloride (PVC) mixed with Cs^+ ionophores.[41,43] These sensors showed either the limit of detection at a high concentration (10^{-7} M) or a small linear range of the detection (three orders of magnitude).[41,43] The new sensor for highly sensitive detection of cesium ions, therefore, is critical meaning. Herein, the cesium probe has been synthesized based on the new complexation of cesium ion with crown ether. The probe must be highly selective to cesium ion and be vertically attachable to the lipid monolayer.

The selectivity of the sensor is originated from the presence of specific probes on the lipid monolayer. For high selectivity of the cesium ions sensor, the chemically synthesized probes have to exhibit a high affinity constant towards Cs^+ ions in two dimensions (steric repulsion or Coulomb interactions between probes might decrease their chelating performances) and a low affinity constant for other ions. Therefore, the probe will be synthesized based on crown ether, which is well known for stable cesium ion complexes. Ideally, only cesium ions should fit the stereochemistry of the recognition site of crown ether. Additionally, the ion interactions should be strong enough to make a complex with the low dissociation constant required to achieve a low limit of detection. Besides, the complexation between the probes and cesium ions must be reversible under chemical treatment or application of electrical stress for reusable sensors. Furthermore, the synthesized probes require functional groups that allow them to be grafted to the lipid monolayer. To this end, the complexion of cesium ion with crown ether will be developed based on the calixarene scaffold, as seen in **Figure 1.7**. The calix[4]arene scaffold will reduce the flexibility of the crown ether ring to obtain a stable cavity. Additionally, there are available positions on the calix[4]arene scaffold to adjust the size of crown ether and affinity to cesium ions that improve the selectivity of probes to cesium ions. Several calix[4]arene derivatives have been reported in the literature for having high affinity constant for cesium ions.[81–84] Our colleagues will focus on this type of molecule and synthesize a probe that will fulfill the above-mentioned specifications.

1.3.4. Strategies for the development of sensor

For a highly sensitive sensor, three key components must be well assembled. For this purpose, this dissertation focuses on three chief tasks in sensor development, including the investigation of a protocol to form the functionalizable lipid monolayer on the organic semiconductor, the establishment of OFET operation in DI-water (Water gated-OFET), the performance of OFET in the electrolyte solution (EG-OFET) for sensor applications. The strategies of each task will be briefly described below.

For the first task, I modify the surface of the P3HT film by the lipid monolayer through the vesicle protocol. A commercial lipid (DCPC) is employed to develop and optimize the lipid monolayer deposition process on the P3HT film, as seen in **Figure 1.6**. DCPC lipids can self-assemble a monolayer on P3HT film through a hydrophobic interaction between alkyl chains of lipids and P3HT film. Concurrently, lipid molecules are inter-polymerized during the deposition process to improve mechanical stability. By using ATR-FTIR (attenuated total reflection Fourier-transform infrared) technique, I can confirm the existence of lipid monolayer on the P3HT film through the intrinsic chemical bonding on DCPC molecules. Besides, the formation of lipids on P3HT film can be reconfirmed by using a simple method, water contact angle measurement. The change of the hydrophobic surface of P3HT film to the hydrophilic surface of the lipid monolayer is observed through a change of water contact angle. Furthermore, the atomic force microscopy (AFM) measurements are useful to investigate the effect of the lipid monolayer deposition process on the P3HT film. AFM measurement allows us to observe the change of morphology of P3HT film at a nanometer-scale before and after lipid deposition. Moreover, the thickness of the lipid monolayer can be calculated by X-ray reflection (XRR) measurement, which is useful to estimate the thin film thickness. On the other hand, for grafting specific probes, the head groups of DCPC lipids will be cleaved to form OH-groups before the lipid membrane deposition. The cesium probes are attached to OH-lipids by using silane groups as intermediate junctions. Here, I replace OH-groups by the methyltrichlorosilane (MTS) groups through the silanization protocol. Because these groups are hydrophobic, the functionalization is conducted directly on the lipid membrane after the deposition process. Moreover, this functionalization is equivalent to a second polymerization. After two times of polymerization, the mechanical stability of

the lipid monolayer on P3HT is expected to improve significantly. This makes the lipid membrane more stable on P3HT film for further modification. The mechanical stability is evaluated by using the force measurement method of the AFM technique.

The second purpose focuses on the establishment of water-gated OFET concerning P3HT film morphology, the metals of the gate electrode, and the surface modification by the lipid monolayer. This step is necessary for the stable operation of the sensor later. To the first stage of sensor development based on EG-OFET, de-ionized (DI) water is used as an electrolyte solution for gating bias. The DI-water has a minimum ion concentration of solvated protons (H^+) and hydroxyl ions (OH^-) of 10^{-7} M that reduces the possibility of ions doping effect into the P3HT film. The intrinsic advantage of WG-OFET is the high capacitance of the electrical double layer forming at the interface. This layer is sensitivity to the roughness of the P3HT film due to its sub-nano thickness. Furthermore, the work functions of metal electrodes influence on the threshold voltage of WG-OFET.[85] Therefore, I employ the gold (Au) electrode instead of the tungsten (W) electrode as a gate electrode to reduce the threshold voltage. Finally, I investigate the influence of lipid monolayer on the operation of WG-OFET. The lipid monolayer is expected to reduce the doping effect into the organic semiconductor leading to improve the operation of WG-OFET in long-term use.

The final purpose, I characterize the performance of EG-OFET functionalized by lipid monolayers for sensor applications. **Figure 1.8** illustrates the suggested sensor based on the EG-OFET. In this step, the electrolyte solution replaces DI-water to resemble the conditions in practice. Though, it is reported that the electrolyte solution caused aggressively doping for the organic semiconductor.[10,59] Hence, the role of lipid monolayer to prevent the doping effect becomes more important. However, the OH groups of the lipid monolayer are sensitive to pH change that significantly impacts the sensor performance.[20] The control of pH sensitivity, therefore, is necessary. For this purpose, the OH-terminated lipid membrane is passivated by MTS using the same protocol in **chapter 2**. With this method, I can passivate the OH-groups as well as use for grafting cesium probes. As a result, I can tune the pH sensitivity of EG-OFET by functionalizing the head groups of the lipid monolayer. The EG-OFET with MTS-lipid monolayer is expected to be stable in electrolyte solution even with pH variation. Finally, the cesium ion probes are grafted to the OH-lipid monolayer for the detection of cesium

ion. The synthesis and characterization of cesium ion probes are completed by my collaborators who have experienced in the calix[4]arene derivatives.[86–88] The recognition properties of such calixarenes are characterized before grafting onto the surface concerning the size cavities and nature of the arms presenting on the macrocycle scaffold.[89] The final sensors will be examined in the presence of interfering ions to prove their high sensitivity for the detection of cesium ions.

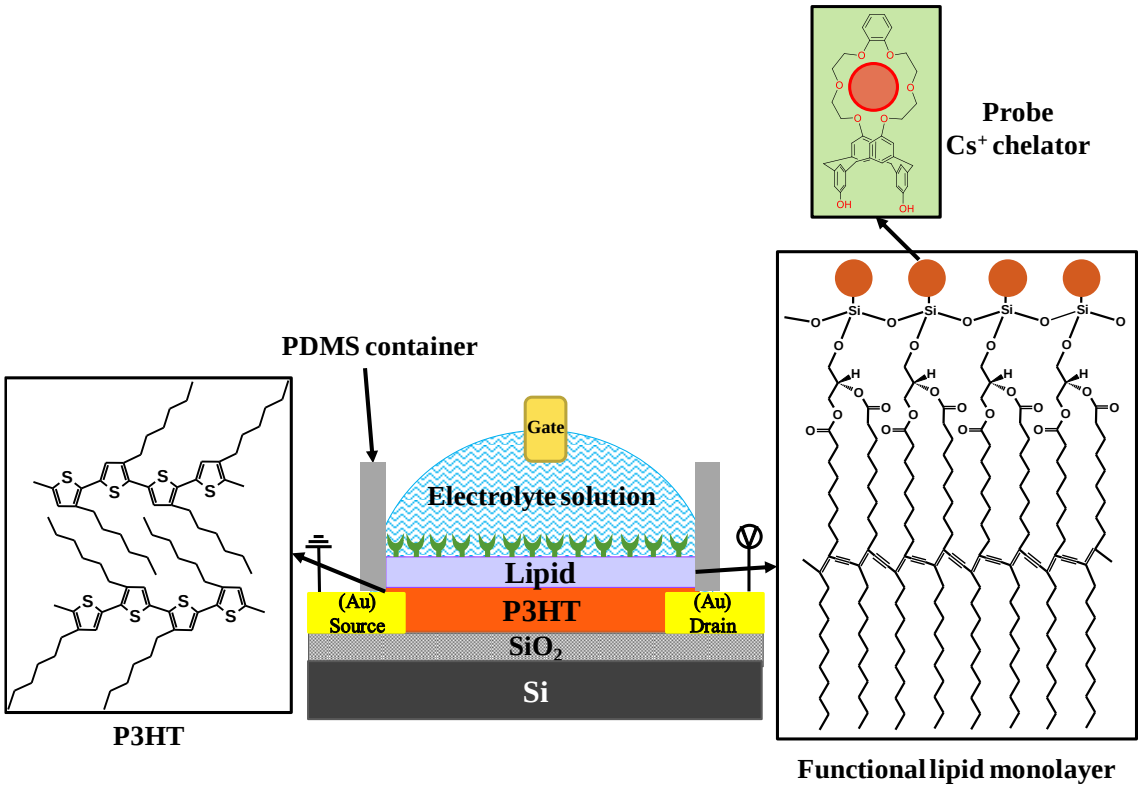

Figure 1.8. Illustration of suggested sensor structure.

1.4. Organization

This dissertation includes five chapters. Chapter 1 provides a general introduction, including the background, motivations, problems, suggested materials, and strategies for this work. Chapter 2 presents the formation of lipid monolayers on the P3HT film, including the inter-polymerization of the lipid membrane as well as the further functionalization of lipid head groups for grafting of cesium probes. Chapter 3

demonstrates the influence of parameters on the performance WG-OFET, namely the morphology of P3HT, metals of gate electrodes, and surface modification by the lipid monolayer. Chapter 4 shows the sensitivity capability of EG-OFET in the tuning of pH sensitivity and the detection of cesium ion. Finally, chapter 5 gives a summary of this dissertation.

Chapter 2 The formation of lipid monolayer

2.1. Introduction

The P3HT has been widely utilized as the organic semiconductor of EG-OFET due to its stability in the aqueous environment. However, the inert surface of the P3HT film limits the way to functionalize the surface for sensor applications. One popular way is a fabrication of a thin layer rich in COOH groups on the P3HT film through the PE-CVD technique.[26,70] However, this method requires a complicated system for the PE-CVD process. Another way is embedding the functional groups directly into the organic semiconductor channel by using COOH -functionalized P3HT molecules. Although this method is simple, the performance of the transistor is reduced in the aqueous medium due to the intrinsic hydrophilic of COOH-P3HT film. The alternative way to functionalize the P3HT film is necessary.

In this chapter, the new protocol to functionalize P3HT film was investigated. Here, an ultra-thin lipid monolayer was coated on the P3HT film through the vesicle protocol. This is a simple technique that takes advantage of the amphipathic property of lipids to form a monolayer on the P3HT film. Due to the ultra-thin thickness of the lipid membrane, the EG-OFETs functionalized by lipid can remain a low operating voltage. Additionally, the lipid membrane also reduces the penetration of ions into the organic semiconductor. In this chapter, I studied the formation as well as the property of the lipid monolayer on the P3HT film. Firstly, DCPC lipid molecules were used to form the membrane on the P3HT film. Then, I did the polymerization at the middle of lipid molecules to enhance mechanical stability. The FT-IR is an important tool to confirm the existence of DCPC lipid monolayer by realizing the specific bonds of DCPC lipid monolayer, namely C=C, C=O, C-N. Then, I evaluated the formation of lipid molecules on the P3HT film by using the water contact angle measurement. The change of surface property after lipid monolayer deposition causes the variation of contact angle. After that, XRR (X-ray reflection) measurement is a powerful tool to examine the thickness of the lipid monolayer. Besides, to be sure that the P3HT film is stable after the lipid monolayer

deposition, we can use the AFM technique to observe the changes in the morphology of P3HT film at nanoscale. For sensor applications, I replaced the head groups of DCPC lipids by OH-groups to form OH-lipid monolayer (DCOH). OH-groups play an important role in stably grafting of probes onto the lipid membrane. The cesium ion probes will be grafted onto the lipid monolayer through the silane groups. Here, MTS groups interacted with OH groups to form DC-MTS lipid monolayer. The formation of DCOH and DCMTS on P3HT was also reconfirmed by ATR-FTIR measurements. The modification of OH groups is also equivalent to the second polymerization. Therefore, we can estimate the mechanical property of DCOH lipid monolayer after MTS passivation. The force measurement by AFM is useful to evaluate the mechanical stability of lipid monolayer after two times of polymerization. Additionally, the effect of lipid monolayer on the carrier transport in P3HT film can be evaluated by estimating the mobility. Therefore, the capacitance of EDL before and after the deposition of lipid monolayer will be calculated by EIS measurements.

2.2. Formation of lipid monolayer on P3HT film

2.2.1. Experimental details

Highly doped Si wafers with 200 nm thickness of SiO_2 on top was used as a substrate. The substrate was cleaned by acetone, followed by isopropanol and DI-water in sonication to remove a photoresist layer. Then, the ultraviolet/ozone cleaning was employed in fifteen minutes to remove organic molecules on the surface of the substrate before being used for spin-coating P3HT film.

P3HT powder was purchased from Sigma Aldrich and used without further purified. **Figure 2.1** shows the preparation process of P3HT film samples for the lipid monolayer deposition process. P3HT powder was dissolved in chlorobenzene (CHB) solvent and heated at 60 ºC for 30 minutes to obtain a P3HT solution. Then, the solution was allowed to go through the filter with a pore size of 200 nm to obtain a homogeneous solution. Then, the P3HT solution was spin-coated on the substrate with a speed of 2000 rpm in 60 seconds. Subsequently, the sample was annealed at 150 ºC in 1 hour to remove

the residue solution and improve the orientation of the P3HT film.[90] The samples were kept in a vacuum until being used in the deposition process of the lipid monolayer.

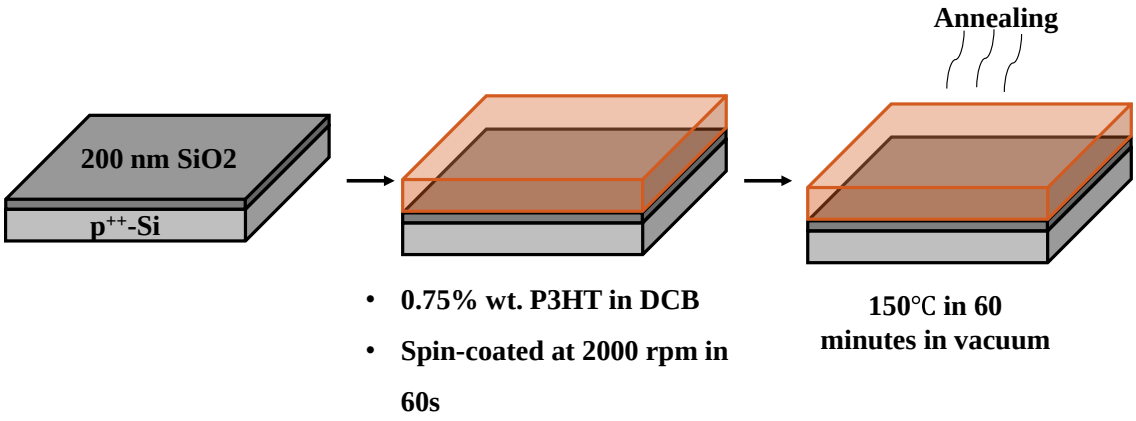

Figure 2.1. The schematic of P3HT film preparation for lipid monolayer deposition

A commercial lipid, (1,2-bis(10,12-tricosadiynoyl)-sn-glycero-3-phosphocholine) (DCPC) lipid powder was purchased from Avanti Polar Lipids (AL, USA) and stored at – 20 ºC for long-term use. For the further functionalization of lipid monolayer, the OH-terminated lipid (DCOH) was synthesized from DCPC lipid. **Figure 2.2** shows the chemical structure of two kinds of phospholipid molecules as well as the synthesis process of DCOH. The DCPC was cleaved with phospholipase C in water for two hours at 40 ºC. The polar head-group of DCPC was successfully replaced by OH-group just before the phosphate group.[47] Then, two kinds of lipids will be coated on P3HT film through vesicle protocol, as described in detail below.[28]

Lipid powder was dissolved in DI-water to prepare a solution of 1 wt% lipid. After that, the solution was sonicated for 30 minutes to obtain vesicles form of lipid. Then, we can obtain the lipid solution of small unilamellar vesicles after extruding through a filter with a pore size of 100 nm. The final lipid solution was dropped to cover all the surface of the P3HT film for the deposition process. The sample was kept on a heating stage during this process. Firstly, by adjusting the temperature of the heating stage to 10 ºC for 5 minutes, the lipid vesicles cracked and spread on the P3HT surface. The lipid molecules self-assembled monolayers through a hydrophobic interaction between the alkyl chains of the P3HT film and lipid molecules. Then, the temperature was gradually increased from 10 ºC to 30 ºC by adjusting 1 ºC per minute to detach the upper layers

from the first monolayer. Because the lipid molecules self-assembled on the P3HT film through the van der Waals interaction, the lipid monolayer was mechanically unstable. Therefore, the lipid membrane was inter-polymerized at acetylene groups to improve mechanical stability. **Figure2.4** shows the chemical structure of AAPD (azobis(2-amidinopropane) dihydrochloride), used as a radical initiator of the polymerization process.[35,91] At 30 ºC, AAPD molecules were added into the solution. Subsequently, the temperature of the sample was increased to 42 ºC by adjusting 5 ºC per ten minutes. The sample was remained at 42 ºC in 45 minutes to make sure the inter-polymerization occurs completely. Finally, the lipid monolayer was formed on the P3HT after cooling down to room temperature and cleaning by DI-water. **Figure 2.3** illustrates the detail of the lipid monolayer deposition process.

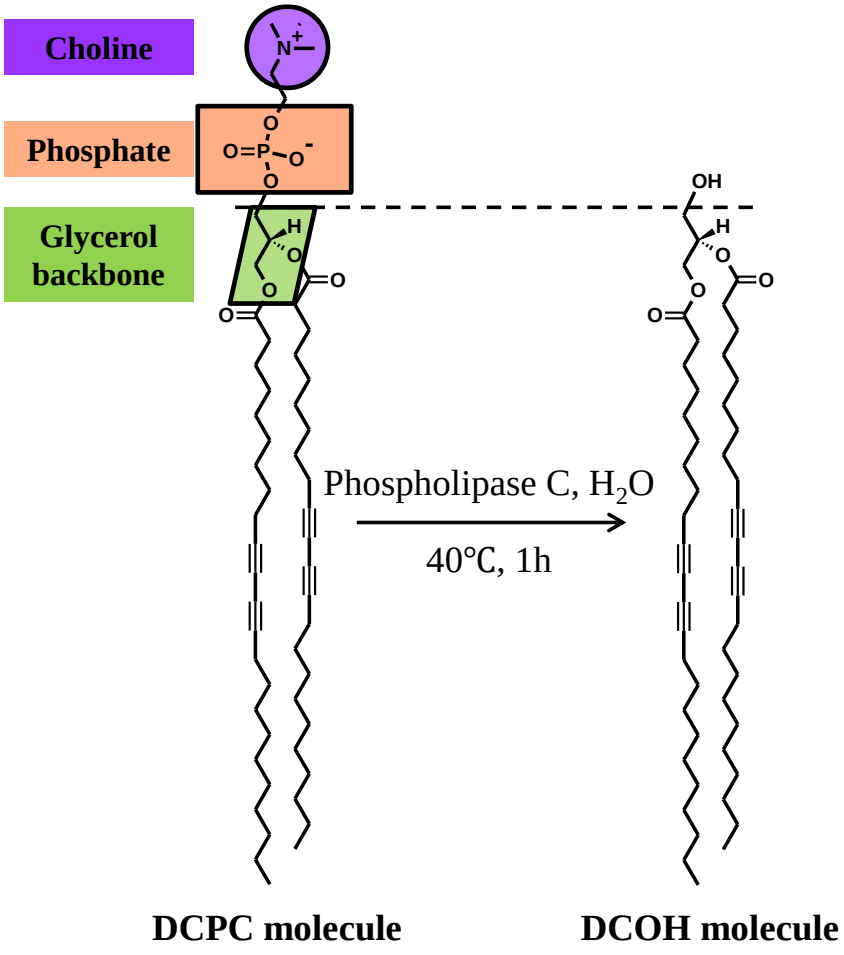

Figure 2.2. The synthesis process of OH-terminated lipid molecule (DCOH) from a commercialized lipid molecule, (DCPC). The polar head-group of DCPC was cleaved with phospholipase C to form OH groups.

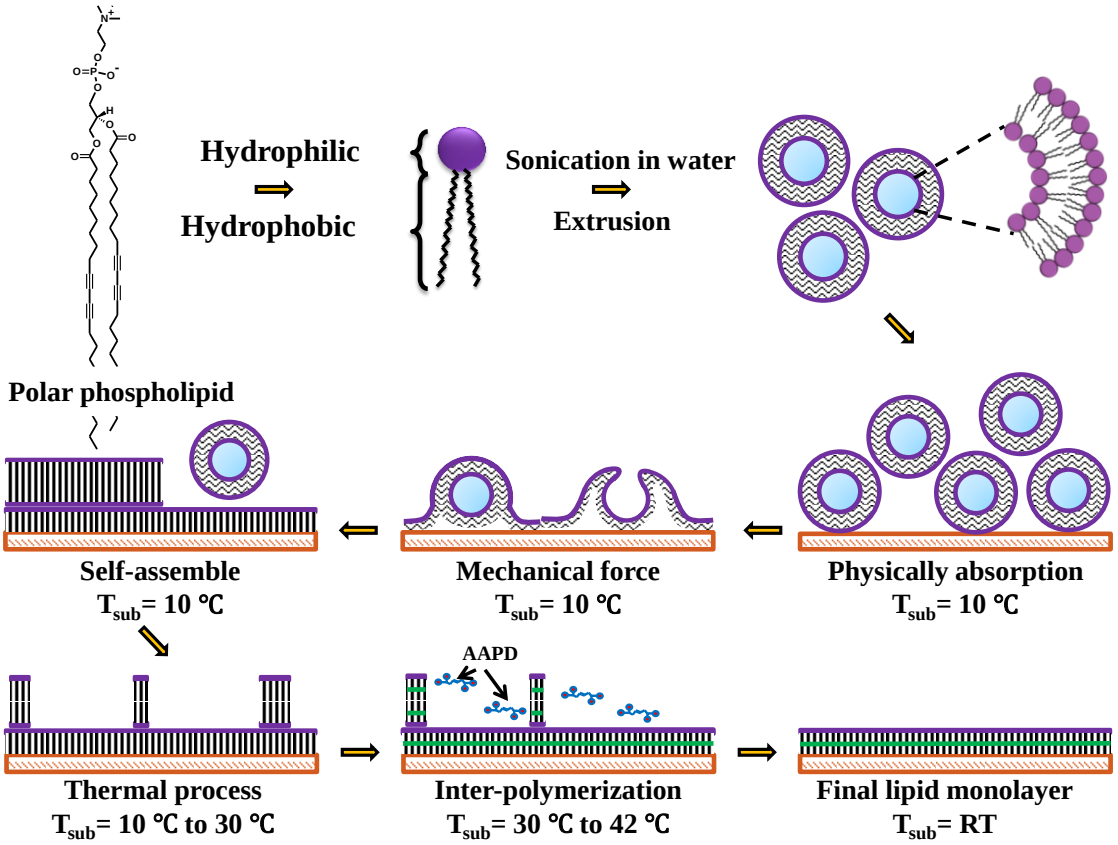

Figure 2.3. Schematic of lipid monolayer deposition process.

To deactivate the pH sensitivity of OH-head groups, the lipid monolayer was modified by MTS groups. This process is equivalent to the second polymerization at head groups of the lipid monolayer. **Figure 2.5** shows the process for the polymerization of head groups of the lipid monolayer at a molecular structure scale. The MTS solvent was diluted by 1,4-dioxane solvent and covered on the lipid monolayers for 15 minutes. Then, the device was rinsed with methanol to remove the residual solvent from the surface. Finally, the DC-MTS lipid monolayer formed on the P3HT film. For sensor applications, ion complexation or biomolecules will attach to MTS groups by silanization protocol.

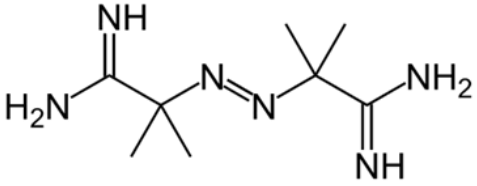

Figure 2.4. Chemical structure of AAPD

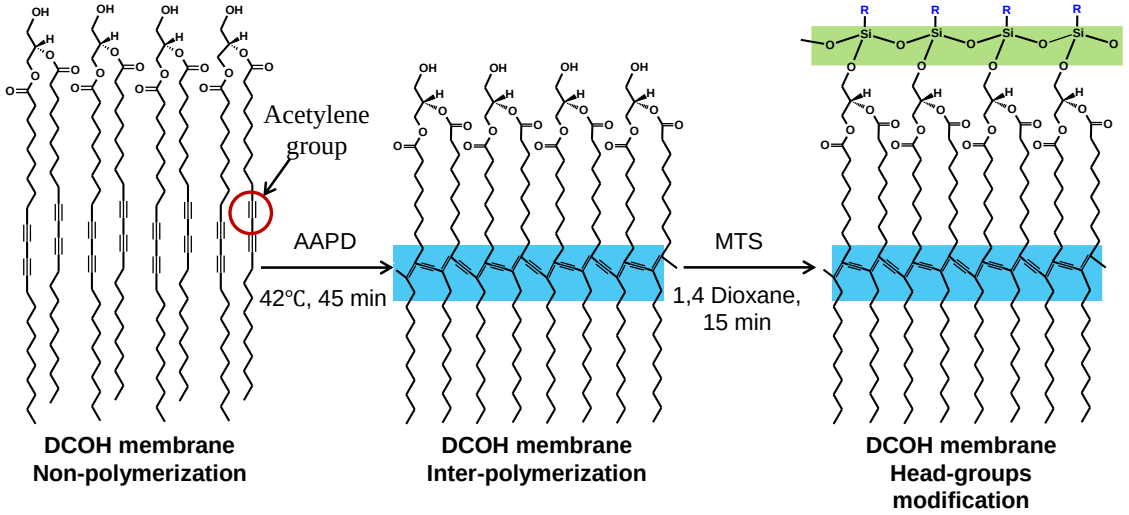

Figure 2.5. Illustration of process for the inter-polymerization at middle of lipid molecules and head-groups functionalization of DCOH lipid monolayer on P3HT film. R groups can be methyl groups, ion complexations or biomolecules.

The existence of the lipid membrane on the P3HT film was confirmed by attenuated total reflection Fourier transform infrared (ATR-FTIR) measurement. All measurements were conducted by using the Nicolet iS50 system at 4 cm^{-1} resolutions in the ambient condition. The set of two samples, the pristine P3HT film and the DCPC monolayer on the P3HT film were analyzed. Firstly, the pristine P3HT film was measured to get a background spectrum. Then, the P3HT film with the DCPC monolayer was realized. Finally, the FTIR spectrum of the DCPC monolayer was obtained by extracting from the background spectrum.

The surface properties of samples were characterized by using a microscope to observe the changes in water contact angle after lipid monolayer deposition. These measurements allow us to reconfirm the formation of lipid monolayer on the P3HT.

The ultra-thin thickness of lipid monolayer was estimated by X-ray reflection (XRR) measurements using Bruker AXS, D8 Discover systems**.**

The morphology of P3HT film before and after lipid monolayer deposition was evaluated by employing an atomic force microscope (Hitachi AFM SPI4000) in the tapping mode. Meanwhile, indentation measurements were realized using the NTEGRA atomic force microscope from NT-MDT spectrum instruments (Moscow, Russia) to evaluate the mechanical stability of lipid monolayer. Force measurements were

performed in water using NSC 38 cantilevers with a diameter of 8-10 nm and spring constant in a range from 0.1 to 0.3 Nm^{-1} (**Figure 2.6**). For each experiment, the force constant of the cantilever was evaluated using the thermal noise analysis method[35] after calibrating the tip deflection against a hard surface.

2.2.2. Principle of force measurement by AFM

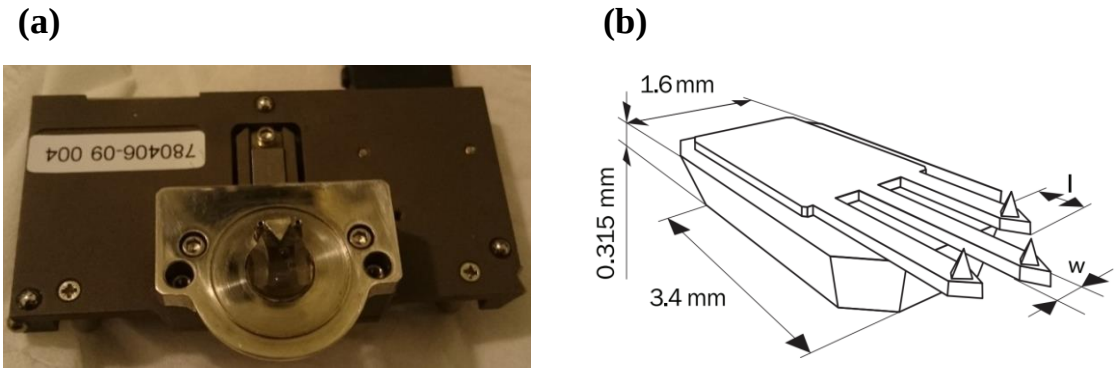

Figure 2.6. (a) The AFM probe is used to measure in water. (b) AFM cantilever for force measurement.[92]

The force measurement based on the AFM technique has been widely known as a useful tool to analyze the nanomechanical properties of materials and especially for thin films.[93–97] The AFM principle is based on the interaction between the AFM probe (**Figure 2.6**) and the surface of samples. The AFM probe consists of a tip and a cantilever, as seen in **Figure 2.7 (a)**. The motion of AFM tip, namely up/down and side to side, is recorded through the laser beam reflected off the cantilever.[93,94] A position-sensitive photo-detector (PSPD) is used to track the reflected laser beam to get the information about the vertical and lateral motions of the AFM probe.[93,94,98] For the force measurement, the bending of the cantilever and the position sensitivity are converted to the force (F) versus the surface-tip distance based on Hooke's law below.

$$F = k \cdot x \tag{2.1}$$

in which, k and x are the force constant of cantilever and the cantilever deflection, respectively.

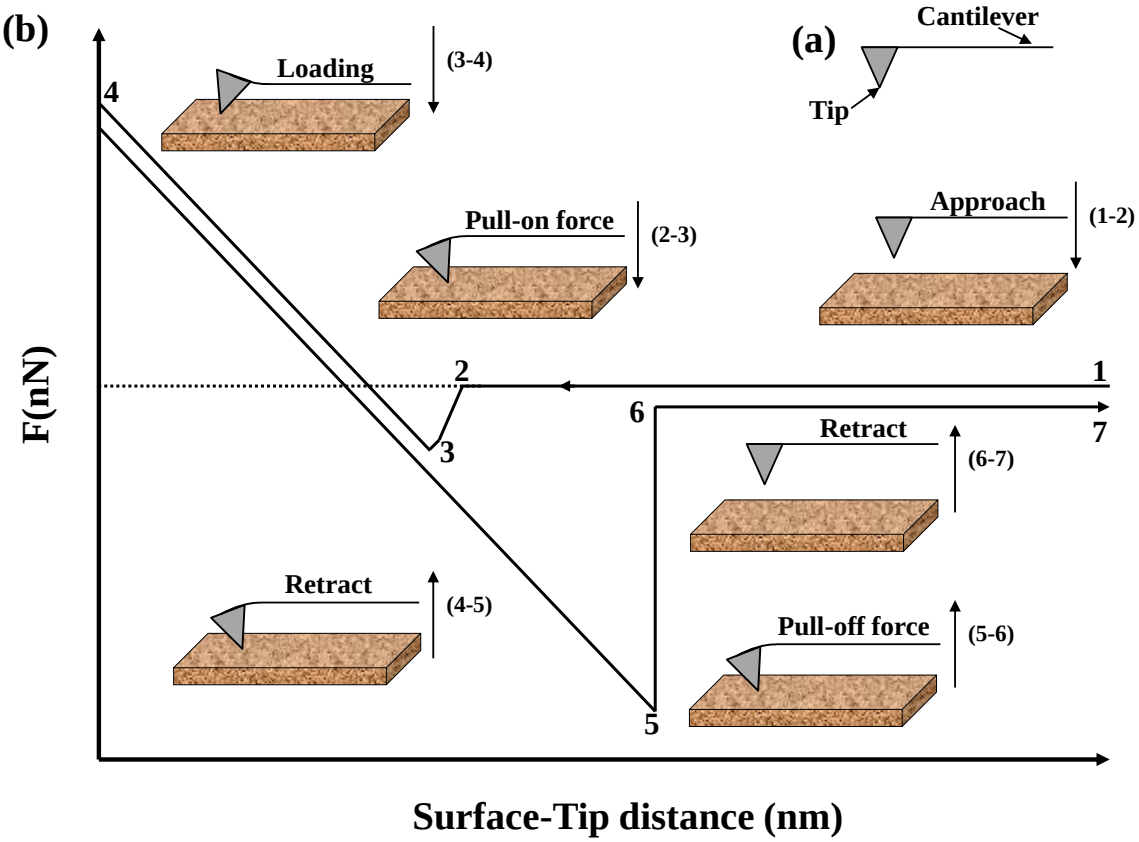

Figure 2.7. (a) The structure of AFM probe. (b) The schematic illustrates the mechanism of force measurement.

Figure 2.7 (b) illustrates a footprint of a tip from the approaching step to the retracting step in the force measurement process. During the approaching step, adhesive force attracts the tip toward the surface until there is contact between the tip and the surface. At this point, the tip continues applying a constant and default force upon the sample surface. Depending on the property of the material, the tip causes a difference in the indentation of the sample surface and the deflection of the cantilever.[99] Subsequently, the tip is retracted from the surface. During this process, the various adhesive force between the tip and the surface hinders the tip retraction.[99] Finally, the tip moves up from the surface with a force overcoming the adhesive force. The indentation force and the adhesive force can be directly taken from the force-distance adhesive force curve.

In this chapter, the force measurement is useful to investigate the properties of engineered lipid monolayers on P3HT films such as mechanical stability and the thickness of lipid monolayers.

2.2.3. Results and discussion

At the early stage of the lipid deposition process, I employed the DCPC lipid due to its commercial availability. Furthermore, DCPC lipids have the intrinsic polar head groups, including phosphate and choline groups. These groups are recognized explicitly by the FTIR method. Here, the spectrum of the lipid membrane was normalized by extracting a background spectrum of the pristine P3HT film. **Figure 2.8** shows the FTIR spectrum of DCPC monolayer on the P3HT film. We can identify the peaks which represented specific bonds C=O, C-N, and C=C in the lipid monolayer.[100–102] These results indicated the existence of the lipid membrane on the P3HT film.

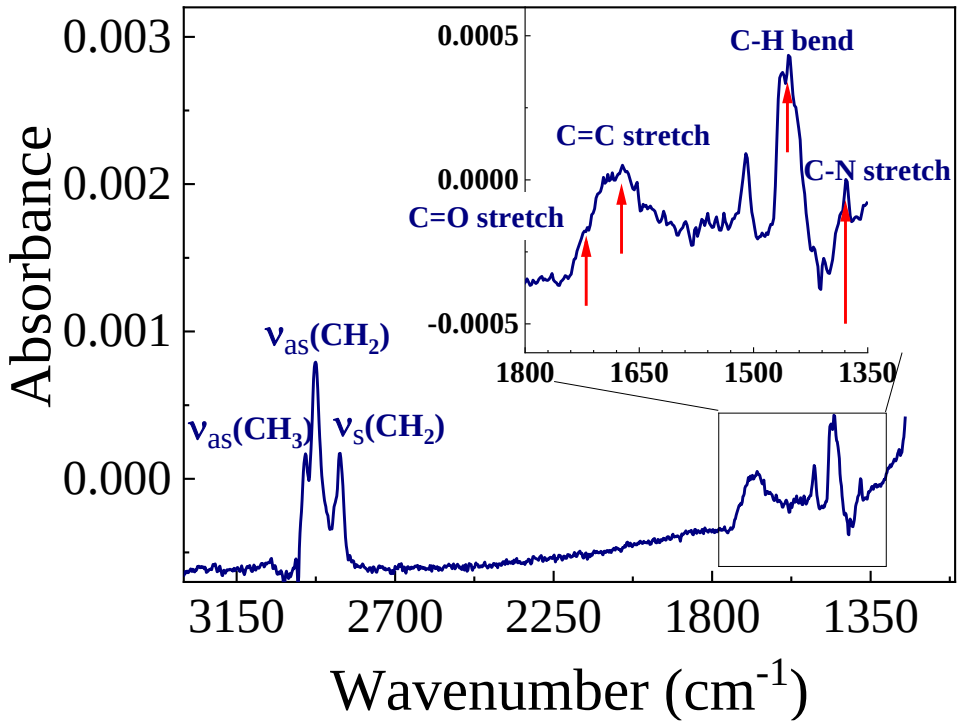

Figure 2.8. FTIR spectrum of a DCPC lipid monolayer on the P3HT film with representative absorption peaks of C=O, C-N, C=C bonds.

On the other hand, the surface property of the P3HT film changed significantly after covering by the lipid monolayer, as seen **Figure 2.9**. The water contact angle on the surface of samples decreased from 104° to 71° after the DCPC lipid deposition. The samples with DCOH lipids showed a similar contact angle with DCPC lipids. These results proved the surface property changed from hydrophobic of the P3HT film to hydrophilic of the lipid membrane. The results of FT-IR and water contact angle indicated that the lipid membrane successfully covered the P3HT film surface.

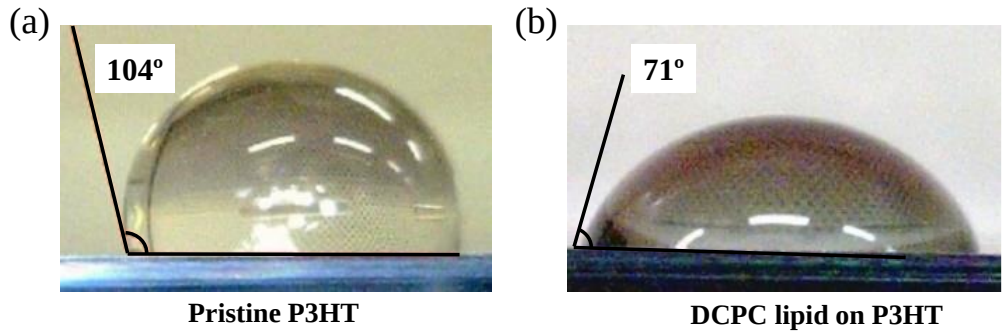

Figure 2.9. Contact angle of water droplet on (a) the pristine P3HT film (hydrophobic) and (b) on a DCPC lipid membrane (hydrophilic).

After the formation of the lipid membrane on the P3HT film was confirmed, the AFM measurements were conducted to evaluate the morphology of the P3HT film with the lipid membrane. AFM images showed the flat P3HT film surface without (**Figure 2.10 (a)**) and with (**Figure 2.10 (b)**) the DCPC lipid monolayer. The obtained surface roughness (RMS) values were 0.56 nm for P3HT film and 0.92 nm for DCPC lipid. P3HT films with DCOH and DC-MTS also had similar results with RMS values of 0.85 nm and 0.77 nm, respectively. These results proved that the uniform formation of the lipid monolayers on the P3HT film.

The thickness of the lipid monolayer was recalculated by using XRR measurements. The measurements were conducted on the same P3HT sample before and after lipid monolayer deposition. The models were fitted to the XRR data to obtain the information of thickness, density, and roughness of samples. **Figure 2.11** shows the fitted curve and raw curve of XRR measurements of P3HT samples with lipid monolayer. By using a fitting model, the calculated thickness of the lipid monolayer was approximately

2.13 nm. This result coincides with the thickness obtained from force measurement and other literature for lipid monolayer.[35,76] To sum up, the above results indicated that the stable lipid monolayer with the ultrathin thickness (2.1 nm) was successfully formed the P3HT film.

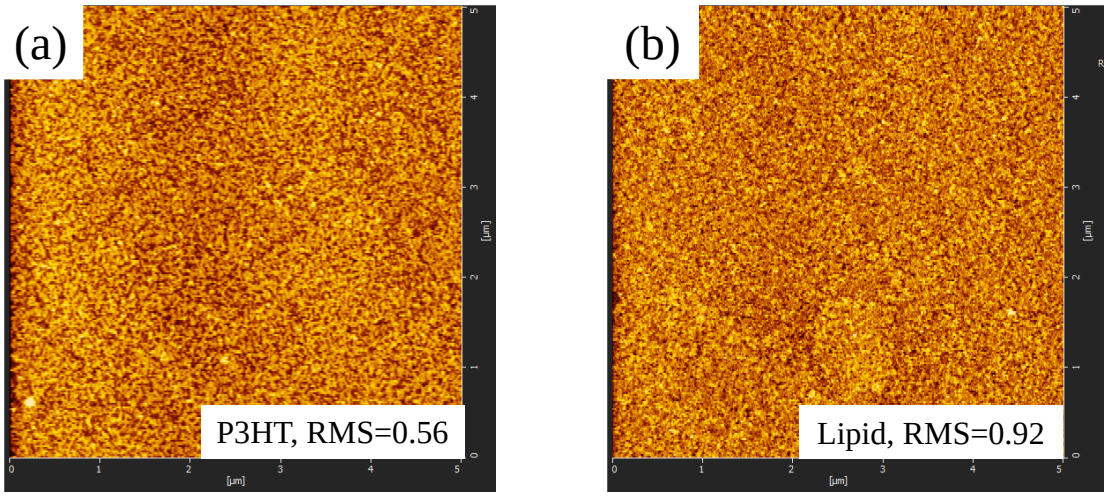

Figure 2.10. The surface morphology of (a) pristine P3HT film and (b) DCPC lipid monolayer on the P3HT film. The AFM images showed the uniform of P3HT film before and after lipid monolayer deposition.

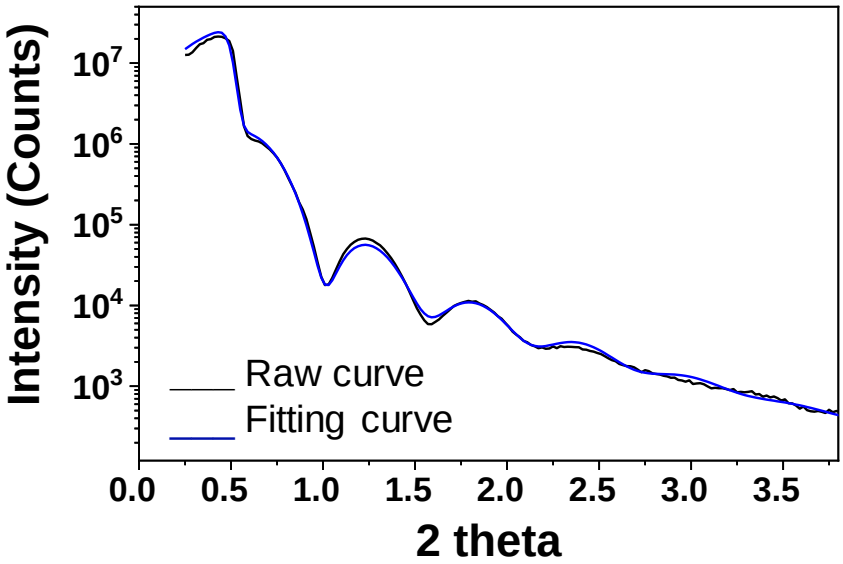

Figure 2.11. XRR spectrum of P3HT film sample with lipid monolayer.

In the next step, the effectiveness of polymerization on the nanomechanical stability of lipid monolayers was investigated by force measurements. Force measurements using AFM were realized on the DCOH lipid monolayers without inter-polymerization and DCOH after inter-polymerization and second polymerization at head groups. In typical force measurement, the AFM tip gradually approaches the sample from far away until the tip makes contact with the lipid monolayer. The tip keeps moving toward and causes the cantilever bending over the lipid layer. This process continues until the exerted force becomes large enough to rupture the lipid monolayer and reach the substrate. At this point, the jump height of the tip corresponds to the thickness of the layer under the compression of the tip. Both the values of break-through force and the jump height are utilized to examine the nanomechanical stability of lipid monolayer. **Figure 2.12** illustrates the representative force measurement process on lipid monolayer.

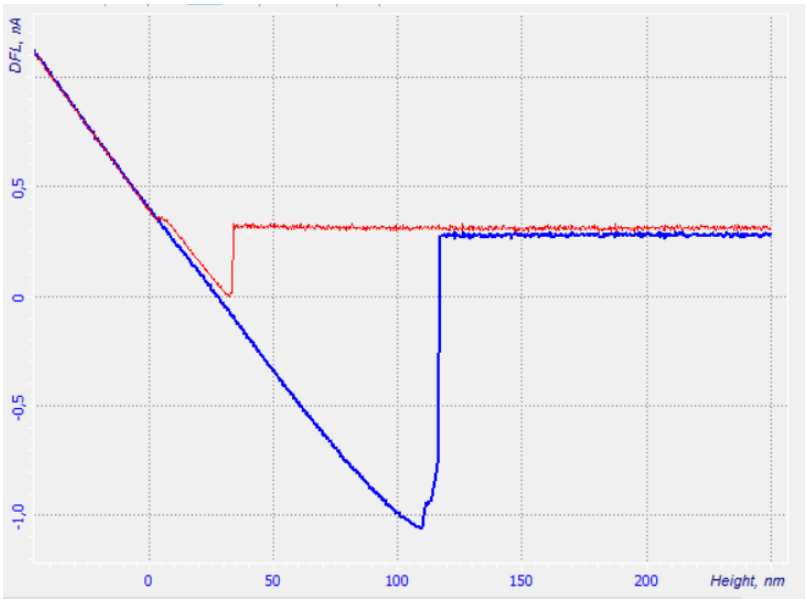

Figure 2.12. Representative force measurements loading curves obtained on the lipid monolayer after polymerization.

To evaluate the effectiveness of the polymerization on nanomechanical stability of lipid monolayer, a statistical analysis of break-through forces and tip jumps heights were realized, as seen in **Figure 2.13**. There was a clear difference between the rupture force of lipid monolayer before and after the polymerization process. The average force

to rupture the monolayer without polymerization is only approximately 0.27 nN. Meanwhile, the average rupture forces for the lipid monolayer after inter-polymerization and second polymerization required 1.1 nN and 2.2 nN, respectively. The rupture forces increased four and ten times higher than that of lipid monolayer without polymerization. Since a higher break-through force indicates a more stability layer, the data revealed the improvement of the nanomechanical stability of the monolayers after polymerization. The average thickness was 2.2 nm for the lipid membrane without polymerization and 2.0 nm for the lipid membrane with inter-polymerization. Meanwhile, after the modification by MTS, the thickness of the lipid membrane increased to 2.7 nm.

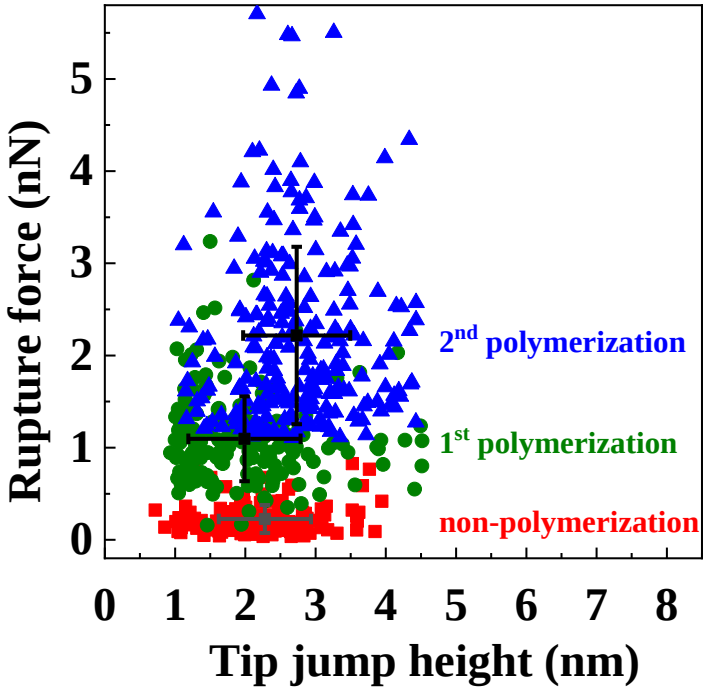

Figure 2.13. Break-through forces versus the tip jump in distance at the lipid monolayer rupture.

2.3. Capacitance of electrical double layer

2.3.1. Principle of electrochemical impedance spectroscopy

Electrochemical impedance spectroscopy (EIS) is a popular technique to investigate the electronic properties of materials and electrochemical systems.[103–105] Generally, EIS is measured by applying a small amplitude of AC (E) (~10-50 mV) on top of a controlled DC polarization potential to obtain the output current (I). **Equation 2.2** allows us to calculate the impedance (Z) of the system.[106]

$$Z = \frac{E}{I} = \frac{E_0 \sin(\omega t)}{I_0 \sin(\omega t + \varphi)} = Z_0 \frac{\sin(\omega t)}{\sin(\omega t + \varphi)} \quad (2.2)$$

where E, I and Z are a potential, a response signal and a complex impedance at time t, respectively. E_0, I_0 and Z_0 are amplitude of the signals. ω and φ are a radial frequency and a phase shift.

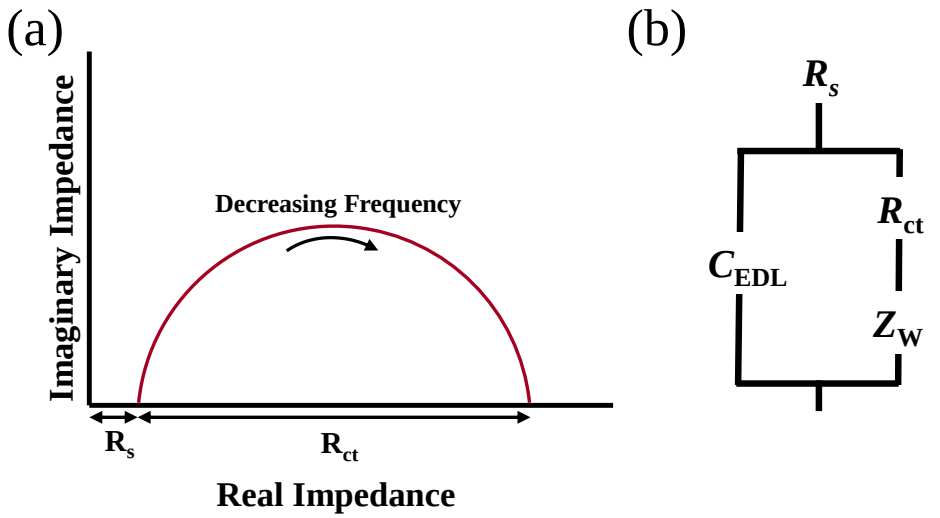

Figure 2.14. (a) Nyquist plot of simple EIS signal and (b) an equivalent circuit to evaluate the contribution of electrochemical processes in EIS.

The impedance results over a wide range of frequencies give a spectrum represented for different kinetics that may occur at the electrochemical system. Each of

kinetic is dominant at different frequency regions.[106] **Figure 2.14 (a)** shows the EIS signal displayed in the Nyquist plot.[103,105] In general, dipolar properties are realized at high frequencies. Meanwhile, bulk and surface properties are dominant at intermediate and low frequencies, respectively.[103,105,106] From a physical point of view, the complex impedance originates when an AC flows through an electrical circuit consisting of resistors, capacitors, inductors.[106] The impedance spectrum, therefore, can be expressed to an equivalent circuit. Randles circuit has been popularly used as an original equivalent circuit (**Figure 2.14 (b)**). This circuit includes the solution resistance (R_S), charge-transfer resistance (R_{CT}), double-layer capacity (C_{dl}), and Warburg impedance (Z_W). The R_S and Z_W relate to the properties of the electrolyte solution and mass transport of the electrolyte analytes, respectively. R_{CT} and C_{dl} are associated with the interfacial properties between solution-electrode.[107–109] EIS, therefore, is a powerful technique to investigate the intrinsic property of a material or a specific process that could affect the conductivity of the electrochemical system.[110] The application of this technique has become popular, from biochemistry up to organic electronics. In this dissertation, we use this technique to analyze the changes of capacitances of the electrical double layer at the interface by extracting from an equivalent circuit.

2.3.2. Experimental details

To estimate the mobilities of EG-OFETs, the capacitances of the EDL were calculated by the EIS measurements. The measurements were conducted on two kinds of capacitor structures (**Figure 2.15 (a)-(b)**) by using the Solartron system with a two-electrode configuration. The first structure composed of the pristine P3HT film on a gold substrate, directly exposed to the electrolyte, Au/electrolyte/P3HT/Au. The second one was the DC-glycerol coated on the P3HT film, Au/electrolyte/lipid/ P3HT/Au. The EIS was recorded in the 0.1 Hz to 1 MHz frequency range at an AC voltage of 50 mV. The phosphate buffer at a fixed pH of 6.86 was used as the electrolyte solution.

2.3.3. Results and discussion

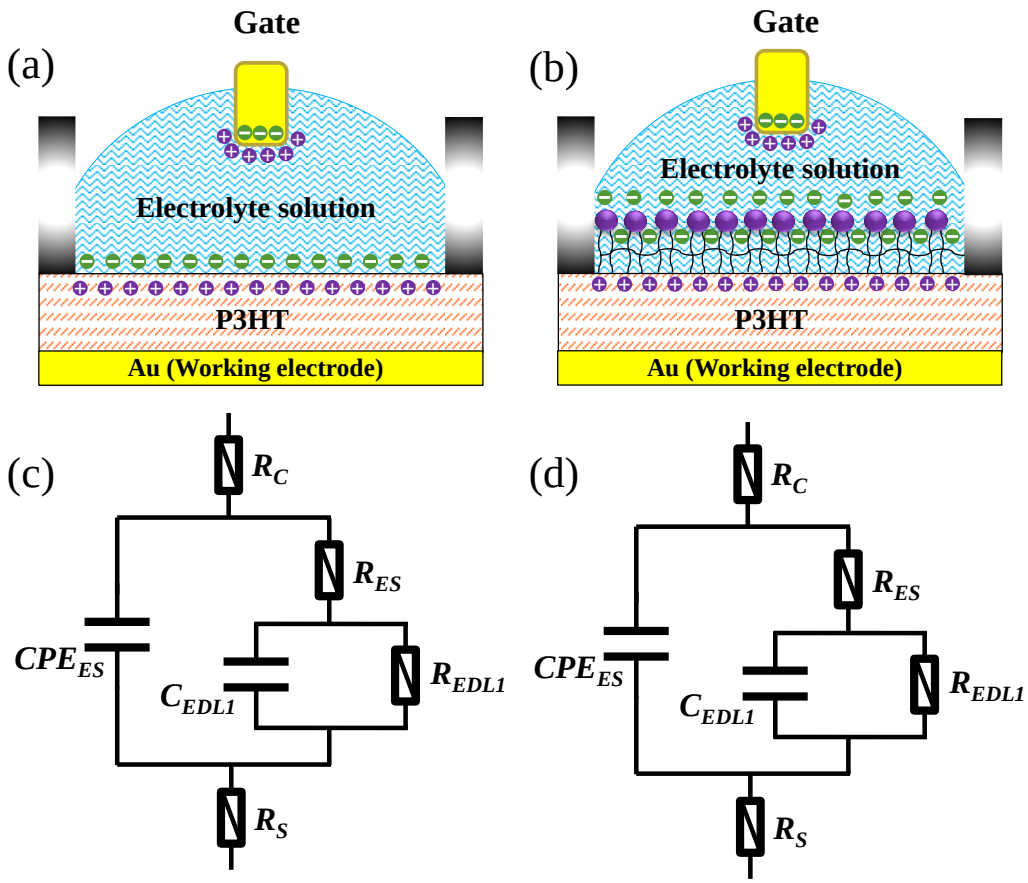

Figure 2.15. Illustrations of two capacitor structures and models of equivalent circuits for (a) and (c) Au/electrolyte/P3HT/Au; (b) and (d) for Au/electrolyte/lipid/ P3HT/Au. In the equivalent circuit, R_C is contact resistance, R_S is substrate resistance, CPE_{ES} and R_{ES} represent constant phase element and resistance of electrolyte solution, respectively. The C_{EDL} and R_{EDL} are capacitance and resistance of electrical double layer.

$$Z_{CPE} = Q^{-1}(j\omega)^{-\alpha} \quad (2.3)$$

If $\alpha = 1$, then Q = C and the Z_{CPE} is considered as an ideal capacitance. Meanwhile, $\alpha = 0$, $Q^{-1} = R$, Z_{CPE} turns into an ideal resistance.

Figure 2.16 showed the obtained EIS spectrum in Nyquist and Bode plots. It is noted that EIS data of two structures showed similar curves. The result can be explained by the relatively uniform of the lipid monolayer on the P3HT film. I, therefore, proposed a similar equivalent circuit for two structures (**Figure 2.16 (c)-(d)**).[110–113] The circuit consists of the contact resistance of Au electrodes with the electrolyte solution (R_S) and

the P3HT film (R_C). In the EIS spectrum, the contribution of two resistors can be considered as a serial resistor. Meanwhile, CPE_{ES} and R_{ES} represent a constant phase element and a resistance of electrolyte solution, respectively. The constant phase element (CPE) accounts for the inhomogeneity of EDL at the interface. The CPE is defined by an equation below.

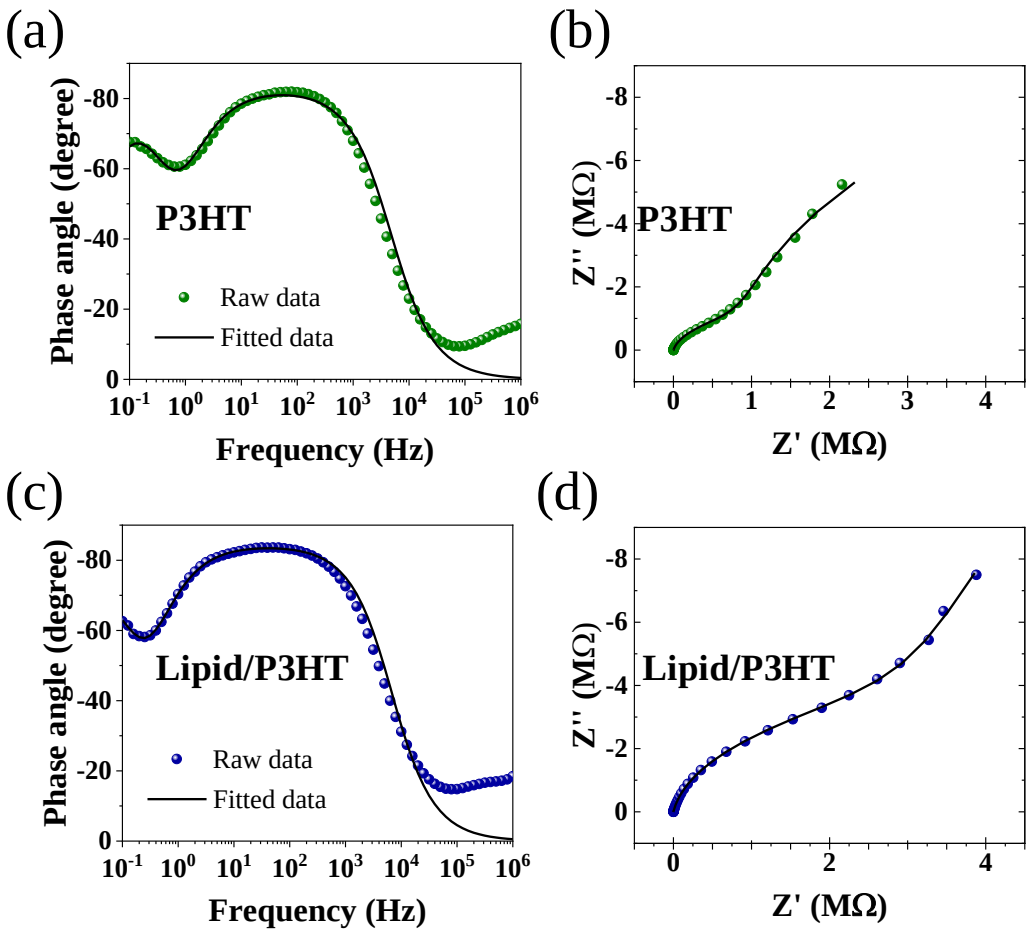

Figure 2.16. EIS data obtained by applying alternative current voltage, V_{AC}, of 50 mV and direct current voltage, V_{DC}, of -500 mV in a frequency range of 0.1 Hz to 1 MHz. a) Bode plot and b) Nyquist plot using the impedance of the pristine P3HT; c) Bode plot and d) Nyquist plot using the impedance of the lipid monolayer on the P3HTfilm. The circle pattern shows raw data and the black solid line represents the fitted curve using the corresponding equivalent circuit.

The capacitance (C_{EDL}) and resistance (R_{EDL}) of the electrical double layer are dominant at a low frequency. The C_{EDL} values, therefore, are considered as the capacitance of the gating layer of the EG-OFET. The extracted capacitance values were 16.25 μFcm^{-2} for the DCOH lipid and 20.5 μFcm^{-2} for the pristine P3HT. The contribution of other components (resistors and capacitors) was estimated by fitting the impedance spectrum with the equivalent circuits. The detail parameters were described in **Table 2.1.**

Table 2.1. Fitted parameters of electrochemical impedance spectrum of two structures extracted from the equivalent circuits.

Parameters	**P3HT**	**DCOH/ P3HT**
R_C (kΩ)	0.69	0.57
R_{ES}(MΩ)	4.05	6.38
R_{EDL} (MΩ)	24.9	87.0
C_{EDL} (μFcm^{-2})	20.5	16.25
C_{ES}(μFcm^{-2})	1.17	1.61

2.4. Conclusion

In summary, this chapter clarified the formation of the lipid membrane on the P3HT film. ATR-FTIR and water contact angle measurements confirmed the existence of lipid monolayer on the P3HT film. The chemical bonds of the lipid membrane were clearly realized in the FTIR spectrum. Meanwhile, the decline of the water contact angle showed the change from the hydrophobic property of P3HT film to the hydrophilic property of the lipid membrane. Furthermore, AFM images showed the flat surface of the P3HT film before and after lipid membrane deposition. Moreover, the polymerizations at middle and head groups of lipid molecules significantly improved the mechanical stability of the lipid membrane. The force measurements showed that the rupture forces of the lipid membrane increased four times for the first polymerization and ten times for the second polymerization. In addition, the thickness of the lipid membrane was realized

around 2.1 nm by the force and XRR measurements. This result was suitable for the thickness of the lipid monolayer. Moreover, EIS measurements showed that the lipid monolayer negligible affected the capacitance of EDL. These results indicated that the ultra-thin lipid monolayer was stably formed on the P3HT film and ready for steps later of sensor fabrication.

Chapter 3 The establishment of WG-OFET operation

3.1. Introduction

WG-OFETs have attracted considerable attention in recent years due to their excellent advantages for sensor applications. At the first stage of the sensor development based EG-OFET, DI-water is widely employed as an electrolyte solution. DI-water reduces the doping effect into the organic semiconductor, causing the degradation of the transistor performance.[33] This provides the advantage of optimizing the sensor structure. On the other hand, WG-OFET inherits many advantages from OFET, namely a high-throughput low-cost fabrication process, a large printable area on flexible substrates, and favorable integration with electronic circuits.[11,13,14] Additionally, OFETs offer the versatility of being able to realize high selectivity and sensitivity.[18–20] Because the three main components of transistor-based sensors, i.e., a probe, a transducer, and an amplifier can be integrated into one device. This merit greatly enhances sensitivity even with marginal input signals.[8,11,96,97] Another merit of WG-OFETs is the formation of an electrical double layer (EDL) at the interface between a solution and a semiconductor channel.[10,23] Due to a nanometer-order thickness, the EDL plays a critical role as a gating layer with an extremely high capacitance (1-10 μFcm^{-2}). WG-OFETs, therefore, can operate at the millivolt scale.[23,30,34,62,63] With these properties, WG-OFETs are excellent for the detection of ions and biomolecules in solution.[12,15,19,23,26,33,61,116] However, stable operation in an aqueous environment remains a challenge with WG-OFET-based sensors.[31,32,54]

In this chapter, I have been investigated the properties of WG-OFETs to obtain stable operation of the transistor in the aqueous medium. For this purpose, I examined the influence of three factors, namely the surface flatness of the semiconductor channel, the gate electrode metals, and the surface modification by the lipid membrane. The EDL is a key factor to control the gate capacitance of WG-OFET, which impacts the transistor performance. However, the thickness of EDL is very ultra-thin at the sub-nano scale. This layer, therefore, is strongly affected by the surface flatness of the P3HT film.[32,117,118]

Hence, the influence of the morphology of P3HT film on the transistor performance was investigated. Another important factor is the metal of the gate electrode. Each metal has an intrinsic work function value that can tune the threshold voltage of transistors.[85,119,120] In this study, I employed two electrodes, namely common tungsten (W) electrode and gold (Au) electrode. Finally, I investigated the influence of surface modification by the lipid membrane on the performance of WG-OFET.

3.2. WG-OFET transistor fabrication

3.2.1. Experimental details

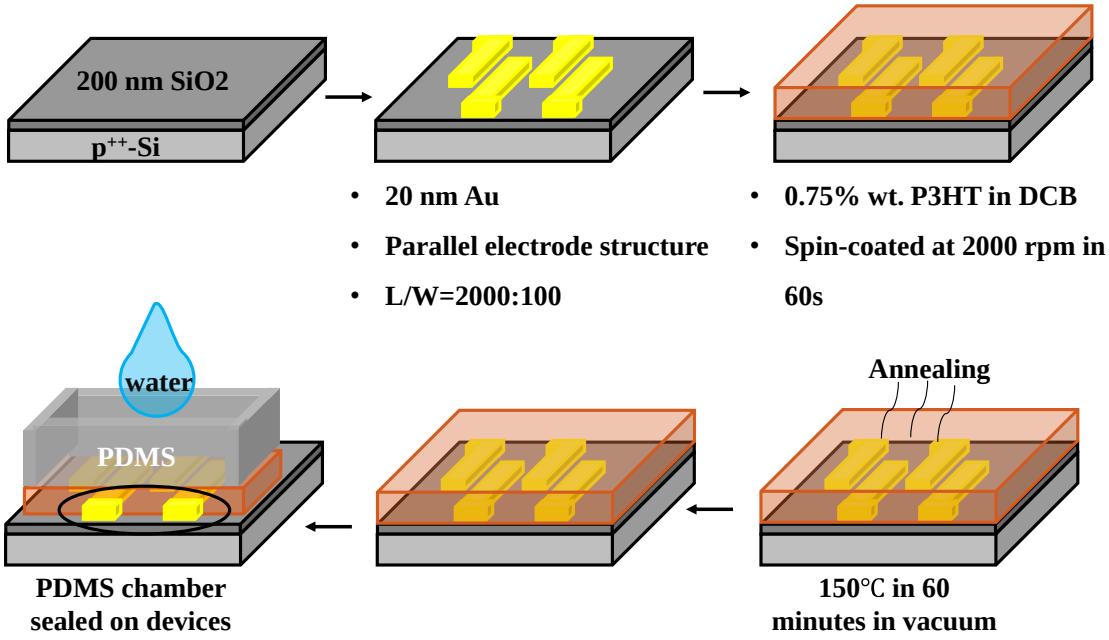

Figure 3.1. Schematic of transistors fabrication process

Figure 3.1 shows the schematic of the WG-OFET fabrication process. Si wafers covered by 200 nm-thick SiO_2 surface layers were used as substrates. Then, the source and drain electrodes were patterned on substrates through thermal evaporation in a vacuum. Finally, we obtained substrates with 22 nm-thickness of the gold electrodes on the surface. P3HT powder was dissolved in chlorobenzene with different weight percentages, followed by thermal heating at 60 ºC for 30 minutes to obtain the P3HT

solutions. After passing through filters with a 200 nm pore size, the homogeneous solution was slowly spin-coated onto the electrodes under ambient conditions. Subsequently, the P3HT film was annealed at 150 ºC in a vacuum. This step helped to eliminate residual solvent and improve the crystallinity of the P3HT films. Finally, a polydimethylsiloxane (PDMS) container for water was carefully sealed on top of the device. The tips of needle-shaped electrodes (Au and W) were placed in the water to supply the gate bias voltage. The lipid monolayer was coated on the P3HT film as described in **section 2.3**

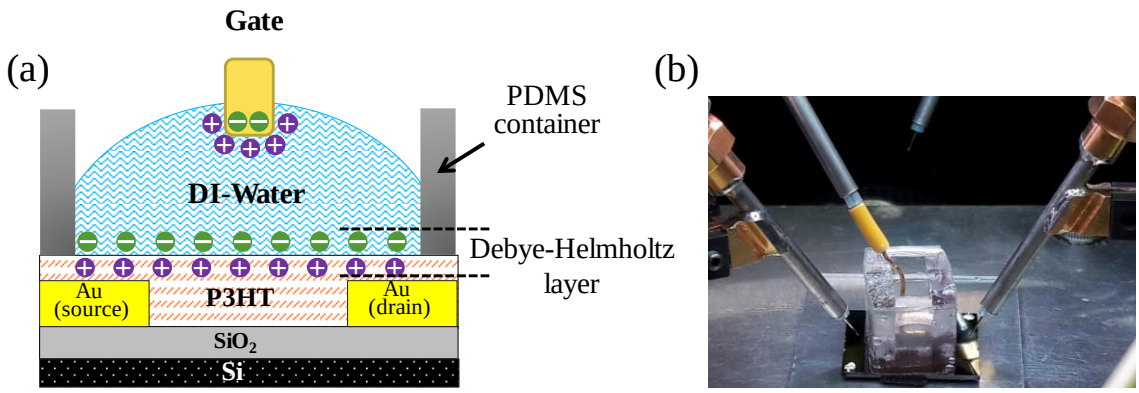

Figure 3.2. (a) Configuration of WG-OFET with an ultra-thin electrical double layer (Debye-Helmholtz layer) formed at the water/P3HT interface under a gate bias voltage. (b) Image of real device and setup of probes for electrical measurement.

I utilized the semiconductor parameter analyzer, Agilent B1500A, to measure electrical properties of transistors under ambient conditions. **Figure 3.2 (b)** showed the image of the real device and the setup of electrical measurements. Meanwhile, the surface morphology of P3HT films was observed by the atomic force microscope (Hitachi AFM SPI4000) in the tapping mode.

3.2.2. The influence of film morphology

Figure 3.2 (a) shows the coupling between charged elements in the organic semiconductor and ions in water forms an ultra-thin EDL at the interface. This layer is well known as a Debye-Helmholtz layer.[23] The EDL plays an important role in the operation of the WG-OFETs because it provides a very high gate capacitance enabling

millivolt operation.[23,30,34] The EDL has a nanometer order thickness, and therefore its capacitance depends strongly on the surface morphology of the semiconducting channel.[32,117,118] Hence, the flatness of P3HT films can have a significant impact on WG-OFET operation.

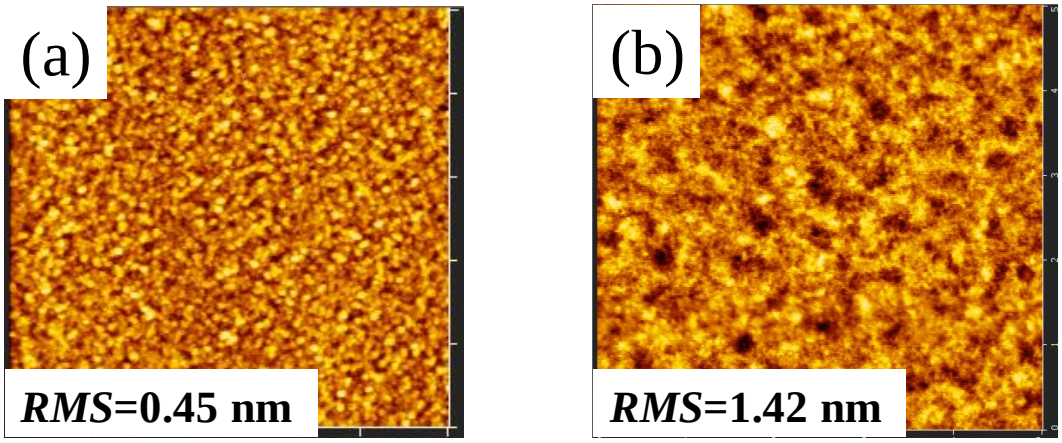

Figure 3.3. AFM images (5 μm×5 μm) of the P3HT films with the solution concentrations of (a) 0.75 wt% and (b) 2 wt%.

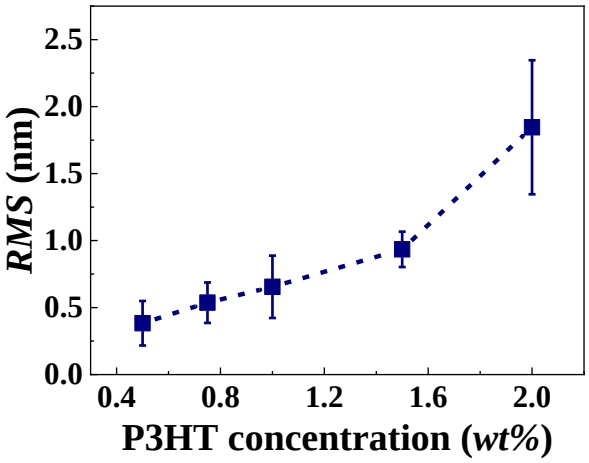

Figure 3.4. The effect of P3HT solution concentration (wt%) to the surface flatness (RMS).

Therefore, I investigated the WG-OFET properties with the different surface flatness of the P3HT film. For this purpose, I prepared the P3HT films with concentrations ranging from 0.5 to 2.0 wt%. **Figure 3.3 (a)** and **(b)** show the typical AFM images of P3HT films with concentrations of 0.75 and 2.0 wt%, respectively. There was a clear difference in the surface flatness. A high concentration (2.0 wt%) generated a rough

surface with small pinholes, dimples, and undulations that were remarkably observed. The RMS (root mean square), therefore, was three times higher than that of film fabricated by a low concentration (0.75 wt%) solution. **Figure 3.4** shows the dependence of concentration on the RMS. The surface roughness showed a monotonically trend with increasing solution concentration.

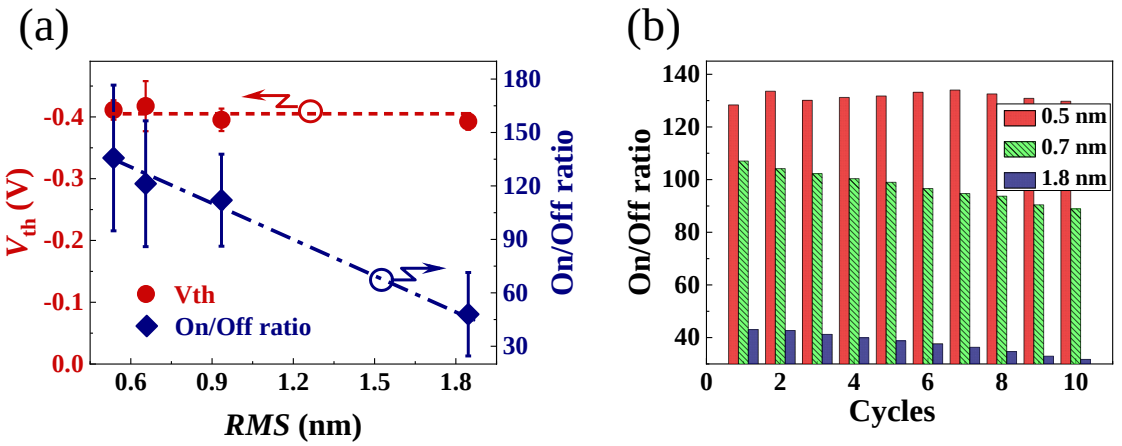

Figure 3.5. The influence of surface flatness on the WG-OFET performance. (a) The influence of surface flatness (RMS) on the V_{th} and on/off ratio. (b) The repeatability of the on/off ratio of devices with three surface flatness.

Figure 3.5 (a) shows the threshold voltage (V_{th}) and on/off ratio as a function of RMS. The V_{th} was the independence of the flatness. The V_{th} was constant at approximately − 400 mV. On the contrary, the on/off ratio decreased linearly with increasing RMS. The flat film showed the highest on/off ratio of 130. This is approximately three times higher than that produced from the film with an RMS of 1.8 nm. The flat surface had another notable advantage as regards the repeatability of the on/off ratio, as shown in **Figure 3.5 (b)**. A rough surface (RMS of 1.8 nm) showed a significant degradation in the on/off ratio after 10 measurement cycles. In contrast, a flat surface with a small RMS of 0.5 nm demonstrated a constant on/off ratio of around 130. The results are probably explained by observing AFM images. The rough surface has many dimples and holes, as observed in the AFM image. Therefore, water ions could be trapped or penetrate the P3HT film through these defective parts. These are the primary causes of the increase in the off-current, leading to the degradation of the on/off ratio. Consequently, a flat surface was

found to have advantages in terms of realizing a high on/off ratio with long-term repeatability.

3.2.3. The influence of metal of gate electrode

Besides the effect of flatness, the metals of the gate electrode can also improve the device properties, as reported in previous studies.[85,119,120] Each metal has an intrinsic work function that causes a shift in the threshold voltage (ΔV_{th}) according to the following equation.[121]

$$\Delta V_{\mathrm{th}} \approx \frac{\phi_{\mathrm{ms1}} - \phi_{\mathrm{ms2}}}{q} \tag{2.1}$$

where ϕ_{ms1}, ϕ_{ms2}, and q are the work functions of the gate electrode metals and the elementary charge, respectively.[23,85,122]

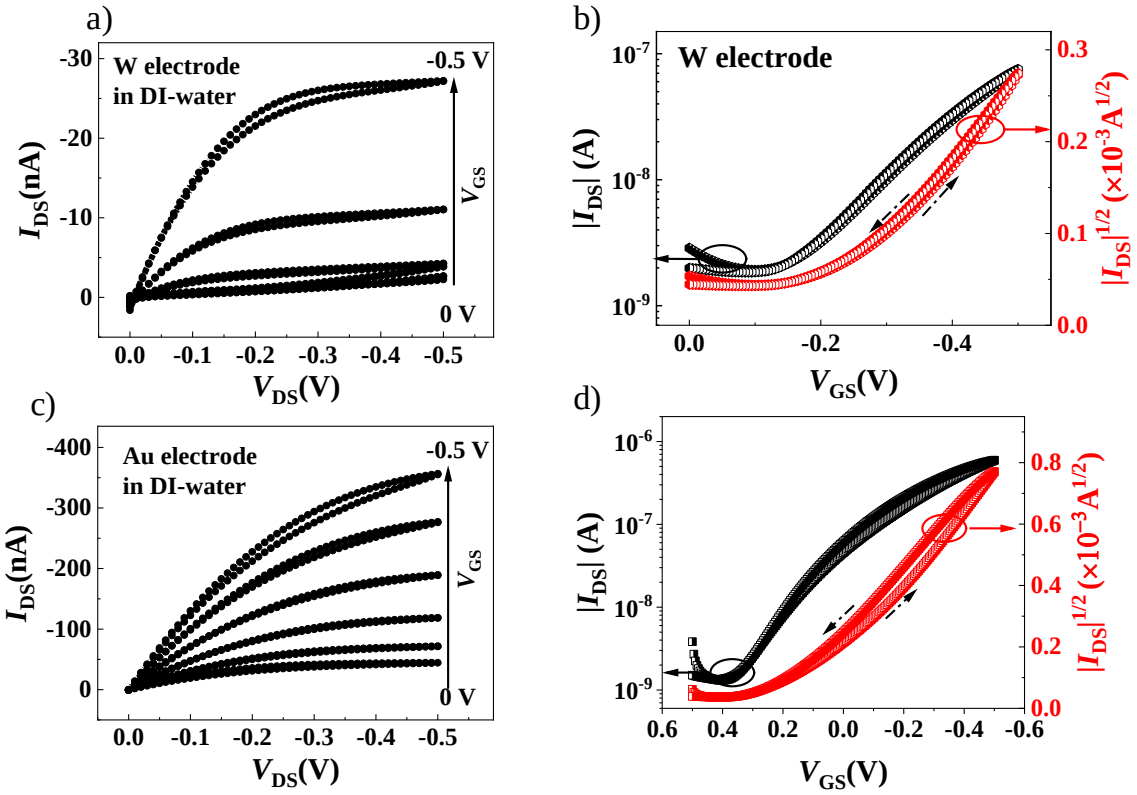

Figure 3.6. Influence of gate electrode metals on the WG-OFET performance. Output curves and transfer curves of WG-OFETs driven by (a)-(b) tungsten (W) and (c)-(d) gold (Au) electrodes.

In this study, I employed two metals: gold (Au) and tungsten (W) with work functions of 5.1 and 4.6 eV, respectively.[123,124] **Figures 3.6 (a)-(b)** and **(c)-(d)** show output curves and transfer curves obtained with the W and Au gate electrodes, respectively. Here, the bias voltages should be limited to the low voltage range to avoid the electrolysis of water and an undesired faradaic reaction.[31,33] Therefore, the transfer curves were measured under a constant drain voltage (V_{DS}) of − 0.5 V, and a gate voltage (V_{GS}) was applied to a maximum of − 0.5 V. In this mode, the V_{th} values were estimated with the **Equation 1.2**. A distinct impact of using Au electrodes was observed as a reduction in V_{th}. The V_{th} value was reduced from − 0.23 to + 0.07 V by replacing W electrodes with Au electrodes. As a result of this shift in V_{th}, the maximum drain current at a V_{GS} of − 0.5 V was greatly increased to 600 nA, which was almost 7 times larger than that obtained with a W electrode.

3.2.4. The influence of surface modification by lipid membrane

As discussed above, surface roughness, including holes, dimples, and undulation that affected the electrical properties of the WG-FETs. Therefore, surface modification with an inert molecular layer is expected to improve transistor performance. Here, the P3HT surface was coated with an ultra-thin lipid membrane, as described in **section 2.3**. Both of DCPC and DCOH lipid were employed to evaluate the influence of surface modification.

Figure 3.7 shows the performance of WG-OFETs coated by DCPC and DCOH lipids, respectively. All measurements used the Au electrode as the gate electrode. Both devices showed the transistor behavior of p-type, as seen in **Figure 3.7 (a)** and **(c)**. The transistor coated by the lipid membrane showed a clear difference in the performance with the pristine P3HT film. WG-OFET covered by lipid membrane showed a negligible hysteresis and a decrease in the drain current. The decrease of drain current can be explained by the reduction in the EDL capacitance. The introduction of a 2.1 nm-thick lipid membrane caused the reduction of total gate capacitance. The transistor, therefore, showed a decrease in the drain current by nearly one order. However, the WG-OFET with the lipid membranes demonstrated a narrow hysteresis loop in the transfer curve (**Figure 3.7 (b)** and **(d)**). Meanwhile, the large hysteresis at the transfer curve of the pristine P3HT

film was probably explained by charge traps inside or on the surface of the P3HT layer. The coverage from lipid membranes protected the P3HT surface from exposing directly to water to reduce such degradation of transistors.[26,80] Additionally, the combination of the Au gate electrode and DCPC lipid membrane coating resulted in the lowest threshold voltage of +35 mV. Meanwhile, the V_{th} of transistors with DCOH lipid monolayer was +60 mV. The slight difference in the V_{th} is probably caused by differences in functional groups of each type of lipid. These results indicated that the lipid membranes were useful in achieving the stable operation of WG-OFETs.

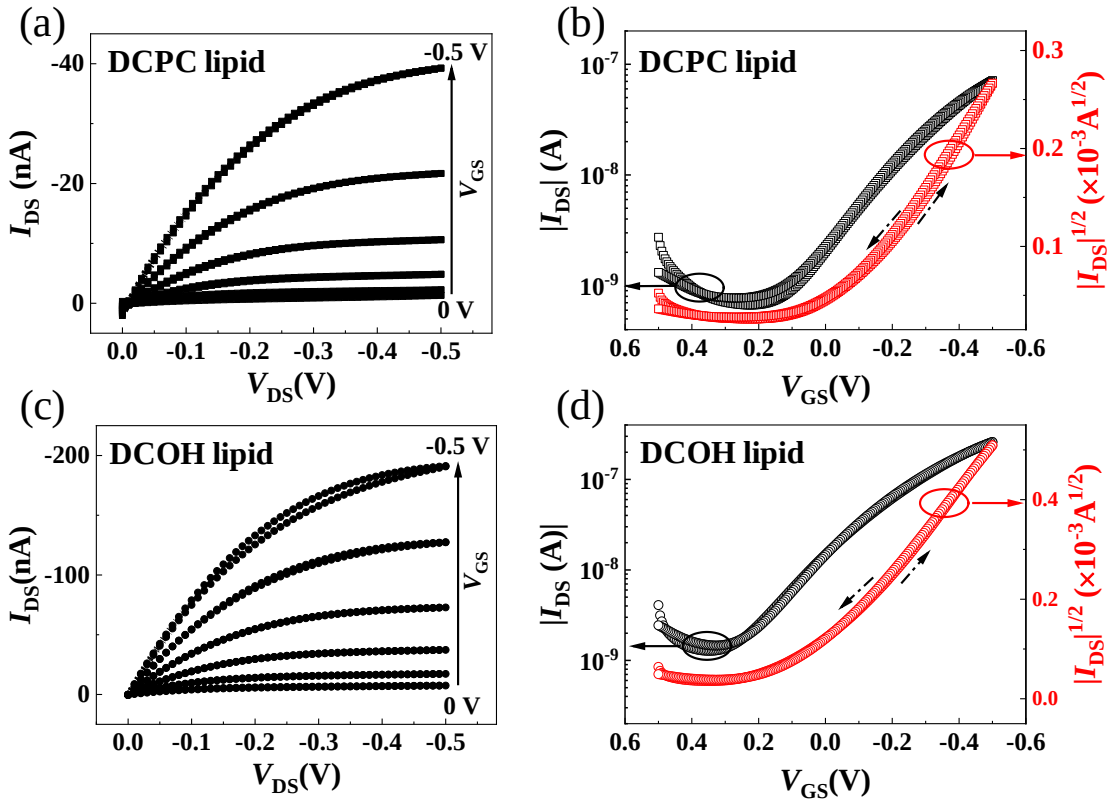

Figure 3.7. Influence of surface modification by lipid membrane on WG-OFET performance obtained using Au gate electrode. Output curves and transfer curves of WG-OFETs modified by (a)-(b) DCPC and (c)-(d) DCOH.

3.3. Conclusion

In this chapter, the fundamental operation of WG-OFET functionalized by a lipid monolayer was established. The de-ionized water (DI-water) was used as electrical gates in the transistors. The highly pure water is ion-free, minimizing the doping effect of ions on the P3HT channel layers. The electric double layers (EDLs) formed at the interface between water and channel plays an important role in allowing WG-OFET to operate on the millivolt range. Because of the sub-nanometer thickness, the EDL depends strongly on the surface morphology of the P3HT film. A flat surface reduced the off current as a consequence of the minimization of trapped ions in the P3HT film. As a result, the on/off ratio increased about three times and demonstrated long-term stable operation. Another key factor is the gate electrode metal to be immersed in water. The intrinsic work function of metal modulated the threshold voltage (V_{th}) of WG-OFET. The V_{th} was reduced from −0.23 V to + 0.07 V by replacing the metal from tungsten (W) to gold (Au). As a result of this shift in $V_{th,}$ the drain current with the Au electrode was increased almost seven times in comparison with that of the W electrode. However, there was a remarkable hysteresis loop in a transfer curve that probably caused by carrier trapping. To reduce this effect, an ultra-thin lipid monolayer was introduced on the P3HT surface. The WG-OFET functionalized by the lipid membranes showed a negligible hysteresis loop in the transfer curve.

Chapter 4 Sensors based on EG-OFET

4.1. Introduction

Cesium ions are popular sources of radioactive pollution. These ions are soluble elements and high mobility in aqueous environments. The pollutants, therefore, could be found at a very far distance from the source. The pollution from cesium ions has become more serious after the Fukushima Daiichi Nuclear Power Plant accident. Monitoring the level of cesium ions in waters in large areas, therefore, is an urgent requirement for marine life and human safety.[38] However, conventional techniques are limited, as discussed in section 1.1. Therefore, I aim to develop a new sensor for the detection of cesium ion is necessary.

EG-OFETs have many advantages for sensor applications, as mentioned above.[10,29] The importance is that the EG-OFETs effectively work at the millivolt range. This is due to the high capacitance (1-20 μFcm^{-2}) [29,30] of EDL formed at the interface between the electrolyte solution and the organic semiconductor. This merit leads to an ultra-low threshold voltage (V_{th}), which is monitored as output signals of the sensors. It should be noted that V_{th} is highly responsive to surface charges that originated from analytes such as ions or biomolecules.[20,25] Ultra-low V_{th}, therefore, is advantageous to detect even small signals. With these features, EG-OFETs are suitable for the detection of ions and biomolecules in the aqueous environment. However, to achieve highly sensitive and selective sensors in water, the sensors based on EG-OFET have to solve the following serious challenges. The first issue is the stable operation of transistor in liquid medium containing many interfering ions, e.g., potassium and sodium. These ions are well known to degrade the transistor performance because they act as electrical dopants for OFETs.[29,30] These ions are typically existence in practical samples. Second, cesium probes should be well attached to the surface of the transistor channels for detecting analytes such as ions and proteins.

In this chapter, I developed the new EG-OFET-based sensor for the detection of cesium ions in water. The EG-OFETs with engineered lipid membranes are proposed to

solve the above issues. The DCOH lipid molecules were used to functionalize the P3HT film. The ultra-thin DCOH monolayer (2.1 nm) was introduced at the interface between the electrolyte solution and the P3HT film. A striking point is that the lipid monolayers protect the transistor channels from direct contacting to the electrolyte solution. Lipid monolayers, therefore, can enhance the stable operation of transistors even in the electrolyte solution by reducing the electrochemical doping into the organic semiconducting layer. However, OH-lipids were sensitive to pH changes in a range from 4 to 12. This is a disadvantage for ion sensor applications. The effect of pH sensitivity can distort the sensitivity of the ion sensor. I, therefore, modified the OH-groups to eliminate this side effect. MTS groups replaced the OH-groups through the silanization protocol. To prove tunable of pH sensitivity by head-group, I investigated the stability, repeatability, and sensitivity to pH levels of the EG-OFETs with different head-groups of the lipid monolayers. The DCOH and DCPC lipid monolayers were sensitive to pH level because their head-groups changed the surface charges with the variation of pH level.[20,58,125–130] On the other hand, MTS-terminated lipid monolayers were no longer sensitive to pH levels and stable operation even with the presence of high ion concentration in the electrolyte solution.

Finally, the OH-groups of lipid monolayer can be utilized as a platform to attach cesium probes for the detection of cesium ions sensor. The cesium probes can be grafted on DCOH lipids through the silanization protocol for sensor applications. The performance of the sensor was examined for the detection of cesium ions in PBS and the synthetic seawater.

4.2. Mechanism of sensor based on electrolyte-gated OFET

Figure 4.1 shows the schematic of the sensing mechanism of the sensor based on EG-OFET. As the target analytes are captured by probes on the surface, the surface charges change. This causes the variation of the threshold voltage of transistors. The shift of threshold voltage (ΔV_{th}) can be estimated by using the equation below.[53,131]

$$\Delta V_{th} = \frac{Q}{C_{tot}} \tag{4.1}$$

where, Q is the change of surface charges, C_{tot} is the total capacitance at the interface. Additionally, the surface charge difference depends on the logarithm of the ions concentration at the surface.[20,131,132] Therefore, the shift of V_{th} is the dependence of ion concentration captured at the interface. Based on the shift of V_{th} corresponding to the changes of analytes concentration, we can build the calibration curve of the sensor.

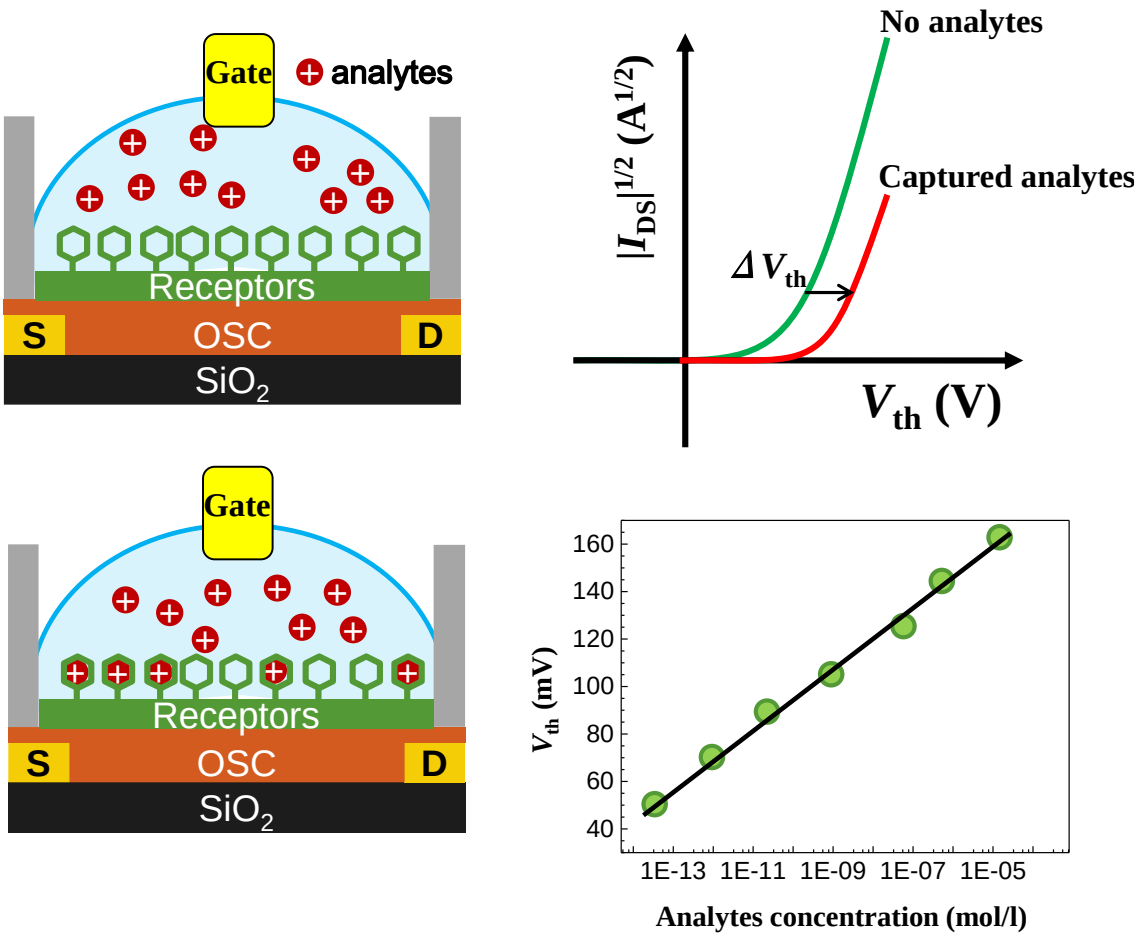

Figure 4.1. The schematic of sensing mechanism based on EG-OFET

4.3. Performance of EG-OFETs with different lipid monolayers

4.3.1. Experimental details

The EG-OFETs were fabricated according to the procedure of WG-OFET described in **section 3.2**. In this experiment, the phosphate buffer solution at a fixed pH level of 6.86 was replaced the DI-water to be used as the electrolyte solution to evaluate the performance of EG-OFETs. For pH sensitivity, other standard pH solutions purchased from Sigma Aldrich was used as the electrolyte solution.

The lipid membranes of DCOH and DCPC were coated on the transistors by vesicle protocol (**section 2.3**). For tuning of pH sensitivity, the DCOH was further functionalized by using MTS through the silanization protocol.[35] The detail of the process was described in **section 2.3**. The schematic of the functionalization process illustrates in **Figure 2.5.** Finally, for the ion sensor, the Cesium probes were grafting on OH-terminated lipids by using the same protocol with MTS. The sensor sensitivity was examined with different concentrations of Cesium ion in the solution containing potassium and sodium.

4.3.2. The influence of lipid monolayers

Figure 4.2 shows the structure of the EG-OFET, the molecular structure of three kinds of lipid monolayers. It should be noted that each lipid monolayer has a unique head group. The first lipid monolayer is phosphocholine (DCPC) lipids. This lipid has a zwitterionic head group, which is composed of a negative charge of phosphate (PO_4^-) group and a positive charge of trimethylamine ($N^+(CH_3)_3$) group. The second one is DC-glycerol (DCOH) lipid monolayer, which is synthesized from DCPC lipids. The zwitterionic head group is exchanged by the neutrally charged OH-functional groups. The last one is DC-MTS lipid monolayer. The OH-functional groups are further functionalized by MTS groups through the silanization protocol.

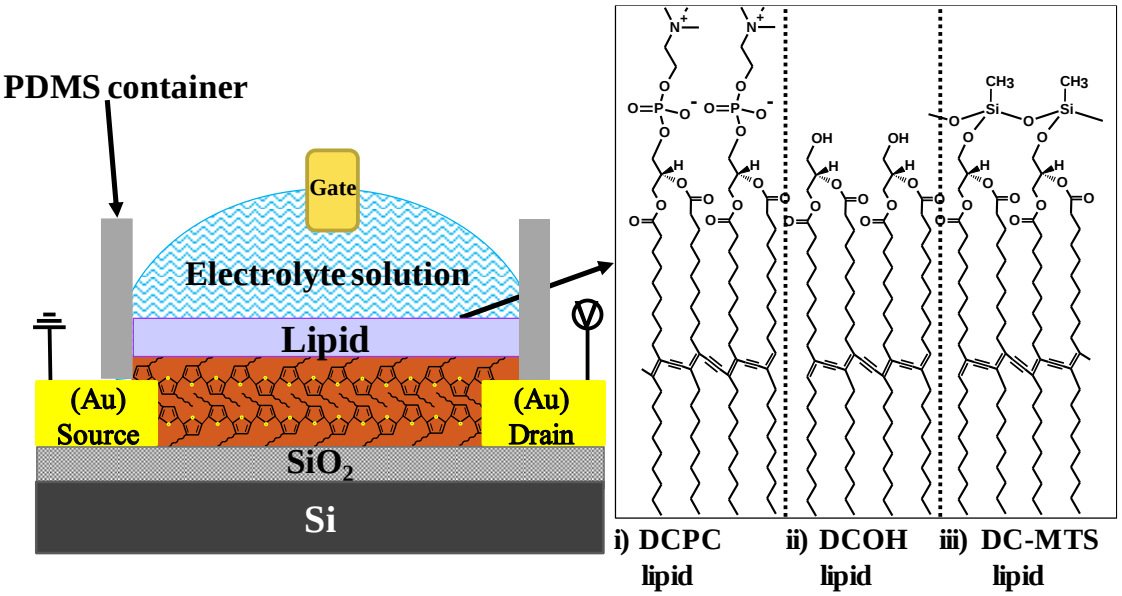

Figure 4.2. The EG-OFET structure with three kinds of lipid monolayers. The molecular structures of respective lipids, i) DCPC, ii) DCOH and iii) DC-MTS, are shown on the right side.

Firstly, the fundamental properties of three kinds of EG-OFETs were investigated. The phosphate-buffered solution with a fixed pH of 6.86 was used as the electrolyte solution. **Figures 4.3, 4.4,** and **4.5** showed the drain current (I_{DS})-gate voltage (V_{GS}) curves of the pristine P3HT without LMLs and the P3HT with respective LMLs (DCPC and DCOH), respectively. The gate voltage was swept from +0.4 V to −0.5 V at a fixed drain voltage of – 0.5 V. These curves indicated that all of the transistors exhibited p-type operation. The V_{th} was calculated with **Equation 1.2**.[133] The V_{th} of the pristine P3HT transistor was estimated to be + 70 mV. Meanwhile, those of the transistors with DCOH and DCPC lipid monolayers were −29 mV and +24 mV, respectively. Although there were slight differences in the V_{th} values, three devices showed the ultra-low threshold voltage (V_{th}).

There were clear differences in the forward and backward potential sweeps of these curves. A large hysteresis was observed around the low gate bias range of +0.4 to 0 V in the curve of the pristine P3HT (**Figure 4.3**). Meanwhile, the EG-OFETs functionalized by the lipid monolayers showed a negligible hysteresis in the loops, as seen in **Figures 4.4** and **4.5**. The large hysteresis in the pristine P3HT can be explained to the ion doping from the electrolyte solution into the P3HT channel during the potential sweeps. Meanwhile, the lipid monolayers protected the P3HT channel from this

electrochemical doping effect. This benefit of the lipid monolayer was represented in the long-term operation, as described below.

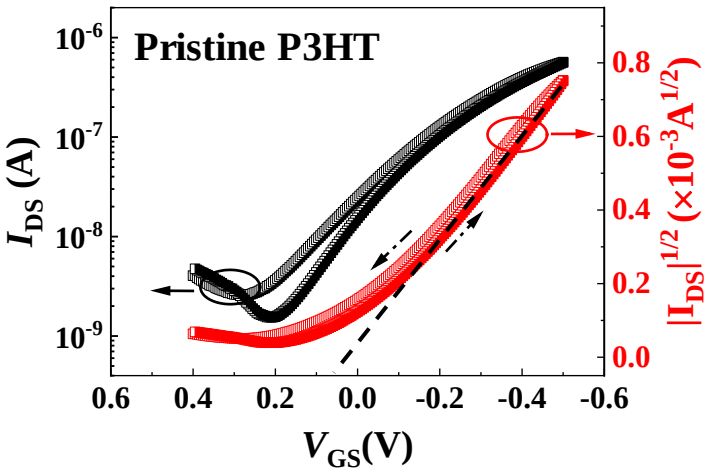

Figure 4.3. Transfer curves of EG-OFETs with pristine P3HT

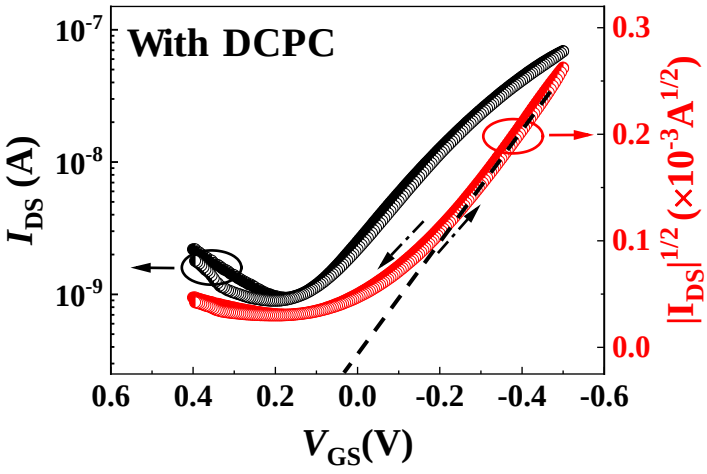

Figure 4.4. Transfer curves of EG-OFETs with P3HT with DCPC layer

For sensor applications, the long-term operation stability in the electrolyte solution is essential. The operation stability of three devices was evaluated by repeating measurements of ten cycles for two hours in the electrolyte solution. The gradual decrease in V_{th} with significant deviation in the pristine P3HT EG-OFET was observed, as seen in **Figure 4.6 (a)**. The ΔV_{th} was defined by the difference between the lowest V_{th} values to other V_{th} values. The doping from the electrolyte solution into the P3HT channel is

probably the main reason for this result. In contrast, both lipid monolayers improved the stability of the EG-OFET for long-term measurement. There were no shifts in V_{th}, as seen in **Figure 4.6 (b)** and **(c)**. Additionally, the deviations at each cycle were negligible. The lipid monolayer showed the effectiveness in the reduction of the ion doping into the P3HT channel. This is a significant advantage for the stable operation of EG-OFETs in the electrolyte solution.

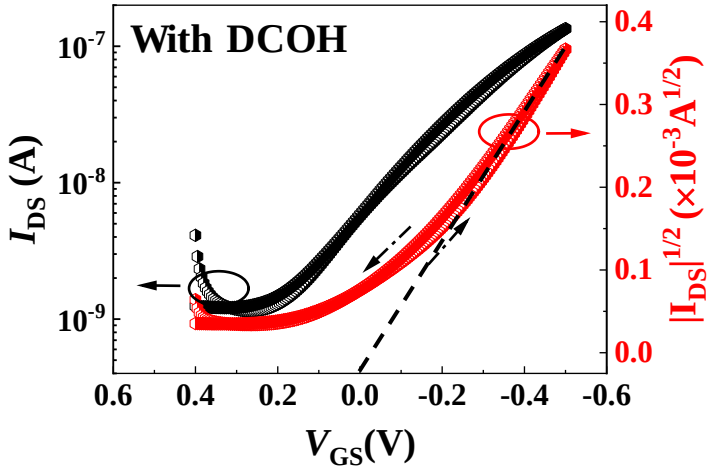

Figure 4.5. Transfer curves of EG-OFETs with P3HT with DCOH layer.

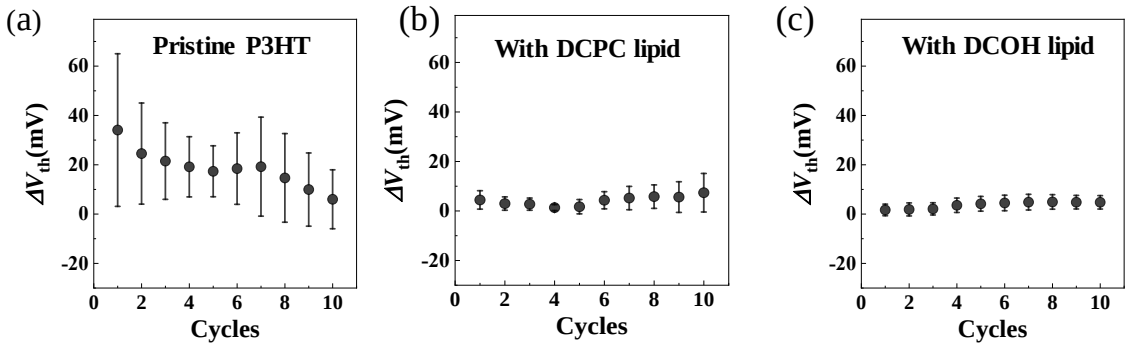

Figure 4.6. The variations in threshold voltage (ΔV_{th}) with repeated transistor measurements: (a) pristine P3HT (b) P3HT with DCPC lipid monolayer (c) P3HT with DCOH lipid.

Here, we should refer to the carrier mobility because this parameter is one of the most important properties of the transistors. For this purpose, the gate-dielectric capacitance of the EDL was estimated by the electrochemical impedance spectroscopy (EIS) measurement. The details of EIS (**Figure 2.16**), corresponding equivalent circuits

(**Figure 2.15),** and fitting parameters (**Tables 2.1**) were described in **section 2.3**. The estimated capacitance of the lipid monolayer on the P3HT film (16.25 μFcm^{-2}) was smaller than that of pristine P3HT film (20.5 μFcm^{-2}) due to the presence of the lipid membrane. The carrier mobilities were calculated by **Equation (1.2)** to be 7.2×10^{-3} cm^{2}V^{-1}s^{-1} for pristine P3HT and 4.3×10^{-3} cm^{2}V^{-1}s^{-1} for P3HT with DCOH, respectively. The estimated carrier mobilities are comparable to those in literature, reported in the P3HT-based EG-OFETs.[30,134] This result suggested that the lipid monolayers had a moderate impact on carrier transport in the channel layers.

4.3.3. Design of head groups of lipid monolayers for pH sensitive

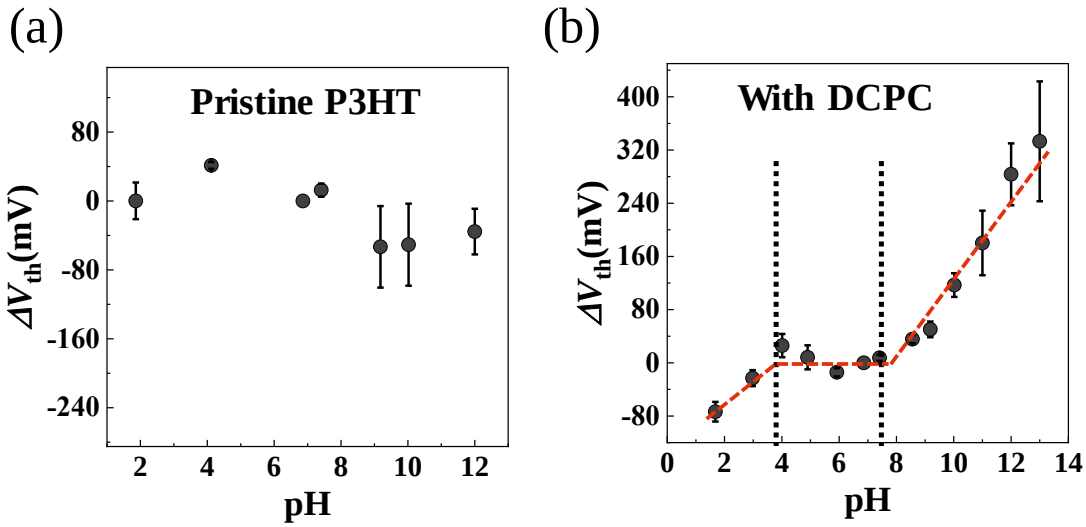

Figure 4.7. Variation in threshold voltage (ΔV_{th}) of EG-OFET operating in electrolyte solutions with different pH levels: (a) pristine P3HT and (b) P3HT with DCPC lipid.

For sensor applications, the control of pH sensitivity is a critical meaning. Therefore, we would like to design the head groups of LMLs for tuning pH sensitivity. I examined the pH sensitivities of EG-OFETs functionalized by two kinds of lipid monolayers, DCOH and DCPC for pH sensors. Meanwhile, the EG-OFET with a pristine P3HT channel was evaluated as a reference. The V_{th} of EG-OFET measured at pH 6.86 was used as an initial value. The variation in the V_{th} (ΔV_{th}) was defined by the difference between this initial value to the V_{th} of EG-OFETs at other pH values. The pH level in a range from 1.68 to 13 was used for examination. The pH-buffered solution of 100 μL was

poured into a PDMS container placed on the transistors. The transfer curves were scanned in the V_{GS} range of 0 to −300 mV at fixed V_{DS} of −300 mV. To avoid any electrolysis process caused by pH variation, the low range of V_{GS} is necessary.[34] The significant differences in ΔV_{th} were observed in **Figure 4.7 (a)-(b)** and **Figure 4.8 (a)**. There was no dependence of V_{th} on the pH level in the pristine EG-OFET (**Figure 4.7 (a)**). This was because of the non-pH sensitivity of the alkyl chains of the P3HT film. However, the pristine EG-OFET showed significant deviations of ΔV_{th}. This result can be explained by the doping of electrolyte ions leading to the unstable operation of the pristine EG-OFET in pH (electrolyte) solution.

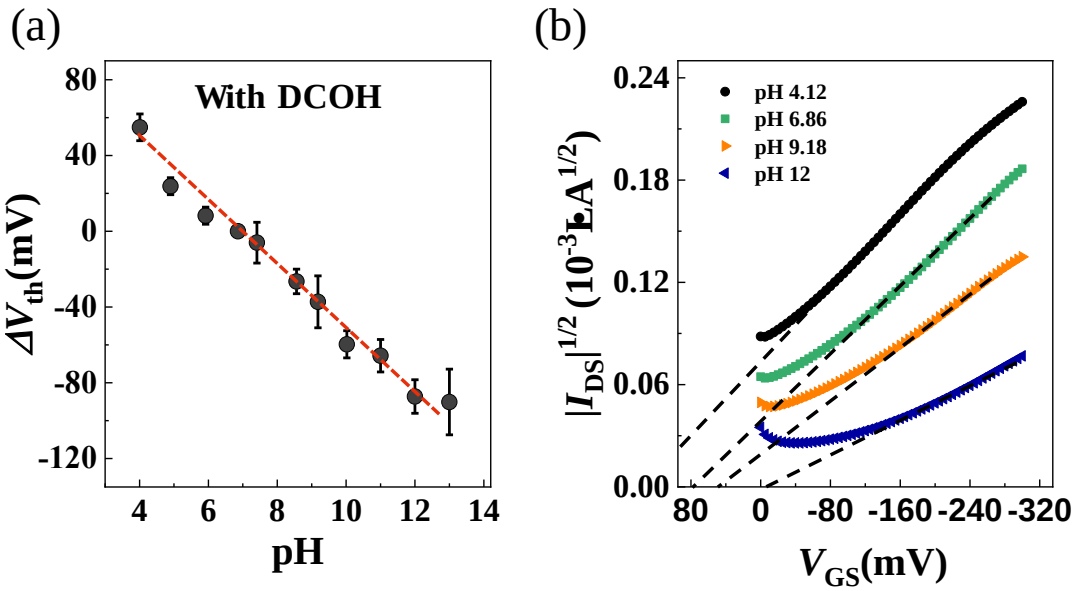

Figure 4.8. (a) Variation in threshold voltage (ΔV_{th}) of EG-OFET operating in electrolyte solutions with different pH levels for P3HT with DCOH lipid. (b) Square root of the drain current versus gate voltage curves of EG-OFETs with DCOH lipid monolayer in different pH solution (4.12, 6.86, 9.18 and 12).

In a case of the DCPC lipid monolayer, the transistors showed wide variations against the different pH levels, as seen in **Figure 4.7 (b)**. However, the dependence of ΔV_{th} on the pH variation was no clear. This result was probably due to the intrinsic characteristics of zwitterionic head groups of DCPC lipids.[125–130] At pH 2, an incipient protonation of the phosphate group converts the P-N zwitterions (lipid PN dipole) into phosphoric acid and $-N^{+}(CH3)_3$ cations. This is related to conformational changes of the polar head group and the gradual increase of ΔV_{th}.[129,135–138] On the contrary, at higher pH (8.5-13),

phosphoric acid group deprotonation leads to an increase of the negative charges at the surface. A linear increase of ΔV_{th} was observed in this range.[128,136] Meanwhile, in the pH range 4-8.5, no changes of ΔV_{th} were observed because the density of charges at the surface remains almost unchanged in this range.[126,127,135,136] In this manner, DCPC lipid monolayers showed complicated variations in ΔV_{th} depending on the surface charges.

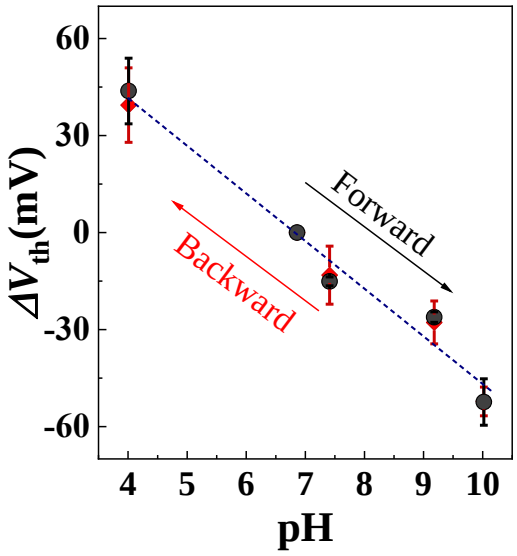

Figure 4.9. Variation in threshold voltage (ΔV_{th}) of EG-OFET with DCOH operating in electrolyte solutions with different pH levels from 4.01 to 10 with black points and reservedly with red points.

In contrast, the DCOH lipid monolayer demonstrated a clear linear dependence of ΔV_{th} on the pH level, as seen in **Figure 4.8 (a)**. The ΔV_{th} was negatively shifted from +50 mV to -100 mV in the range of pH from 4 to 12. The sensitivity is approximately 17.76 mV per pH. This result can be explained by the formation of H_3O^+ at the OH group. The concentration of H_3O^+ at the interface of DCOH changes according to the pH value. These extra charges cause the modulation of the capacitance of EDL, leading to the variation of charge accumulation in the P3HT channel.[20,58,139][139]. Hence, the transfer curves gradually shifted to a negative gate voltage corresponding to the increase of the pH level. This tendency was observed in **Figure 4.8(b)**. Additionally, the devices demonstrated stability with small hysteresis when changing pH values from acid to and vice versa (**Figure. 4.9**). Under the pH of 4, there was no dependence of the ΔV_{th} on the pH level. From these results, head groups of the lipid monolayer demonstrated their importance on

EG-OFET performance. The chemical reactions of the head groups at different pH levels significantly impacted on the performance of transistors. Notably, the EG-OFET with the DCOH showed a linear sensitivity with the physiological pH range of 4-8 that is suitable for biology and medicine applications.[36] This finding is useful to fulfill sensing applications with biological friendliness.

4.3.4. Design of head groups of lipid monolayers for pH non-sensitive

For sensor applications, the control of pH sensitivity is a key factor because pH sensitivity interferes with the signal of sensors. Therefore, we discussed how to design the head groups of lipid monolayers for enhancing pH sensitivity in the previous section. In some cases, the development of sensors with non-sensitivity to pH variations is also necessary. In practical, the pH level of the electrolyte solution is always changing. This probably interferes with the received signal of sensors when sensors detect a small number of analytes (ions or proteins) in the electrolyte solution.[20] I, therefore, would like to remove the noise signal from the variation of pH level. For this purpose, I passivated the DCOH lipid monolayer by MTS groups. The OH groups were replaced by MTS groups through the silanization protocol. Then, the pH sensitivity and the operation stability of the EG-OFET with DC-MTS lipid monolayer were investigated with the same conditions as other EG-OFETs.

The V_{th} of DC-MTS remained a low threshold voltage, +120 mV. It should be noted that the transistors became non-sensitive to the pH variation, as shown in **Figure 4.10 (a)**. There was a negligible variation in V_{th} (ΔV_{th} ~ 0 mV) regardless of pH levels. Additionally, the deviation of V_{th} at each pH level was small due to the reduction of the doping effect. This means that the MTS groups successful passivated the OH-groups. Furthermore, the EG-OFET showed a stable operation even after exposing to the organic solvent (**Figure 4.10 (b)**). The V_{th} showed almost no change even after repeated measurements for 2 hours. It should be emphasized that this technique not only can passivate OH terminals but also can be grafted sensing receptors onto the lipid monolayer at R-positions in **Figure 2.5**. The EG-OFET with DCOH monolayer can provide a platform for further functionalization by specific probes for versatile sensor applications.

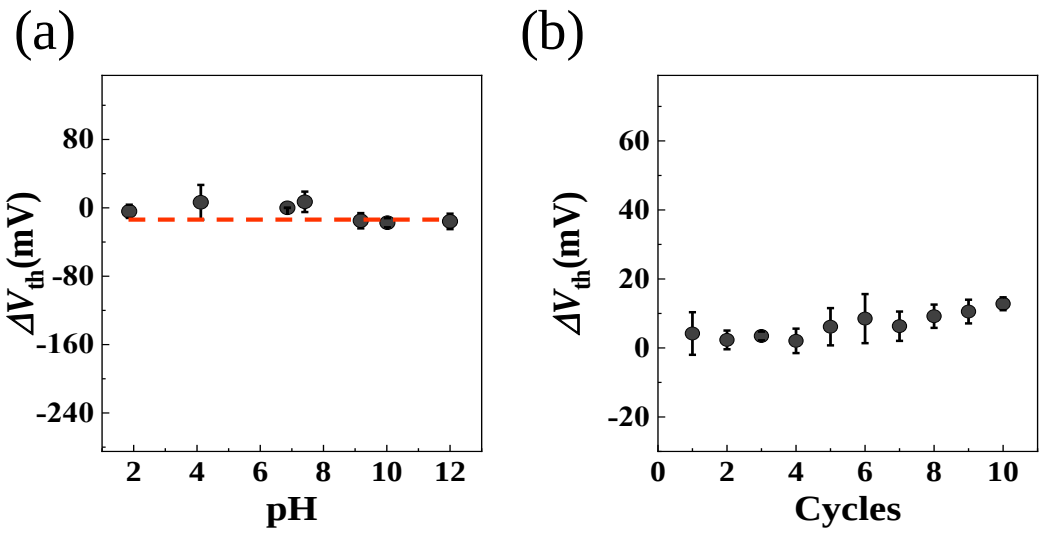

Figure 4.10. The performance of EG-OFET after directly MTS modification of DCOH head-groups on the P3HT film by silanization protocol. (a) pH dependence of ΔV_{th}, showing no variations. (b) ΔV_{th} after repeated operations.

4.4. Ion sensor applications: detection of cesium ions

4.4.1. Experimental details

For ion sensor applications, the cesium probes were attached to the DCOH monolayer of EG-OFET through the silanization protocol. **Figure 4.11** shows the chemical structure of the cesium probe on the lipid layer. The cesium probes were synthesized by my collaborators at Centre Interdisciplinaire de Nanoscience de Marseille (CINaM). The UV-VIS showed that the new cesium probes had an affinity to cesium, potassium, and rubidium ions.[89] However, the highest affinity was obtained with cesium ions.[89] Additionally, HNMR measurements showed that cesium ions could replace potassium and rubidium ions in complexes.[89] The detail of the synthesis procedure and properties of cesium probes were described in detail in the **Appendix section**. When the cesium ions are captured by the probes to form stable complexes, there are extra positive charges at the surface. In this section, I demonstrated the detection ability of the sensor to cesium ions.

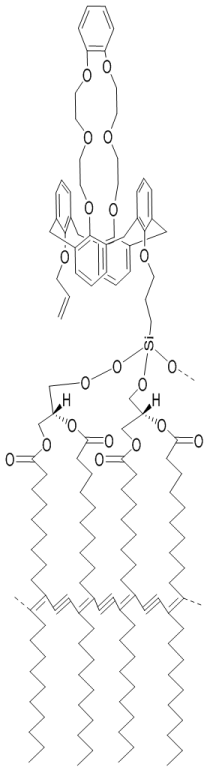

Figure 4.11. The chemical structure of lipid monolayer with Cesium probe at head group.

To evaluate the detection of cesium ions of sensors, 100 μL of solutions of cesium ions at different concentrations were dropped into the container and kept in 5 minutes for the reaction between ions and probes. Then, the samples were rinsed by phosphate buffer saline (PBS) at a fixed pH of 7.4. The PBS solution was also used as an electrolyte solution for EG-OFETs. For the selectivity, the sensor was also exposed to other interfering ions such as potassium, sodium, calcium, and rubidium. After that, in comparison with the conventional technique, the same samples of cesium ion were both characterized by our sensor and ICP-MS. Finally, for practical application, the sensor was tested in synthetic seawater.

4.4.2. Results and discussion

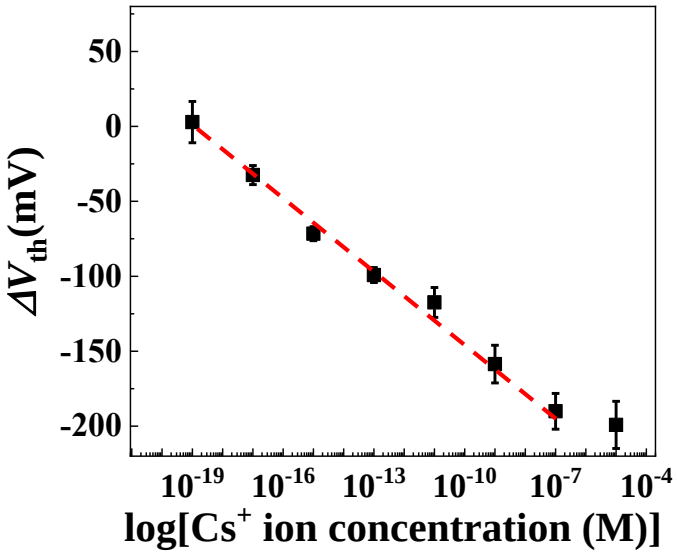

Figure 4.12. Variation in threshold voltage (ΔV_{th}) of sensor after exposing the sensor active area to cesium ion at different concentrations in PBS.

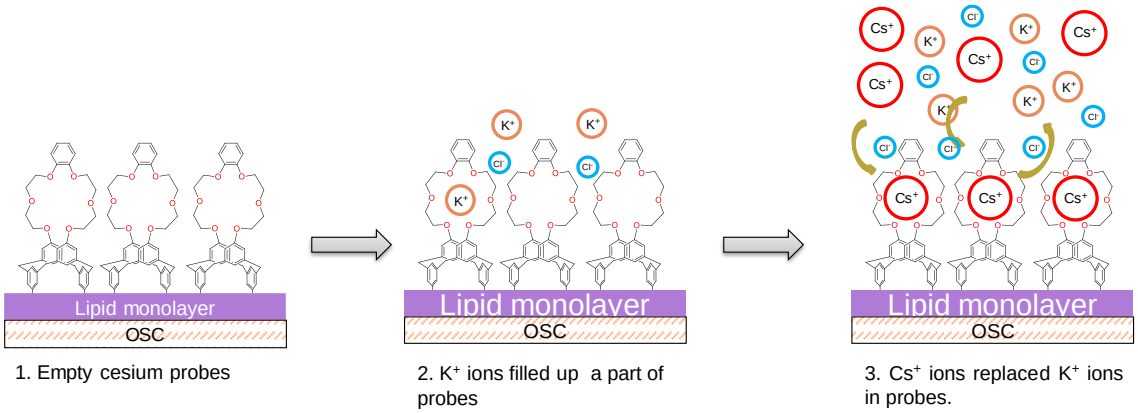

Figure 4.13. The schematic of sensing mechanism for Cs^+ ion detection.

The output signal of the sensor was determined based on the shift of V_{th}, which was estimated from the I_{DS}-V_{GS} curves of EG-OFET. During the measurements, V_{GS} was swept from 0 to -300 mV at constant V_{DS} of -300 mV. The solution of cesium ions contained the interfering ions, namely potassium (K^+, 10^{-2} M) and sodium (Na^+, 10^{-2} M). The concentration of cesium ion varied from 0.01 fM to 10 µM. First of all, I measured the EG-OFETs at zero concentration to obtain the V_{th0} as a background signal. Then, the sensors were exposed to different cesium concentrations to calculate the corresponding

V_{th} values. The change in the V_{th} was induced by the capture of cesium ions carrying positive charges at the surface of the lipid monolayer. **Figure 4.12** showed the linear dependence of the ΔV_{th} on the cesium ion concentrations. The result showed that the sensors could detect cesium ions in a wide range from 0.01 fM to 10 µM. The total shift of V_{th} is 157 mV. Additionally, the deviation of ΔV_{th} at each concentration was negligible.

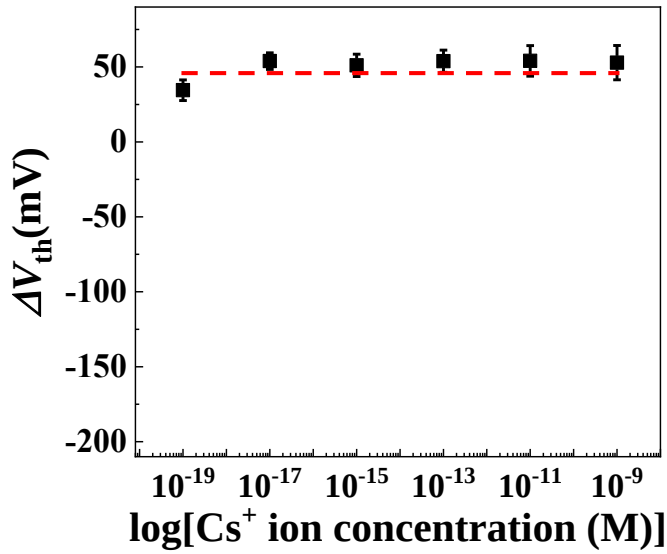

Figure 4.14. Variation in threshold voltage (ΔV_{th}) of EG-OFET without cesium probes after exposing the sensor active area to cesium ion at different concentrations in PBS.

Figure 4.13 shows the mechanism of sensors for the detection of cesium ions in PBS. At the initial stage, the potassium ions probably attached to a small part of probes due to their weak affinity to probes. When the sensor exposes to the solution of cesium ions, cesium ions gradually filled up vacant probes. This process causes the change of surface charge at the surface, leading to the reduction of V_{th}. At a higher concentration, there was no change of the V_{th}. This can be explained that the saturation of the probes or the maximum complexing capacity of the sensor has been reached. Meanwhile, the samples without cesium probes showed no dependence of V_{th} on cesium ion concentration (**Figure 4.14**). This means that the shift of V_{th} only happened when cesium ions interacted with our probes. Our sensor demonstrated ultra-sensitivity and specificity to cesium ions at the femtomolar concentration in the presence of interfering ions.

For the comparison of our sensor with the conventional technique, we characterized the sample samples of cesium ion at different concentrations by ICP-MS

and our sensor. **Figure 4.15** showed a significantly different performance of our sensor and ICP-MS. The lowest concentration of cesium ion could be detected by ICP-MS is 10^{-3} ppb. The highest range cesium of ICP-MS was around 1 ppb. For higher concentration, the sample must be diluted to approximately 1 ppb. Meanwhile, our sensor demonstrated the sensitivity for the detection of cesium ions at low concentrations of prepared samples (from 10^{-7} to 1 ppb). This result indicated that our sensor was higher sensitivity than the ICP-MS technique for the detection of cesium ion.

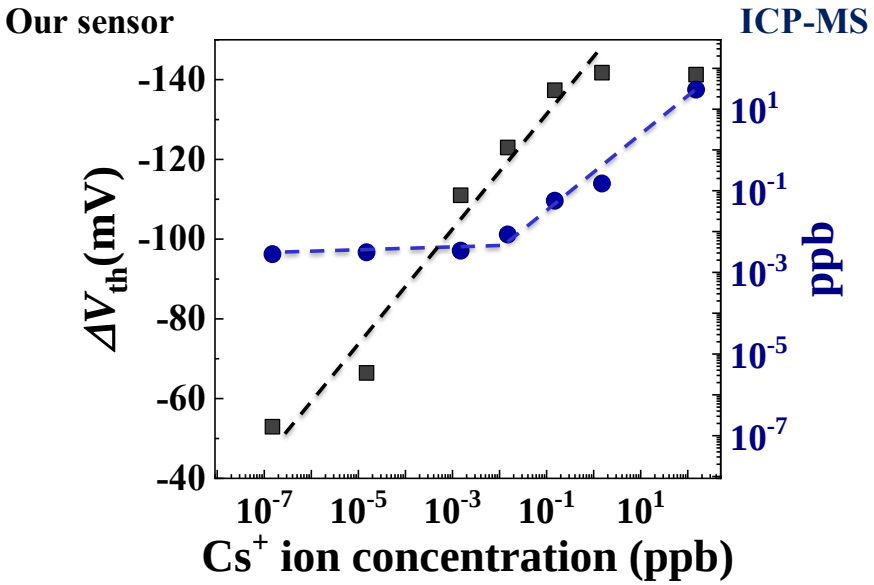

Figure 4.15. Comparison of our sensor and ICP-MS in detection of cesium ion.

From the above results, I tried to characterize the performance of the sensor in the synthetic seawater for practical application. In the synthetic seawater, there are many kinds of ions at high concentrations, such as potassium (10^{-2} M), sodium (10^{-1} M), magnesium (10^{-2} M), calcium (10^{-2} M), strontium, etc.[140] Interestingly, our sensor still could detect the signal of ultra-low cesium ion concentration, as seen in **Figure 4.16**. The lowest concentration of cesium ion was detectable is 10^{-17} M even in the presence of interfering ions at high concentrations. However, the shift of V_{th} was 70 mV, smaller than that in PBS (157 mV). This result could be explained by the increase in the capacitance of EDL. Because the concentration of ions in seawater is approximately one order higher than those in PBS solution, the Debye length reduces, leading to the rise of the EDL

capacitance.[120,141] This result indicates that our sensor has a high potential for the detection of cesium ions in practical conditions.

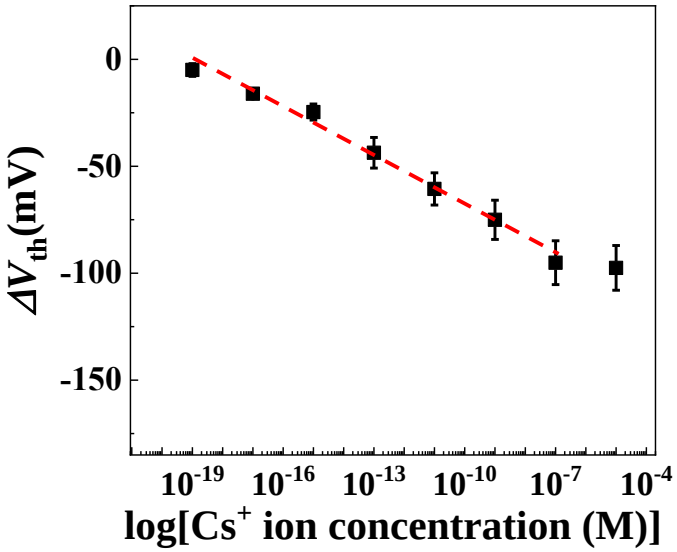

Figure 4.16. Variation in threshold voltage (ΔV_{th}) of sensor after exposing the sensor active area to cesium ion at different concentrations in seawater.

4.5. Conclusion

In summary, I have developed a novel EG-OFET with the functionalization of polymeric semiconductors based on a conjugation between the organic semiconductor and the engineered lipid monolayer. The engineered lipid monolayer contributed to the improvement of EG-OFET operation by minimizing the doping effect of electrolyte solution into the organic semiconductor. The V_{th} was negligible change even after operating in the electrolyte solution for a long time. Furthermore, the performance of EG-OFET can be controlled by the different functional groups of the lipid monolayer. The EG-OFET with DCOH monolayer demonstrated a linear pH sensitivity in the physiological range of pH (4-8). Meanwhile, the devices of DCPC monolayer were sensitive to pH out of this range (under pH 4 and upper pH 8). The EG-OFET with DOCH showed the potential for pH sensor applications. However, the pH sensitivity is a disadvantage for ion sensors because the pH dependence of devices can change the output signal of ion sensors. Therefore, it is necessary to eliminate the pH sensitivity of lipid

monolayers. Here, I passivate head groups of lipid monolayers by methyltrichlorosilane (MTS), which is inert to pH variation. This method is also employed for grafting the specific probes to lipid monolayers. Here, the Cs^+ probes are attached to lipid monolayers through MTS molecules for ion sensor applications. The sensor demonstrated a linear sensitivity and specificity to Cs^+ ions even in the presence of interfering ions in synthetic seawater. The limit of detection (LOD) and the large range of detection is 10^{-17} M and 10 orders of concentration, respectively. The limit of detection of our sensor covered the safety level of Japanese government for cesium ion concentration in drink water. Additionally, the performance of our sensor overcame the performance of ICP-MS and other reported sensors. These results indicate that EG-OFET functionalized by lipid monolayer can be utilized for sensor applications for the detection of ions. Our approach will pave the way for the development of new sensor applications in chemical and biological fields.

Chapter 5 Summary and conclusion

In summary, this dissertation has provided a new way to functionalize the P3HT film by the lipid monolayer. Additionally, a better understanding of the operation of EG-OFET functionalized by lipid monolayer was revealed. Interestingly, the applicability in sensors of EG-OFET with the lipid monolayer

In chapter 2, the functionalization of the P3HT surface was conducted by depositing the lipid monolayer (2.1 nm) on the P3HT film. The formation of lipid monolayer was confirmed with the presence of specific bonds (C=C, C-N, C=O) in the FTIR spectrum. Additionally, the surface property of P3HT changed from hydrophobic to hydrophilic of the lipid monolayer. On the other hand, the mechanical stability of lipid monolayer was significantly increased by inter-polymerization in the middle of lipid molecules. The rupture force of lipid monolayer increased 4 times after the polymerization process. The ultra-thin lipid monolayer, therefore, was stably formed on the P3HT film.

In chapter 3, a fundamental operation of WG-OFET functionalized by a lipid monolayer was established. The de-ionized water (DI-water) was used as electrical gates in the transistors. The highly pure water is salt-free with ionic ions leading to minimize the doping effect of ions to organic semiconductor. The EDL formed at the interface between water and the organic semiconductor plays an important role in allowing WG-OFET to operate at a millivoltage range. Because of a sub-nano thickness, the EDL depends strongly on the surface morphology of the P3HT film. A flat surface reduced the off current, as a consequence of the minimization of trapped ions in the P3HT film. The on/off ratio, therefore, increased around three times and be stable with long-term repeatability. Another key factor is gate electrode metal immersing in water. The intrinsic work function of metal modulated the threshold voltage (V_{th}) of WG-OFET. The V_{th} with gold (Au) electrode reduced from −0.23 V of tungsten (W) electrode to + 0.07 V. As a result of this shift in $V_{th,}$ the on current with the Au electrode increased almost seven times in comparison with the W electrode. However, there was a remarkable hysteresis loop in a transfer curve that probably caused by carrier traps. To reduce this effect, an ultra-thin

lipid monolayer was introduced on the P3HT surface. The WG-OFET coated by the lipid membrane showed a negligible hysteresis loop in the transfer curve.

Chapter 4 demonstrated the performance of EG-OFET functionalized by lipid monolayers for sensor applications. In particular, the detection of ions and biomolecules is typically carried out in the presence of interfering ions. An electrolyte solution, therefore, was replaced DI-water as a gating medium. In this case, the benefit of lipid monolayer in the protection of P3HT film from the doping of electrolyte ions was more clearly expressed. EG-OFET with lipid monolayer demonstrated the stability of V_{th} even in aqueous conditions after ten cycles of measurements. Meanwhile, the pristine EG-OFET showed the variation of V_{th}. Moreover, the lipid monolayers with functionalized head groups provided a capability for pH sensors. The OH-terminated lipid monolayer demonstrated a linear sensitivity with the pH level in the range of 4 to 12. This range satisfies the physiological pH range of 4-8 required for biosensor applications. Meanwhile, the lipid monolayers with polar head groups showed the pH sensitivity in the range under 4 and upper 8. However, for the ion sensor applications, the pH sensitivity need to be eliminated. Therefore, the OH-groups were successfully passivated by methyl trichlorosilane (MTS) resulting in the transistors becoming non-pH sensitivity. The significantly stable operation of transistors was maintained in the electrolyte solution. Then, the Cs^+ probes were attached to OH substitutes of lipid monolayers instead of MTS molecules for ion sensor applications. The sensor demonstrated the ultra-high sensitivity (LOD: 10^{-17} M) and specificity to Cs^+ ions even in the pseudo-practical condition, synthetic seawater. The performance of the sensor also covered the requirement of the Japanese government for the safety concentration of cesium ion in tap water. Additionally, the sensor showed outstanding performance in comparison to ICP-MS and other reported sensors.

This dissertation showed the stable operation and applicability in sensors of EG-OFETs modified by the functionalized lipid monolayer in the electrolyte solution. The findings in this dissertation will pave the way for the development of new sensor applications in chemical and biological fields.

Appendix Synthesis of cesium probes

Figure S1 shows the schematic for the synthesis procedure of the cesium ion probes based on calix[4]arene (**1**). The synthesis and characterization of cesium ion probes were completed by our collaborators in France.[89] First of all, calix[4]arene powder was dissolved in anhydrous acetonitrile-CH_3CN (MeCN) solvent, followed by adding potassium carbonate into the solution to synthesize 1,3 calix[4]arene bis-allyloxy (**2**). Then, the mixture was stirred and kept at 70°C for 2 hours under reflux. During this process, allyl bromide was added dropwise into the mixture. The reaction mixture was heated at 80°C under reflux and stirred for 2 days. The residue substance was dissolved in $CHCl_3$ solvent, followed by the three-step washing process with HCl 2 M, solution of sodium carbonate and DI-water. Afterward, the mixture is dried over $MgSO_4$, filtered and evaporated in a vacuum to obtain (2).

In next step, 1,2-bis(5-hydroxy-3-oxa-1-pentyloxy)benzene **(4)**-crown ether was synthesized from catechol **(3)**. Firstly, catechol was dissolved in DMF solvent. After that, K_2CO_3 and 2-(2-chloroethoxy)ethanol were added to the solution. The mixture then was heated at 80 °C and stirred under N_2 overnight. Then, the solvent was dried in a vacuum. The residue was dissolved in chloroform solvent, followed by a washing process with aqueous NaOH 0.5 M and DI-water. The substance was dried over Na_2SO_4 and evaporated in a vacuum.

For grafting on the calixarene scaffold, 1,2-bis(5-toluenesulfonyl-3-oxa-1-pentyloxy)benzene (5) was synthesized. Firstly, NaOH solution was prepared and then added solution of THF containing **(4)** molecules. The mixture was stirred and kept at 0 °C in 1 hour. During this process, p-toluenesulfonyl chloride in THF solvent was added dropwise. Then, solution of 10% HCl was added to the mixture. The residue was extracted two times by using CH_2Cl_2 solvent. Then, the solution was washed by a three-step process with DI-water and, aqueous $NaHCO_3$ 0.5M and DI-water. Each step was done two times with each cleaning solution. Finally, the synthesized solution was dried over $CaCl_2$ and evaporated in a vacuum.

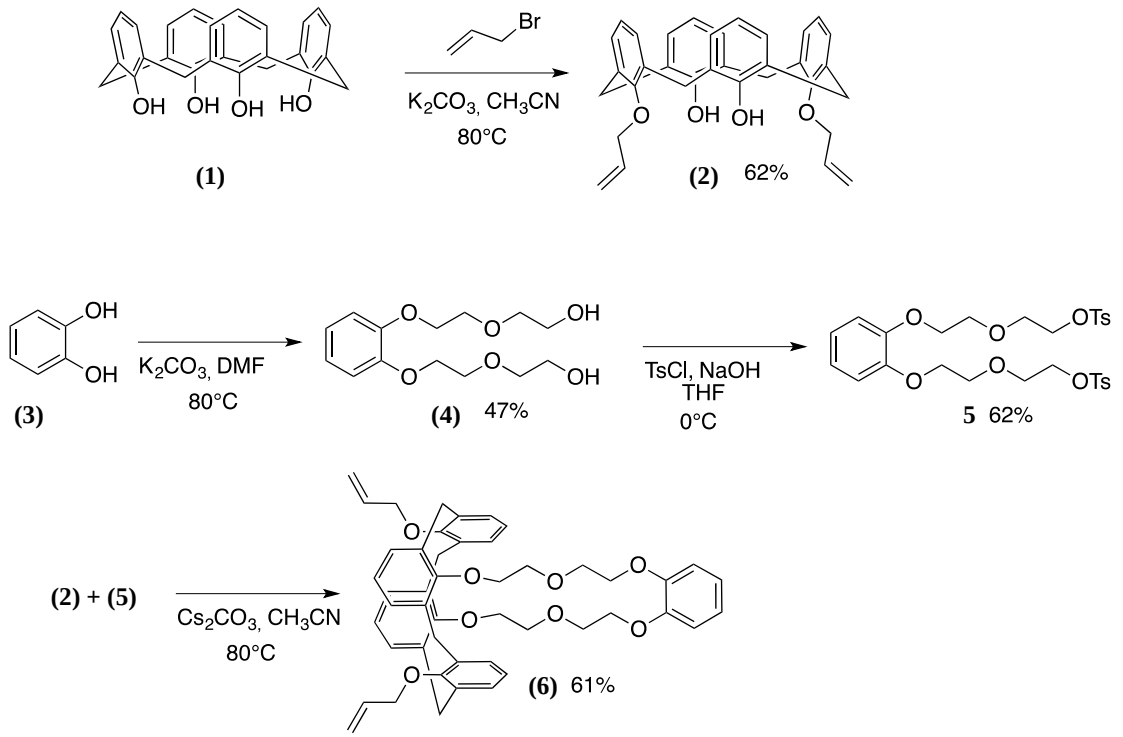

Figure S 1. The schematic of cesium probe synthesis process.[89]

Finally, the crown ether **(5)** was grafted on the calixarene scaffold **(2)**. 1,3-alternate 25,27-bis(allyloxy)-1,2-phenylenebis(5-dioxy-3-oxa-1-pentyloxy)]calix-[4]arene **(6)** was synthesized. **(2)** molecules were dissolved in anhydrous MeCN solution and cesium carbonate then was added. The mixture was heated at 70°C and stirred reflux for 2 hours under argon. During this process, **(5)** molecules dissolved in anhydrous MeCN solvent was added dropwise. The reaction mixture was heated at 80°C under reflux and stirred for 2 days. The residue was evaporated and then extracted with CH_2Cl_2 solvent by two times. The solution was washed by a three-step process with HCl 2 M, brine and DI-water. The synthesized solution was rinsed 2 times by each cleaning solution. Afterward, it is dried over Na_2SO_4, filtered and evaporated in a vacuum.

For attaching the cesium probe on the lipid membrane, the probe was modified by silane group to form hydrosilylation of 1,3-alternate 25,27-bis(allyloxy)-1,2-phenylenebis(5-dioxy-3-oxa-1-pentyloxy)]calix-[4]arene **(7)**. **(6)** molecules and triethoxysilane were diluted in 2 mL anhydrous toluene. After stirring 20 minutes under argon, 20µL solution of commercial Karstedt catalyst was added to the mixture. Then, the mixture was kept at 50°C and stirred for 12 hours in an argon-filled glove box. After

cooling down to room temperature, the mixture was filtered through a Celite pad. The excess of triethoxysilane was removed in a vacuum.

All of the chemical compounds were chromatographed by NMR ^{1}H ($CDCl_3$, 400 MHz) to confirm the chemical structure.

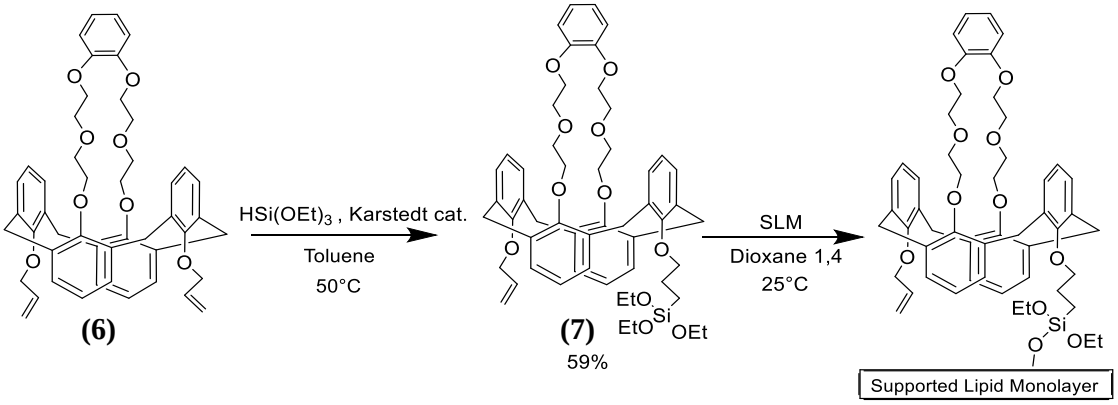

Figure S 2. The functionalization of Cesium probe by silane group to graft on lipid membrane.[89]

Abbreviation

AAPD: azobis(2-amidinopropane) dihydrochloride

AFM: Atomic force measurement

APTES: (3- aminopropyl)triethoxysilane

ATR-FTIR: attenuated total reflection Fourier transform infrared

DCPC: 1,2-bis(10,12-tricosadiynoyl)-sn-glycero-3- phosphocholine

DCOH: 1,2-bis(10,12-tricosadiynoyl)-sn-glycero-3

DC-MTS: 1,2-bis(10,12-tricosadiynoyl)-sn-glycero-3-methyldichlorosilane

EDL: Electrical double layer

EIS: Electrochemical impedance spectra

EG-OFET: Electrolyte-gated organic field effect transistor

GC: Gas chromatography

GC-MS: Gas chromatography coupled with mass spectroscopy

HPLC: High-performance liquid chromatography

ICP-MS: Inductively coupled plasma-mass spectroscopy

LC-MS and LC-MS/MS: Liquid chromatography coupled with mass spectroscopy

LC-ED: Electrochemical detection

LOD: Limit of detection

MOSFET: Metal-oxide-semiconductor field effect transistor

MTS: Methyltrichlorosilane

OCET: Organic electrochemical transistor

OFET: Organic field effect transistor

P3HT: Poly(3-hexylthiophene-2,5-diyl)

PDMS: Polydimethylsiloxane

PSPD: Position sensitive photo-detector

RMS: Root mean roughness

XRD: X-ray diffraction

XRR: X-ray reflection

WG-OFET: Water-gated organic field effect transistor

Acknowledgment

First of all, I would like to appreciate my supervisor, Professor. Yutaka Wakayama, who gave me a chance to join the interesting researches. I also received a lot of valuable advice from him only in research but also in living. I would like to express my sincere thanks to Dr. Ryoma Hayakawa, for his very kind advice and support. I could not have done my study successfully without their enthusiastic helping. I am further thankful to my collaborators, Dr. Anne Charrier, Associate Professor. Matthieu Petit, Professor. Jean-Manuel Raimundo, and Volkan Kilinc for their supporting and discussing with me all the time.

I would like to express my gratitude to Dr. Masayoshi Higuchi and Dr. Yemineni Narayana who supported me to measure electrochemical impedance spectra by Solartron system.

I am also very grateful to Ms. Miko Wanatabe who helped me for AFM and XRD measurements. I would like to thank Ms. Remi Minoshima and Ms. Matsushita who supported me to solve many personal issues all the time.

I would like to appreciate my parents, my wife and my son for their support during the doctoral course.

Finally, I gratefully acknowledge the financial support from the Strategic International Collaborative Research Program (SICORP) supported by the Japan Science and Technology Agency (JST) and L'Agence Nationale de la Recherche (ANR) as well as from the World Premier International Center (WPI) for Materials Nanoarchitectonics (MANA) of the National Institute for Materials Science (NIMS), Tsukuba.

References

[1] A. Raouf MS, A. Raheim ARM, *J. Pollut. Eff. Control* **2016**, *05*, 1.

[2] A. G. Heath, *Water Polution and Fish Physiology*, *2nd ed*; 1995; Vol. 14.

[3] A. E. McKeown, G. Bugyi, *Impact of water pollution on human health and environmental sustainability*; McKeown, A. E.; Bugyi, G., Eds.; Practice, Progress, and Proficiency in Sustainability; IGI Global, 2015; Vol. 53.

[4] https://mjiit.utm.my/analytical-lab/lab-services/instrument/chromatography/.

[5] https://www.indiamart.com/proddetail/atomic-absorption-spectrophotometer-18274652630.html.

[6] S. D. T. Kelly, N. K. Suryadevara, S. C. Mukhopadhyay, *IEEE Sens. J.* **2013**, *13*, 3846.

[7] M. T. Lazarescu, *IEEE J. Emerg. Sel. Top. Circuits Syst.* **2013**, *3*, 45.

[8] P. Lin, F. Yan, *Adv. Mater.* **2012**, *24*, 34.

[9] C. S. Lee, S. Kyu Kim, M. Kim, *Sensors* **2009**, *9*, 7111.

[10] L. Torsi, M. Magliulo, K. Manoli, G. Palazzo, *Chem. Soc. Rev.* **2013**, *42*, 8612.

[11] G. Horowitz, *Adv. Mater.* **1998**, *10*, 365.

[12] R. F. De Oliveira, L. Merces, T. P. Vello, C. C. Bof Bufon, *Org. Electron.* **2016**, *31*, 217.

[13] Z. Bao, A. Dodabalapur, A. J. Lovinger, *Appl. Phys. Lett.* **1996**, *69*, 4108.

[14] F. Werkmeister, B. Nickel, *J. Mater. Chem. B* **2013**, *1*, 3830.

[15] M. E. Roberts, S. C. B. Mannsfeld, N. Queraltó, C. Reese, J. Locklin, W. Knoll, Z. Bao, *Proc. Natl. Acad. Sci. U. S. A.* **2008**, *105*, 12134.

[16] Z. Ma, H. Geng, D. Wang, Z. Shuai, *J. Mater. Chem. C* **2016**, *4*, 4546.

[17] B. Yaman, I. Terkesli, K. M. Turksoy, A. Sanyal, S. Mutlu, *Org. Electron.* **2014**, *15*, 646.

[18] S. Cotrone, M. Ambrico, H. Toss, M. D. Angione, M. Magliulo, A. Mallardi, M. Berggren, G. Palazzo, G. Horowitz, T. Ligonzo, L. Torsi, *Org. Electron.* **2012**, *13*, 638.

[19] S. P. White, K. D. Dorfman, C. D. Frisbie, *Anal. Chem.* **2015**, *87*, 1861.

[20] T. D. Nguyen, A. Labed, R. El Zein, S. Lavandier, F. Bedu, I. Ozerov, H.

Dallaporta, J. M. Raimundo, A. M. Charrier, *Biosens. Bioelectron.* **2014**, *54*, 571.

[21] T. Minami, Y. Sasaki, T. Minamiki, S. ichi Wakida, R. Kurita, O. Niwa, S. Tokito, *Biosens. Bioelectron.* **2016**, *81*, 87.

[22] R. Hayakawa, M. Petit, K. Higashiguchi, K. Matsuda, T. Chikyow, Y. Wakayama, *Org. Electron.* **2015**, *21*, 149.

[23] L. Kergoat, L. Herlogsson, D. Braga, B. Piro, M. C. Pham, X. Crispin, M. Berggren, G. Horowitz, *Adv. Mater.* **2010**, *22*, 2565.

[24] L. Kergoat, B. Piro, M. Berggren, M. C. Pham, A. Yassar, G. Horowitz, *Org. Electron.* **2012**, *13*, 1.

[25] S. Lai, M. Demelas, G. Casula, P. Cosseddu, M. Barbaro, A. Bonfiglio, *Adv. Mater.* **2013**, *25*, 103.

[26] M. Magliulo, A. Mallardi, M. Y. Mulla, S. Cotrone, B. R. Pistillo, P. Favia, I. Vikholm-Lundin, G. Palazzo, L. Torsi, *Adv. Mater.* **2013**, *25*, 2090.

[27] F. Buth, A. Donner, M. Sachsenhauser, M. Stutzmann, J. A. Garrido, *Adv. Mater.* **2012**, *24*, 4511.

[28] T. P. Nguy, R. Hayakawa, V. Kilinc, M. Petit, J.-M. Raimundo, A. Charrier, Y. Wakayama, *Jpn. J. Appl. Phys.* **2019**, *58*, SDDH02.

[29] F. Buth, D. Kumar, M. Stutzmann, J. A. Garrido, *Appl. Phys. Lett.* **2011**, *98*, 2009.

[30] S. Cotrone, M. Ambrico, H. Toss, M. D. Angione, M. Magliulo, A. Mallardi, M. Berggren, G. Palazzo, G. Horowitz, T. Ligonzo, L. Torsi, *Org. Electron. physics, Mater. Appl.* **2012**, *13*, 638.

[31] O. Knopfmacher, M. L. Hammock, A. L. Appleton, G. Schwartz, J. Mei, T. Lei, J. Pei, Z. Bao, *Nat. Commun.* **2014**, *5*, 2954.

[32] R. Porrazzo, S. Bellani, A. Luzio, E. Lanzarini, M. Caironi, M. R. Antognazza, *Org. Electron.* **2014**, *15*, 2126.

[33] T. Cramer, A. Campana, F. Leonardi, S. Casalini, A. Kyndiah, M. Murgia, F. Biscarini, *J. Mater. Chem. B* **2013**, *1*, 3728.

[34] K. Schmoltner, J. Kofler, A. Klug, E. J. W. List-Kratochvil, *Adv. Mater.* **2013**, *25*, 6895.

[35] A. Kenaan, R. El Zein, V. Kilinc, S. Lamant, J. M. Raimundo, A. M. Charrier, *Adv. Funct. Mater.* **2018**, *28*.

[36] G. K. Schwalfenberg, *J. Environ. Public Health* **2012**, *2012*.

[37] A. Aarkrog, *Deep. Res. Part II Top. Stud. Oceanogr.* **2003**, *50*, 2597.

[38] Iaea, *Environmental and Source Monitoring for Purposes of Radiation Protection*; General Safety Guides; INTERNATIONAL ATOMIC ENERGY AGENCY: Vienna, 2005; Vol. RS-G-1.8.

[39] G. W. Gokel, W. M. Leevy, M. E. Weber, *Chem. Rev.* **2004**, *104*, 2723.

[40] A. V. Tsukanov, A. D. Dubonosov, V. A. Bren, V. I. Minkin, *Chem. Heterocycl. Compd.* **2008**, *44*, 899.

[41] P. S. Ramanjaneyulu, A. N. Kumar, Y. S. Sayi, K. L. Ramakumar, S. K. Nayak, S. Chattopadhyay, *J. Hazard. Mater.* **2012**, *205–206*, 81.

[42] S. Gilmour, S. Miyagawa, F. Kasuga, K. Shibuya, *PLoS One* **2016**, *11*, e0152040.

[43] N. Alghamdi, Z. Alqahtani, M. Grell, *J. Appl. Phys.* **2019**, *126*.

[44] B. Radaram, T. Mako, M. Levine, *Dalt. Trans.* **2013**, *42*, 16276.

[45] M. Shamsipur, M. Asgari, M. G. Maragheh, D. Matt, *Sensors Actuators, B Chem.* **2015**, *209*, 9.

[46] L. Sudakov-Boreysha, A. Morgenshtein, U. Dinnar, Y. Nemirovsky, *11th IEEE Int. Conf. Electron. Circuits Syst. ICECS 2004* **2004**, 535.

[47] T. Nguyen Duc, R. El Zein, J. M. Raimundo, H. Dallaporta, A. M. Charrier, *J. Mater. Chem. B* **2013**, *1*, 443.

[48] T. Sakai, Y. Araki, H. Kanazawa, H. Umezawa, M. Tachiki, H. Kawarada, *Japanese J. Appl. Physics, Part 1 Regul. Pap. Short Notes Rev. Pap.* **2002**, *41*, 2595.

[49] J. H. An, S. J. Park, O. S. Kwon, J. Bae, J. Jang, *ACS Nano* **2013**, *7*, 10563.

[50] B. Veigas, E. Fortunato, P. V. Baptista, *Sensors (Switzerland)* **2015**, *15*, 10380.

[51] K. Maehashi, Y. Sofue, S. Okamoto, Y. Ohno, K. Inoue, K. Matsumoto, *Sensors Actuators, B Chem.* **2013**, *187*, 45.

[52] K. Manoli, M. M. Patrikoussakis, M. Magliulo, L. M. Dumitru, M. Y. Mulla, L. Sabbatini, L. Torsi, *Org. Electron. physics, Mater. Appl.* **2014**, *15*, 2372.

[53] S. Lai, M. Barbaro, A. Bonfiglio, *Sensors Actuators, B Chem.* **2016**, *233*, 314.

[54] M. Yun, A. Sharma, C. Fuentes-Hernandez, D. K. Hwang, A. Dindar, S. Singh, S. Choi, B. Kippelen, *ACS Appl. Mater. Interfaces* **2014**, *6*, 1616.

[55] Y. Diao, B. C. K. Tee, G. Giri, J. Xu, D. H. Kim, H. A. Becerril, R. M. Stoltenberg, T. H. Lee, G. Xue, S. C. B. Mannsfeld, Z. Bao, *Nat. Mater.* **2013**, *12*, 665.

[56] H. Ebata, T. Izawa, E. Miyazaki, K. Takimiya, M. Ikeda, H. Kuwabara, T. Yui, *J. Am. Chem. Soc.* **2007**, *129*, 15732.

[57] C. C. Chang, C. L. Pai, W. C. Chen, S. A. Jenekhe, *Thin Solid Films* **2005**, *479*, 254.

[58] I. Y. Sohn, D. J. Kim, J. H. Jung, O. J. Yoon, T. Nguyen Thanh, T. Tran Quang, N. E. Lee, *Biosens. Bioelectron.* **2013**, *45*, 70.

[59] L. Kergoat, B. Piro, M. Berggren, G. Horowitz, M. C. Pham, *Anal. Bioanal. Chem.* **2012**, *402*, 1813.

[60] D. Elkington, N. Cooling, W. Belcher, P. C. Dastoor, X. Zhou, *Electron.* **2014**, *3*, 234.

[61] F. X. Werkmeister, T. Koide, B. A. Nickel, *J. Mater. Chem. B* **2016**, *4*, 162.

[62] K. Melzer, M. Brändlein, B. Popescu, D. Popescu, P. Lugli, G. Scarpa, *Faraday Discuss.* **2014**, *174*, 399.

[63] T. Cramer, A. Kyndiah, M. Murgia, F. Leonardi, S. Casalini, F. Biscarini, *Appl. Phys. Lett.* **2012**, *100*, 0.

[64] M. Di Lauro, S. Casalini, M. Berto, A. Campana, T. Cramer, M. Murgia, M. Geoghegan, C. A. Bortolotti, F. Biscarini, *ACS Appl. Mater. Interfaces* **2016**, *8*, 31783.

[65] J. D. Yuen, A. S. Dhoot, E. B. Namdas, N. E. Coates, M. Heeney, I. McCulloch, D. Moses, A. J. Heeger, *J. Am. Chem. Soc.* **2007**, *129*, 14367.

[66] A. D. McNaught, A. Wilkinson, In *IUPAC Compendium of Chemical Terminology*; IUPAC: Research Triagle Park, NC, 2008.

[67] L. Herlogsson, X. Crispin, N. D. Robinson, M. Sandberg, O. J. Hagel, G. Gustafsson, M. Berggren, *Adv. Mater.* **2007**, *19*, 97.

[68] I. N. Hulea, H. B. Brom, A. J. Houtepen, D. Vanmaekelbergh, J. J. Kelly, E. A. Meulenkamp, *Phys. Rev. Lett.* **2004**, *93*, 16.

[69] C. Suspène, B. Piro, S. Reisberg, M. C. Pham, H. Toss, M. Berggren, A. Yassar, G. Horowitz, *J. Mater. Chem. B* **2013**, *1*, 2090.

[70] H. U. Khan, M. E. Roberts, O. Johnson, R. Förch, W. Knoll, Z. Bao, *Adv. Mater.* **2010**, *22*, 4452.

[71] W. H. Lee, J. H. Cho, K. Cho, *J. Mater. Chem.* **2010**, *20*, 2549.

[72] V. Skrypnychuk, N. Boulanger, V. Yu, M. Hilke, S. C. B. Mannsfeld, M. F. Toney,

Barbero, *Adv. Funct. Mater.* **2015**, *25*, 664.

[73] H. Toss, C. Suspène, B. Piro, A. Yassar, X. Crispin, L. Kergoat, M. C. Pham, M. Berggren, *Org. Electron. physics, Mater. Appl.* **2014**, *15*, 2420.

[74] S. Cotrone, M. Ambrico, H. Toss, M. D. Angione, M. Magliulo, A. Mallardi, M. Berggren, G. Palazzo, G. Horowitz, T. Ligonzo, L. Torsi, *Org. Electron. physics, Mater. Appl.* **2012**, *13*, 638.

[75] K. Sugihara, *ACS Nano* **2010**, *4*, 5047.

[76] A. Charrier, T. Mischki, G. P. Lopinski, *Langmuir* **2010**, *26*, 2538.

[77] M. Grit, D. J. A. Crommelin, *Chem. Phys. Lipids* **1993**, *64*, 3.

[78] J. C. Weaver, K. H. Schoenbach, *IEEE Trans. Dielectr. Electr. Insul.* **2003**, *10*, 715.

[79] R. J. O'Neill, L. Tung, *Biophys. J.* **1991**, *59*, 1028.

[80] C. Dumas, R. El Zein, H. Dallaporta, A. M. Charrier, *Langmuir* **2011**, *27*, 13643.

[81] A. Casnati, S. Barboso, H. Rouquette, M. J. Schwing-Weill, F. Arnaud-Neu, J. F. Dozol, R. Ungaro, *J. Am. Chem. Soc.* **2001**, *123*, 12182.

[82] F. Ugozzoli, A. Casnati, A. Pochini, R. Ungaro, F. Arnaud, S. Fanni, M. J. Schwing, R. J. M. Egberink, F. de Jong, D. N. Reinhoudt, *J. Am. Chem. Soc.* **1995**, *117*, 2767.

[83] H. Luo, S. Dai, P. V. Bonnesen, A. C. Buchanan, J. D. Holbrey, N. J. Bridges, R. D. Rogers, *Anal. Chem.* **2004**, *76*, 3078.

[84] J. L. Sessler, S. K. Kim, D. E. Gross, C. H. Lee, J. S. Kim, V. M. Lynch, *J. Am. Chem. Soc.* **2008**, *130*, 13162.

[85] L. Kergoat, L. Herlogsson, B. Piro, M. C. Pham, G. Horowitz, X. Crispin, M. Berggren, *Proc. Natl. Acad. Sci. U. S. A.* **2012**, *109*, 8394.

[86] J. M. Raimundo, Z. Chen, O. Siri, *Chem. Commun.* **2011**, *47*, 10410.

[87] R. Haddoub, M. Touil, J. M. Raimundo, O. Siri, *Org. Lett.* **2010**, *12*, 2722.

[88] R. Haddoub, M. Touil, Z. Chen, J. M. Raimundo, P. Marsal, M. Elhabiri, O. Siri, *European J. Org. Chem.* **2014**, *2014*, 745.

[89] V. Kilinc, C. Henry-de-Villeneuve, T. P. Nguy, Y. Wakayama, A. M. Charrier, J.-M. Raimundo, *ACS Appl. Mater. Interfaces* **2019**, *11*, 47635.

[90] K. Kanai, T. Miyazaki, H. Suzuki, M. Inaba, Y. Ouchi, K. Seki, *Phys. Chem. Chem. Phys.* **2010**, *12*, 273.

[91] R. El Zein, H. Dallaporta, A. M. Charrier, *J. Phys. Chem. B* **2012**, *116*, 7190.

[92] *https://www.spmtips.com/afm-probes-38-series.afms*.

[93] U. Maver, T. Velnar, M. Gaberšček, O. Planinšek, M. Finšgar, *TrAC - Trends Anal. Chem.* **2016**, *80*, 96.

[94] S. Garcia-Manyes, F. Sanz, *Biochim. Biophys. Acta - Biomembr.* **2010**, *1798*, 741.

[95] A. Kovalev, H. Shulha, M. Lemieux, N. Myshkin, V. V. Tsukruk, *J. Mater. Res.* **2004**, *19*, 716.

[96] C. Canale, M. Jacono, A. Diaspro, S. Dante, *Microsc. Res. Tech.* **2010**, *73*, 965.

[97] L. Picas, F. Rico, S. Scheuring, *Biophys. J.* **2012**, *102*, L01.

[98] *https://www.nanosurf.com/en/how-afm-works/afm-operating-principle* **2019**.

[99] V. Shahin, W. Hafezi, H. Oberleithner, Y. Ludwig, B. Windoffer, H. Schillers, J. E. Kühn, *J. Cell Sci.* **2006**, *119*, 23.

[100] J. Trilleras, D. J. Pacheco, A. Pérez-Gamboa, J. Quiroga, A. Ortiz, J. Gálvez, M. Nogueras, J. Cobo, *Appl. Sci.* **2017**, *7*, 967.

[101] M. Gagoś, M. Arczewska, *Eur. Biophys. J.* **2012**, *41*, 663.

[102] C. Zafiu, G. Trettenhahn, D. Pum, U. B. Sleytr, W. Kautek, *Phys. Chem. Chem. Phys.* **2011**, *13*, 13232.

[103] E. Barsoukov, J. R. Macdonald, *Impedance Spectroscopy: Theory, Experiment, and Applications*; 2005.

[104] B.-Y. Chang, S.-M. Park, *Annu. Rev. Anal. Chem.* **2010**, *3*, 207.

[105] C. Brett, A. Brett, *Electrochemistry: principles, methods, and applications*; 1993.

[106] C. Fernández-Sánchez, C. J. McNeil, K. Rawson, *TrAC - Trends Anal. Chem.* **2005**, *24*, 37.

[107] L. T. N. Truong, M. Chikae, Y. Ukita, Y. Takamura, *Talanta* **2011**, *85*, 2576.

[108] T. TN Lien, N. Xuan Viet,, M. Chikae, *J. Biosens. Bioelectron.* **2011**, *02*, 2.

[109] T. T. N. Lien, Y. Takamura, E. Tamiya, M. C. Vestergaard, *Anal. Chim. Acta* **2015**, *892*, 69.

[110] J. Kang, J. Wen, S. H. Jayaram, A. Yu, X. Wang, *Electrochim. Acta* **2014**, *115*, 587.

[111] P. Agarwal, *J. Electrochem. Soc.* **2006**, *139*, 1917.

[112] L. M. A. Monzón, L. M. Yudi, *Electrochim. Acta* **2006**, *51*, 1932.

[113] E. Diamanti, E. Gutiérrez-Pineda, N. Politakos, P. Andreozzi, M. J. Rodriguez-Presa, W. Knoll, O. Azzaroni, C. A. Gervasi, S. E. Moya, *Soft Matter* **2017**, *13*,

8922.

[114] L. M. Dumitru, K. Manoli, M. Magliulo, G. Palazzo, L. Torsi, *Microelectronics J.* **2014**, *45*, 1679.

[115] T. Minami, T. Sato, T. Minamiki, K. Fukuda, D. Kumaki, S. Tokito, *Biosens. Bioelectron.* **2015**, *74*, 45.

[116] M. Sessolo, J. Rivnay, E. Bandiello, G. G. Malliaras, H. J. Bolink, *Adv. Mater.* **2014**, *26*, 4803.

[117] H. N. Tsao, D. Cho, J. W. Andreasen, A. Rouhanipour, D. W. Breiby, W. Pisula, K. Müllen, *Adv. Mater.* **2009**, *21*, 209.

[118] C. Liu, Y. Xu, Y. Li, W. Scheideler, T. Minari, *J. Phys. Chem. C* **2013**, *117*, 12337.

[119] S. Fabiano, S. Braun, M. Fahlman, X. Crispin, M. Berggren, *Adv. Funct. Mater.* **2014**, *24*, 695.

[120] V. Lockett, M. Horne, R. Sedev, T. Rodopoulos, J. Ralston, *Phys. Chem. Chem. Phys.* **2010**, *12*, 12499.

[121] L. Kergoat, L. Herlogsson, B. Piro, M. C. Pham, G. Horowitz, X. Crispin, M. Berggren, *Proc. Natl. Acad. Sci.* **2012**, *109*, 8394.

[122] Y. Tack Lee, J. Keun Kim, R. Ha, H. J. Choi, S. Im, *Appl. Phys. Lett.* **2011**, *99*, 3.

[123] Y. Zhang, O. Pluchery, L. Caillard, A. F. Lamic-Humblot, S. Casale, Y. J. Chabal, M. Salmeron, *Nano Lett.* **2015**, *15*, 51.

[124] R. Jacobs, D. Morgan, J. Booske, *APL Mater.* **2017**, *5*.

[125] K. Arand, D. Stock, M. Burghardt, M. Riederer, *J. Exp. Bot.* **2010**, *61*, 3865.

[126] J. Stein, *Biophys. J.* **1986**, *49*.

[127] N. A. Alhakamy, I. Elandaloussi, S. Ghazvini, C. J. Berkland, P. Dhar, *Langmuir* **2015**, *31*, 4232.

[128] A. D. Petelska, Z. A. Figaszewski, *Biophys. J.* **2000**, *78*, 812.

[129] S. Pullanchery, T. Yang, P. S. Cremer, *J. Phys. Chem. B* **2018**, *122*, 12260.

[130] M. Mackiewicz, J. Romanski, M. Karbarz, *RSC Adv.* **2014**, *4*, 48905.

[131] O. Knopfmacher, A. Tarasov, W. Fu, M. Wipf, B. Niesen, M. Calame, C. Schönenberger, *Nano Lett.* **2010**, *10*, 2268.

[132] H. Butt, K. Graf, M. Kappl, *Physics and Chemistry of Interfaces*; Wiley: Germany, 2003.

[133] H. Ishii, K. Kudo, T. Nakayama, N. Ueno, *Electronic processes in organic*

electronics: Bridging nanostructure, electronic states and device properties; Monographs on the physics and chemistry of materials; Oxford University Press, 2015.

[134] L. Kergoat, N. Battaglini, L. Miozzo, B. Piro, M. C. Pham, A. Yassar, G. Horowitz, *Org. Electron.* **2011**, *12*, 1253.

[135] J. Stein, *Biophys. J.* **1986**, *49*.

[136] J. Kotyńska, I. Dobrzyńska, Z. A. Figaszewski, *Eur. Biophys. J.* **2017**, *46*, 149.

[137] J. Kotyńska, Z. A. Figaszewski, *Biochim. Biophys. Acta - Biomembr.* **2005**, *1720*, 22.

[138] A. D. Petelska, J. R. Janica, J. Kotynska, U. Łebkowska, Z. A. Figaszewski, *J. Membr. Biol.* **2012**, *245*, 15.

[139] Y. Qin, H. J. Kwon, M. M. R. Howlader, M. J. Deen, *RSC Adv.* **2015**, *5*, 69086.

[140] M. Cavasin, M. Sangermano, B. Thomson, S. Giannis, *Materials (Basel).* **2019**, *12*, 807.

[141] E. Stern, R. Wagner, F. J. Sigworth, R. Breaker, T. M. Fahmy, M. A. Reed, *Nano Lett.* **2007**, *7*, 3405.